THE EFFECT OF PARTICLE SIZE DISTRIBUTION ON SPECTRAL BACKSCATTERING COEFFICIENT

By

Erin N. Hildebrand

DALHOUSIE UNIVERSITY

HALIFAX, NOVA SCOTIA

NOVEMBER, 1999

Contents

List of Tables

List of Figures

Abstract

A ten week study over the course of the 1998 spring phytoplankton bloom in Bedford Basin, Nova Scotia, provided the first simultaneous, *in situ* measurements of the backscattering coefficient as a function of wavelength and the large (>100μm) particle size distribution. Correlations are sought between changes in the *in situ* size distribution greater than 100μm and the wavelength dependence of the backscattering coefficient. Measurement of backscatter made by the Hydroscat-6 (HOBI Labs) must be corrected for pathlength attenuation that occurs as the light travels from source to receiver. Corrections performed using the default method and one that uses measured optical properties showed generally less than 10% difference in the final backscatter estimates. The correction algorithms resulted in final estimates of backscatter that were most different when absorption was highest and in the chlorophyll *a* absorption band 442nm and region of strongest water absorption, 671nm. Using Mie theory, backscatter was predicted from particles greater than 100μm and compared with the values observed by the Hydroscat. Two linear relationships were found between observed and calculated backscatter. Backscatter predicted from large particles found in the first part of the study (February 26 to March 19) tended to under–predict observed backscatter while those from the second part of the study tended to over–predict observed backscatter. The change in the relationship is correlated with changing particle characteristics with respect to size distribution and composition as evidenced by ancillary data. Specifically, the results are consistent with observed backscatter from the first part of the study dominated by the signal from particles less than 100μm while backscatter from the second part of the study is dominated by that from large particle aggregates (>100μm). Changes in the shape of the particle areal size distribution per-unit-volume are correlated with changes in the spectral shape of backscatter. However, no consistent pattern change in the wavelength dependence of backscatter was found for similar changes in particle size distributions and the shape does not follow the theoretically predicted relationship between wavelength and backscatter.

List of Symbols

Table 1: Symbols used in this thesis.

Symbol	Definition	Units
α	Enhancement of backscatter from particles not correlated with large	unitless
A	Area of image particle	mm^2 or μm^2
A_T	Total area	m^2
$A(d_i)$	Area at particle equivalent circular diameter size d_i	m^2
A_V	Area of particles per–unit–volume	$m^2\ m^{-3}$
$A_V(d_i)$	Area of particles per–unit–volume at diameter d_i	$m^2\ m^{-3}$
A_f	Area fraction of particles	unitless
$A_{16,50,84}$	16, 50 and 84th percentiles of the areal cumulative frequency distributions	unitless
a	Absorption coefficient	m^{-1}
a_T	Total absorption	m^{-1}
a_p	Absorption from particulates	m^{-1}
a_{DOM}	Dissolved absorption	m^{-1}
a_w	Absorption due to water	m^{-1}
a_0	Asymptotic value of relationship between D'_f and λ	m^{-1}
a_1	Intercept of relationship between D'_f and λ	m^{-1}
a_*	Log area density function	$m^2\ m^{-3}$
β	Volume scattering function	$sr^{-1}m^{-1}$
b	Scattering coefficient	m^{-1}
b_{est}	Estimated scatter ($=\frac{b'_b}{b_b}$)	m^{-1}
b_b	Backscatter coefficient	m^{-1}

Table 1: continued. Symbols used in this thesis.

Symbol	Definition	Units
b'_b	Uncorrected backscatter	m^{-1}
b_{bT}	Total backscatter	m^{-1}
b_{bw}	Backscatter due to water	m^{-1}
b_{bp}	Backscatter from particulates	m^{-1}
b_{bdet}	Backscatter from detrital material	m^{-1}
$b_{bp(calc)}$	Backscatter calculated from images of particles using Mie theory	m^{-1}
$b_{bp(obs)}$	Backscatter measured by the Hydroscat minus b_{bw}	m^{-1}
b_{bp_L}	Backscatter from N_L large particles	m^{-1}
b_{bp_0}	Backscatter from N_{S_0} background particles	m^{-1}
b_{b_0}	b_{bp_0} plus backscatter from detrital material	m^{-1}
$\tilde{b}_b$	Backscattering ratio ($\frac{b_b}{b}$)	unitless
C	Concentration of particles of size d_0	# per m^3
c	Beam attenuation coefficient	m^{-1}
cl	Cluster number	unitless
γ	Pathlength amplification correction factor	m
D'_f	Measured filter pad absorbance	unitless
D'_c	Measured cuvette dissolved absorbance	unitless
D	Equivalent circular diameter	mm or μm
d	Particle diameter	m
d_0	Reference particle diameter	m
d_S	Small (<100μm) particle diameter	m
d_L	Large (>100μm) particle diameter	m
δ	Distance between objects in cluster analysis	parameter units
δ_{euc}	Euclidian distance between objects	unitless or m^2m^{-3}
δ_{cb}	City block distance between objects	unitless or m^2m^{-3}

Table 1: continued. Symbols used in this thesis.

Symbol	Definition	Units
$E(\lambda)$	Incident spectral irradiance	W m^{-2} nm^{-1}
η	HOBI Labs defined correction parameter	unitless
θ	Direction of light	sr
I	Intensity of incident light	W sr^{-1} nm^{-1}
K_{bb}	LED pathlength attenuation coefficient	m^{-1}
k_0	Hydroscat–6 calibration constant	unitless
k_1	Hydroscat–6 calibration constant	m^{-1}
k_2	Hydroscat–6 calibration constant	m^{-2}
λ	Wavelength	nm
ℓ	Geometric pathlength	m
M_A	Graphic mean of the image particles	unitless
m	Slope of the relationship between N_L and N_S	unitless
N	Number concentration of particles	# per m^3
N_L	Number concentration of large particles	# per m^3
N_S	Number concentration of small particles	# per m^3
N_{S_0}	Number concentration of small particles not correlated with large	# per m^3
n_*	Log number density function	# per m^3
n	Index of refraction	unitless
n_S	Mean index of refraction for small particles	unitless
n_L	Mean index of refraction for large particles	unitless
ξ	Exponent of Junge power-law	unitless
o_i (i=1,2)	Hydroscat offset to OBS depth	m
p	Number of mean bin diameters	unitless
Q_{bb}	Backscattering efficiency	unitless
$Q_{bb}(n_L, \lambda, d_L)$	Backscattering efficiency of large particles	unitless
$Q_{bb}(n_S, \lambda, d_S)$	Backscattering efficiency of small particles	unitless
R(0)	Irradiance reflected just below the surface	unitless
r	Number of objects	unitless
s	Slope of relationship between D'_f and λ	m^{-1}

Table 1: continued. Symbols used in this thesis.

Symbol	Definition	Units
se	Standard error	parameter units
SD	Standard deviation	parameter units
σ	Pathlength attenuation	unitless
ϕ	Phi units of particle size	ln(mm)
$\overline{\lvert x \rvert}$	Absolute mean	parameter units
V_{photo}	Total volume of the digital image	m^3
V	Equivalent circular volume	mm^3 or μm^3
v	Volume of water	m^3
x_{ij}	Value for object i and parameter j	unitless or m^2m^{-3}
Ω	Ratio of actual to theoretical backscatter from large particles	m^{-1}
ω_0	Single–scattering albedo $(\frac{b}{c})$	unitless
z	Corrected digital camera depth	m
z'	Uncorrected camera depth	m
z_{HS-6}	Corrected Hydroscat depth	m
z'_{HS-6}	Uncorrected Hydroscat depth	m

Acknowledgements

First and foremost Paul, without whom I would have lost it long ago. Tim for always providing a laugh and the oodles of particle guru–ness. Jon and John for excellent advice, always. Xiaodong, Gary and Karen for the lab help. Everyone involved in the Spring Bloom study but especially Sherry. Aurea for lab help and more. Richard for code and optics knowledge. Kristian for sharing Matlab frustration. Tony, because he always knew I could do it and more importantly, he told me so. Liz–impossible to thank her enough–for so much more than just computer knowlegde and mainly for the chuckles. Arran, Kirsty and Jen for the giggles and stress relief. Everyone else in the Oceanography department who has made my time much more bearable. Mom, Dad, Kris and Dani because they don't have a choice and they still care. Finally, to Chris who although he entered the game late, has been the most important player in the end.

Chapter 1

General Introduction

Light entering water is subject to attenuation – the removal of energy from the incident plane wave (Morel, 1991). Attenuation is the sum of both absorptive and scattering processes. Absorption results in loss of light energy (Kirk, 1994), whereas simple, elastic scattering merely affects the direction of propagation, and no energy loss is incurred (Morel, 1991). Most light entering the ocean is absorbed, but is also scattered at least once (Kirk, 1994).

Light scatter in natural waters is caused by water itself, dissolved salts, operationally defined as dissolved organics and inorganics and suspended material (Kullenberg, 1974). The scatter due to water and salts is attributed to small–scale density fluctuations and is identical in both the forward and backward directions (Kullenberg, 1974; Kirk, 1994) like Rayleigh scatter, and its value has been defined (Smith and Baker, 1981). The volume scattering function (VSF) describes the intensity of light scattered into a solid angle centered on a given angle by a unit volume of water illuminated by the incident light and is given by the equation

$$\beta(\theta, \lambda) = \frac{dI(\theta, \lambda)}{E(\lambda) dv}, \tag{1.1}$$

where $\beta(\theta, \lambda)$ is the volume scattering function for a given angle θ and wavelength λ, $dI(\theta)$ is the intensity of incident light that is scattered in direction θ, E is the incident irradiance and dv is the scattering volume (Kullenberg, 1974; Mobley, 1994). Scatter

can be further divided into both a forward and a backward component. The portion scattered into the backward direction is described using the backscattering coefficient which is defined as

$$b_b(\lambda) = 2\pi \int_{\frac{\pi}{2}}^{\pi} \beta(\theta, \lambda) \sin(\theta) d\theta \tag{1.2}$$

where $b_b(\lambda)$ is the amount of light of wavelength λ scattered into $\pi/2 \leq \theta \leq \pi$. The backscattering coefficient of any particular volume of water can be broken into the sum of its component parts

$$b_{bT}(\lambda) = b_{bw}(\lambda) + b_{bp}(\lambda) + b_{bdet}(\lambda) \tag{1.3}$$

were the subscript T is total, w is water, p is particulate matter and *det* is detrital material including matter that is operationally defined as dissolved ($< 0.45\mu$m).

The amount and colour of backscattered light from a volume of water can be related to the concentration, composition and size distribution of particles and detritus within the water. Because backscatter plays a key role in determining ocean colour observations by satellites, remote sensing potentially offers synoptic data on the particulate and detrital content of oceanic water over vast spatial scales. Reflectance ($R(0)$) of light from just below the water surface has been shown by both theoretical and empirical studies to follow

$$R(0) = f\left(\frac{b_b}{a}\right) \tag{1.4}$$

where b_b and a are the backscatter and absorption coefficients of the water and its constituents respectively. The functional relationship depends on the radiance distribution which is determined by factors such as solar zenith angle, sky conditions and sea state (Mobley, 1994). However, to link satellite observations to the concentration, composition and size distribution of particles and detritus requires clear understanding of how these variables affect the backscatter of light. The goal of this thesis is to examine how changes in the particulate size distribution during a spring phytoplankton bloom affect the backscattering coefficient.

The spectral dependence of the backscattering coefficient has been suggested to follow

$$b_{bp}(\lambda) \propto \lambda^{(3-\xi)} \tag{1.5}$$

where λ is wavelength and ξ is the exponent of the Junge particle size distribution (Ulloa *et al.*, 1994). Size distributions of suspended particulate matter are routinely described using the Junge–type power–law distribution for which the log number density function ($n_*(d)$) is of the form

$$n_*(d) = C\left(\frac{d}{d_0}\right)^{-\xi} \tag{1.6}$$

where d is the particle diameter, d_0 is the reference particle diameter (not necessarily equal to the minimum resolvable particle diameter), C is the number concentration of particles of size d_0 and ξ varies with environment. Typically, optical studies involving the Junge size distribution assume an ξ of 3–5 (for example Stramski and Kiefer, 1991; Ulloa *et al.*, 1994; Maffione and Dana, 1997). Any changes in the shape of the suspended particle size distribution is reflected in ξ and therefore in the wavelength dependence of the backscatter coefficient. The absolute value of ξ is highest when small particles dominate and decreases as larger particles increase. Spectral backscatter is expected to range from a shape that is peaked in the blues when small particles dominate to one that is spectrally flat when larger particles are more common.

A laboratory investigation by Conner and De Visser (1992) showed that optical backscatter sensors are more sensitive to changes in the particle size distribution less than 100μm than to those greater than 100μm. Using values of ξ>3, theoretical investigations into the effects of particle size on the backscattering coefficient have shown that it is in fact particles less than 10μm and particularly those less than 1μm that contribute the highest portion to backscatter (for example Morel, 1991; Stramski and Kiefer, 1991). Any changes in this optically important size range could change the dependence of the backscattering coefficient on wavelength.

Aggregation of suspended particulate matter changes the *in situ* particle size distribution. Flocculation of the suspended particles has been observed to occur rapidly,

particularly as phytoplankton blooms senesce, creating large ($> 100\mu m$) loosely aggregated particles called flocs (Smetacek, 1985; Kranck and Milligan, 1988; Alldredge and Gotschalk, 1989; Riebesell, 1991b, 1991a; Kranck and Milligan, 1992; Kepkay *et al.*, 1993; Kiorbe *et al.*, 1994; Li and Logan, 1995). The relatively rapid aggregation of suspended material will result in a marked change in the size distribution as larger particle sizes increase. However, it is unclear what the effects on the shape of the particle size distribution less than $100\mu m$, and therefore the spectral dependance of backscatter, will be when large appregates form.

Over the course of a previous study of the phytoplankton bloom in Bedford Basin, the suspended particle size distribution was observed to evolve as phytoplankton increased in number, aggregated and finally sank out (Kranck and Milligan, 1988). The present investigation combines *in situ* measurements of particle size distribution and spectral optical backscatter.

It is important that *in situ* observations of both the particle size distribution and the backscattering coefficient be made simultaneously. Once water has been sampled, fragile aggregates are broken and the size distribution is changed. Over the course of the bloom, an instrument frame housing a digital silhouette camera and a multi–wavelength backscattering sensor (Hydroscat–6) was used to obtain weekly profiles of the water column. Estimates of changes in the suspended particle size distribution are made from *in situ* silhouette photographs, and spectral backscatter measurements are made with the Hydroscat–6. Water samples were also collected to estimate the absorption coefficient. No previous study has collected simultaneous data of *in situ* particle size distributions and the variation in backscattering coefficient as a function of wavelength.

The Hydroscat–6 is the first commercially available backscatter sensor to measure at multiple wavelengths across the visible spectrum. However, its utility is limited by the quality of its estimates. The Hydroscat makes assumptions not only about the shape of the VSF, but also about the attenuation of the beam as it travels from source to receiver. The accuracy of the attenuation estimate and the correction for

it is evaluated. Backscattering measurements made over the course of this study are corrected using both the default correction method and one that uses the measured absorption. The goal is to assess the ability of the default correction algorithm versus that of a correction that uses measured optical properties of the water mass being studied.

Optical studies in the past have based predictions of the backscattering coefficient on Coulter Counter, microscopic or gravimetrically measured size distributions. Using such distributions, it has been found that particles less than 100μm dominate the backscatter signal (for example Stramski and Kiefer, 1991; Morel, 1991; Conner and Visser, 1992; Ulloa *et al.*, 1994; Mobley, 1994). However, these distributions are not measured *in situ*. In order to assess the effect on backscatter of particles greater than 100μm, the particle areal size distribution from a digital silhouette camera will be combined with Mie theory to predict a backscattering coefficient. These estimates are compared to the values measured by the Hydroscat. The goal is to assess the potential effects of large particles on the measured backscatter signal.

The digital silhouette camera provides a record of changes in the *in situ* particle size distribution greater than 100μm. Corresponding to each image, backscattering measurements within the visible spectrum were made. As the phytoplankton bloom grows and then senesces, the number of aggregates evolves. As the aggregation state of the water mass changes, a change in the shape of the backscatter spectrum may occur. The spectral shape of backscatter coefficient associated with images of differing size distributions are compared in order to determine if a change in spectral shape was observed with a change in the size distribution greater than 100μm. The null hypothesis is that with a change in the particle size distribution, no change in the slope of the spectral backscatter will occur. The alternative hypothesis is that with a change in particle size distribution, a change in the slope of spectral backscatter will be observed.

In this study, information is gathered to assess the accuracy of backscatter estimates and the potential effects of changing aggregate concentration and size distribution on the backscattering coefficient as a function of wavelength. The overall objective of this study is to observe simultaneous changes in the wavelength dependence of the backscattering coefficient and the *in situ* particle areal size distribution greater than $100\mu m$ over a spring phytoplankton bloom.

Chapter 2

Field Study

2.1 Introduction

Data were collected as part of the larger Spring Bloom 1998 study conducted by scientists at the Department of Fisheries and Ocean's Bedford Institute of Oceanography (B.I.O.). Once a week from February 26 to April 30, 1998, sampling was carried out from the Department of National Defense's Acoustic Barge located in approximately 45m of water in the mid-eastern portion of Bedford Basin, Nova Scotia (Figure 2.1).

Each week, an instrument frame containing a plankton digital silhouette camera, a conventional optical backscatter sensor and a multiwavelength backscatter sensor was profiled three times with the exception of April 9 when an additional fourth cast was carried out. Water samples were also taken at 5, 10, 20 and 40m throughout the study and an additional surface sample was taken from March 26 to April 30.

2.2 Methods

The multiwavelength optical backscatter sensor used in this study was HOBI Labs' Hydroscat-6 which measures backscattered light at 10nm wavebands centered on 442nm, 470nm, 510nm, 589nm, 620nm and 671nm. Detailed information about Hydroscat-6 is available in Maffione and Dana (1997).

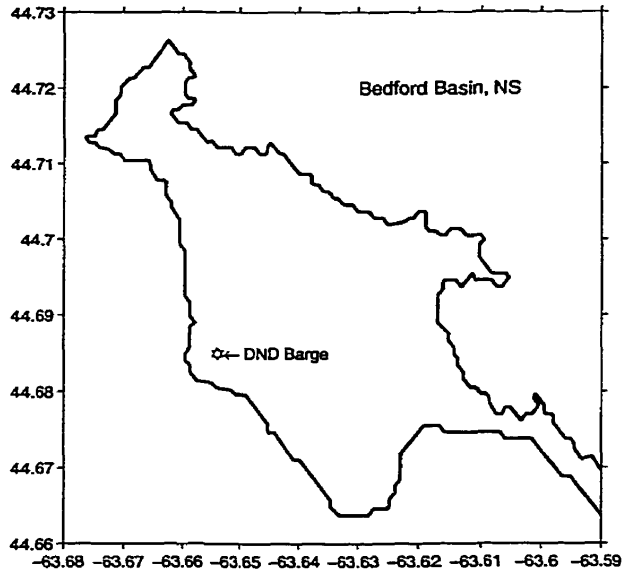

Figure 2.1: Site map of Bedford Basin, Nova Scotia. Site marked DND barge was the sampling site for this study.

Profiling speed of the instrument frame was approximately $0.3 m \cdot s^{-1}$. The Hydroscat was left at the surface for approximately five minutes to equilibrate with the water temperature on the first cast of each week and allowed to log for approximately one minute before it was lowered for every subsequent cast. The instrument was held for approximately one minute at 40m and 10m on the up and down profile during at least two casts weekly. Sampling rate of the Hydroscat was set at 2Hz.

All backscatter data are corrected using the HOBI Labs default correction algorithm and is presented minus the backscatter due to water as estimated by Smith and Baker (1981) unless otherwise noted. In order to increase confidence in the estimate and reduce noise, backscatter values were binned into half or one meter intervals to correspond to the measurements of either the depth of the discrete water sample used for absorption measurements or depth of the digital silhouette image.

The digital silhouette camera, a 1024X1024 pixel CCD (charge coupled device), resulted in between eighteen and 207 images per day. In all, 1428 images of good quality were taken. Images were analyzed with Media Cybernetics' Image-Pro Plus (IPP,

Version 3.1.1). A sub-sample of images was used to determine the best analysis technique. Final processing involved flattening the image to even out background colour (for more information IPP, 1997) and applying an area of interest set to 1004X1004 pixels to crop the image and eliminate the edge pixels that were affected by the flatten filter. For the count procedure, only pixels with a value of 226 or greater, on a grey scale of 0-255, were considered to be pixels representing particles. Further, only particles larger than four pixels (total area of $\sim 8300 \mu m^2$, equivalent circular diameter $\sim 100 \mu m$) were included to eliminate noise. IPP particle counts were exported to a Microsoft Office97 Access database where particle areas were converted to equivalent circular diameter and volume as

$$D = \sqrt{\frac{4 \cdot A}{\pi}} \tag{2.1}$$

and

$$V = \sqrt{\frac{16 \cdot A^3}{9 \cdot \pi}} \tag{2.2}$$

where A is the sum of pixel areas. Pixel size was $43.7 \mu m$ by $43.7 \mu m$ square. All particles in an image were binned into one of 28 size classes based on an equivalent circular diameter class separation of $\frac{1}{3}\phi$ units where

$$\phi = \frac{-\ln D(mm)}{\ln 2} \tag{2.3}$$

Number concentration within each size class is the sum of all particles with equivalent circular diameters that fall within the boundaries of that class. Binned particle data were produced for number, area and volume of particles in each size class.

From March 26 to April 30, absorbance measurements from surface, 5, 10, 20 and 40m were made except for March 26 for which only the surface and 5m samples were used. The absorbance technique was a modified version of that described in Ciotti (1999) (see also Yentsch, 1962; Mitchell and Kiefer, 1983; Kishino *et al.*, 1985; Mitchell and Kiefer, 1988). Samples of $\sim$500mL were filtered with low vacuum pressure (<5 mm Hg) through Whatman GF/F filters with nominal pore size $0.7 \mu m$.

All filtration was completed within four hours of sampling and samples were stored in dark bottles and kept cool between sampling and filtration to minimize biological changes. Absorbance measurements were made using a Cary 13 spectrophotometer. Total particulate (pigmented) and detrital absorbance measurements were performed using filter holders designed to hold the filter close to the light sensor in order to maximize the collection of forward scattered light. To obtain non-pigmented absorption, filter organic extractions were performed with a minimum of 25mL of methanol and left to extract until no chlorophyll was evident in the absorbance spectra (Kishino *et al.*, 1985, see also). All filter absorbance measurements were made with a reference, blank filter that was first saturated with double filtered source seawater then flushed with 25mL of methanol for the extracted sample. Care was taken that both reference and sample filters remained saturated during measurement. Dissolved absorbance was measured using the filtrate from each depth. Samples were placed in 10cm quartz cuvettes, and care was taken such that all bubbles were omitted from the sample and cuvette ends were clean. Reference cell solution for the dissolved fraction was Super–Q, reagent grade water.

A single wavelength, infrared, D&A Instrument Company model OBS–3 optical backscatter sensor (OBS) was deployed on the instrument frame. Although the uncalibrated IR backscatter measurements were not used in this study, the pressure sensor on the OBS provided the most consistent and reliable depth readings and therefore was taken as the 'true' measure of instrument frame depth. The Hydroscat depth showed a cast–number dependent offset to that measured by the OBS. For days when OBS data was unavailable (March 26 and April 30) Hydroscat depth was corrected according to

$$\begin{aligned} o_1 &= 0.04 \cdot z'_{HS-6} + .614 \\ o_2 &= 0.046 \cdot z'_{HS-6} + .97 \end{aligned} \tag{2.4}$$

where o_1 is the offset for the first cast, o_2 is the offset for the second cast and z'_{HS-6} is the uncorrected Hydroscat depth. Equation 2.4 was developed as the average relationship between the OBS and Hydroscat measured depth from all days for which OBS

depth measurements were available. The new Hydroscat depth, z_{HS_6}, was calculated as

$$z_{HS-6} = z'_{HS-6} - o_i \tag{2.5}$$

where z'_{HS-6} is as defined above and o_i is the offset for the particular cast (i=1 or 2).

The depth sensor in the digital silhouette camera gives anomalous values for depths less than 20m because of uneven power supply. It was possible to use the values greater than 20m to estimate the values less than 20m. A fit specific to the cast values greater than 19m gave the best results. However, because the instrument was often left to log for extended periods at 5m or 10m and the offset between measured and actual depth was non–linear, a fifth–order polynomial fit was used to correct the camera depth for casts where logging at a particular depth occurred

$$\begin{aligned} z \;=\; & -6 \times 10^{-5} \cdot (z')^5 + 2.9 \times 10^{-3} \cdot (z')^4 - 4.3 \times 10^{-2} \cdot (z')^3 \\ & +0.17 \cdot (z')^2 + 1.21 \cdot z' + 2.08 \end{aligned} \tag{2.6}$$

where z' is the uncorrected camera depth and z is the resulting corrected value. The equation was calculated from the relationship between the output depths from the camera and those that were calculated as specific trends for casts that did not have extended logging periods.

Scientists from B.I.O. deployed a CTD weekly. This data included salinity and temperature as well as a relative measure of chlorophyll *a* from a fluorometer. All data were binned into half meter bins. For more information on the methods for the CTD data collection see Li *et al.* (1998).

2.3 Results

2.3.1 CTD Data

Values of density (kg·m^{-3}) calculated from the salinity and temperature measured by the CTD are displayed in the fourth panel of Figures A.1–A.10. Also shown

in these figures is chlorophyll *a* ($\mu g \cdot L^{-1}$) estimated from a fluorometer calibrated after completion of the bloom study with chlorophyll samples taken during the study period.

Density remained fairly constant throughout the study, particularly below five meters. The surface waters contained the most variability, particularly on February 26 when density in the surface waters (<5m) dropped dramatically as a result of the infusion of freshwater from the Sackville River and basin catchment caused by a storm in the days prior to sampling.

The evolution of chlorophyll *a* estimates can be used as a proxy for bloom dynamics. Chlorophyll begins to increase in water at depths less than ten meters by March 12 (Figure A.3) and peaks to nearly $15 \mu g \cdot L^{-1}$ at roughly five meters on March 19 (Figure A.4). The chlorophyll maximum broadens spatially and decreases in magnitude after this until April 16 (Figure A.8) when the maximum is distributed to nearly 20m. By April 23 (Figure A.9), chlorophyll values have decreased to $\sim 3 \mu g \cdot L^{-1}$. Figure 2.2 shows chlorophyll *a* values averaged over one meter intervals for surface, 5, 10, 20 and 40m during the bloom. Note that chlorophyll values in water deeper than 20m remain fairly constant and low throughout the bloom. This figure more clearly shows the slight rise in chlorophyll on March 12 although the peak on March 19 evident in Figure A.4 is not reproduced. Figure 2.2 also demonstrates the final decline on April 23 and by April 30 chlorophyll values at all depths are almost equal and relatively low.

Using this chlorophyll evolution as a proxy for plankton populations, it is estimated that the bloom was beginning in the surface waters of March 12, marginally decreased on March 26 only to resurge by April 2. The bloom began to decline around April 16 and had declined by April 23.

2.3.2 Particle Size Distribution

The size distributions greater than $100 \mu m$ seen in the images from the digital silhouette camera throughout the study are displayed in the first panel of Figures A.1–A.10. Typical areal size distributions are either flat or have negative slopes indicating that

most particles (in number) in the images are less than 500μm. Qualitative assessment of the images shows that the majority of visible particles are composed of mainly small chains and unidentifiable roughly circular particles. Larger particles begin to appear in the images from surface waters on March 12 and 19th as is indicated by size distributions that extend beyond 1000μm and remain flat or have positive slopes on the area size distributions. Gradually, images with larger particles are seen at deeper depths, down to ~25m on April 16. Size distributions move back to more typical distributions with few particles larger than 500μm by April 23 and 30th.

Figure 2.3 is an image from April 16 with many large particles showing the stringy nature of the aggregated chain flocs. Figure 2.4 is an image from March 5 that displays the typical size and nature of most images seen throughout the study. Notice that in this image there are few chains and most of the background particles are roughly circular.

2.3.3 Backscatter

The magnitude and spectral shape of backscatter varied throughout the study. Qualitatively, backscatter as a function of wavelength changes more between days than with depth on a given day. This is particularly evident on February 26, March 5, 12th, 19th and April 30 (Figures A.5, A.2, A.3, A.4 and A.10) when spectra with depth are similarly shaped. April 9, 16th and 23rd (Figure A.7, A.8 and A.9) have the least consistency between the shape of backscatter as a function of wavelength over the depth of the profile. Overall, the spectra are generally humped at 510nm with the value at 671nm the lowest.

The magnitude of backscatter has a range of over an order of magnitude. The highest values were seen in the surface waters of February 26 with a value of $\approx 0.2 m^{-1}$ at any wavelength. This is the week that a storm in the days previous to sampling caused an increase in freshwater inflow to the basin. Surface waters were observed to be a light tan colour, which was likely caused by an increase in the inorganic suspended material resulting in the high values of measured backscatter. Unfortunately, since

the surface waters contained more fresh water than the underlying, the mixing of the two water masses resulted in images from the digital camera that were not clear so an assessment of the particles visually is not possible. By 5m, backscatter had dropped over an order of magnitude to $\sim 0.01 m^{-1}$. This value was much more typical of the values seen for the rest of the study. For the first part of the study (February 26 to March 19), values of backscatter hovered around $0.01 m^{-1}$. During this period, the profiles of backscatter varied with depth. Most interesting is the peak at 5m on March 19 which is correlated with a peak in estimated chlorophyll a (see Figure A.4). For both April 2 and 9th, the surface waters have backscatter peaked at $\sim 0.01 m^{-1}$ (Figures A.6 and A.7) but values drop to $\sim 0.005 m^{-1}$ by 10m. April 16 (Figures A.8) has a slightly higher backscatter in the 5-25m region but, values drop below $0.005 m^{-1}$ below this region. Finally, on April 23 and 30th the measurements of backscatter values are relatively constant with depth at values $\sim 0.005 m^{-1}$ (Figures A.9 and A.10).

2.3.4 Absorption

Measured absorption (a_T, a_{phyt}, a_{DOM} and a_{det}) is displayed in Figures C.1–C.6. The highest absorption values in the blue region of the visible wavelengths (400–500nm) were seen in the surface waters of the late stages of the bloom, specifically between April 9 and April 23. The absorption in the red region (650–700nm) of the visible spectrum was relatively constant throughout the study. This is not unexpected since absorption in this region is mainly due to water. Over the spectrum, the largest changes occur in the region less than 500nm. The most dramatic example occurs at depths greater than 20m on April 2 when the blue region of the spectrum has the lowest values of the study.

2.4 Discussion

The evolution of the bloom, as estimated from the chlorophyll a values, corresponds well to the major data collected in this study. As the chlorophyll values first begin

to rise in the surface waters of March 12 and 19th, the first large particle aggregates also appear. Aggregates begin to dominate the surface waters by March 26 and the absolute value of the backscattering coefficient drops, particularly below 10m in depth. The bloom peaks on April 9 and is waning on April 16 when the largest and most highly concentrated aggregates are observed. It is also during these weeks that the highest absorption in the blue region is observed. By April 23, chlorophyll values have dropped and aggregates have almost disappeared from the water column. On April 30, measured chlorophyll and backscatter are at their lowest values and aggregates have completely disappeared from the water column.

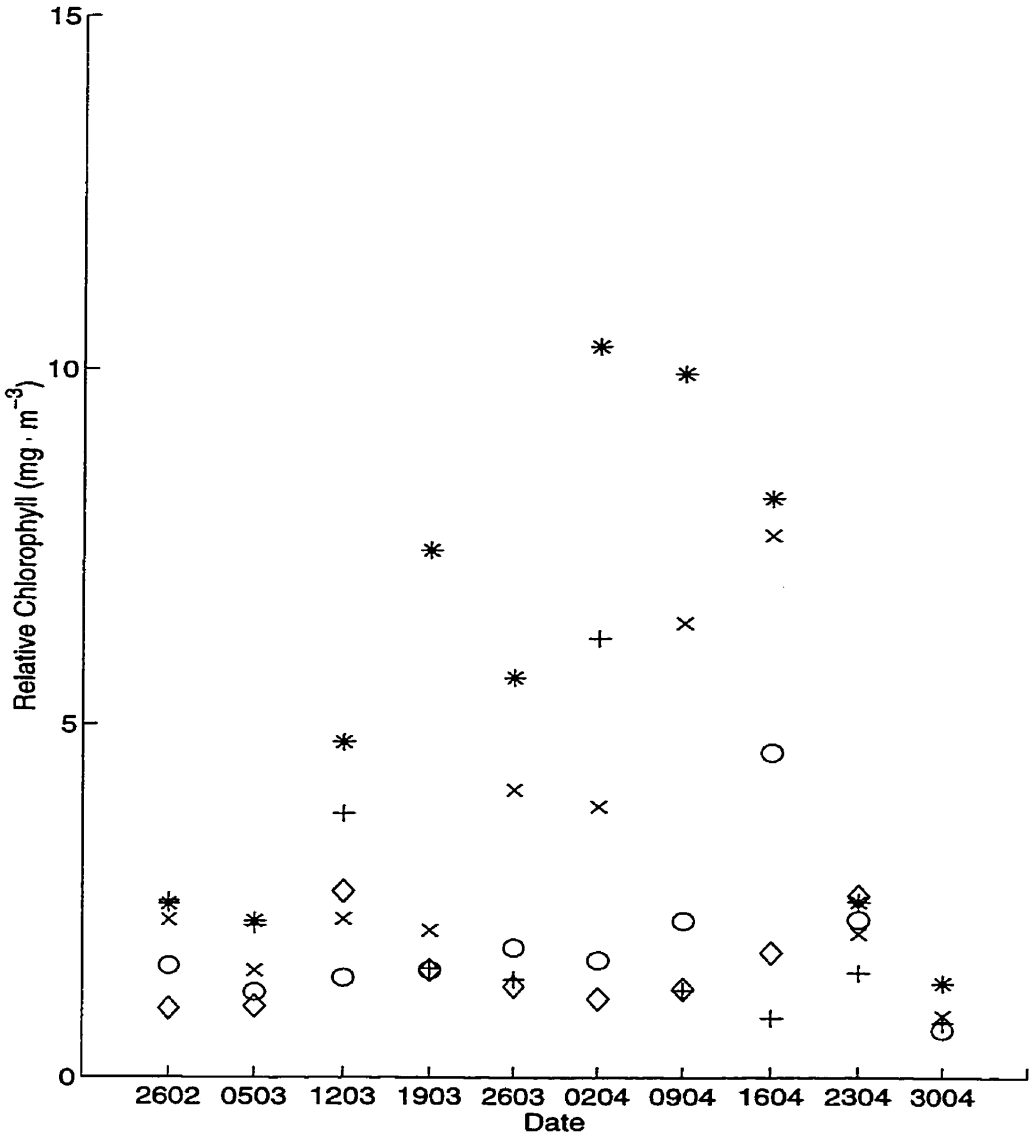

Figure 2.2: Plot of chlorophyll *a* averaged over one meter at the surface, 5, 10, 20 and 40m from February 26 to April 30. Symbols are + surface, $*$ 5m, $\times$ 10m, $\circ$ 20m and $\diamond$ 40m.

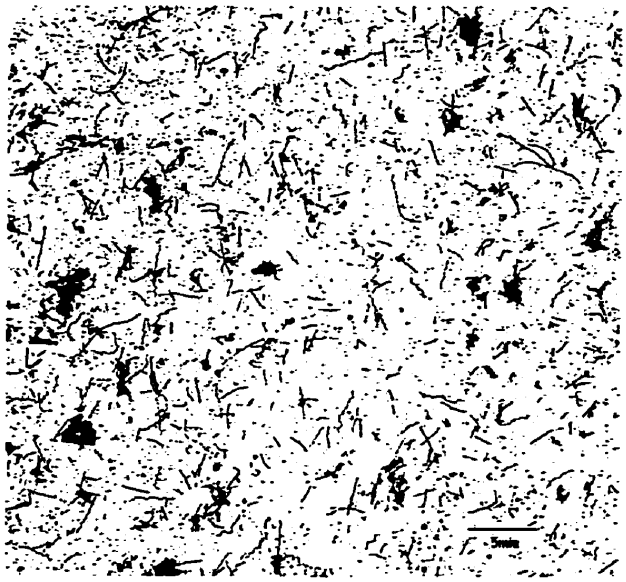

Figure 2.3: Digital silhouette image taken April 16, 1998 at approximately 2m. Note the 5mm scale bar.

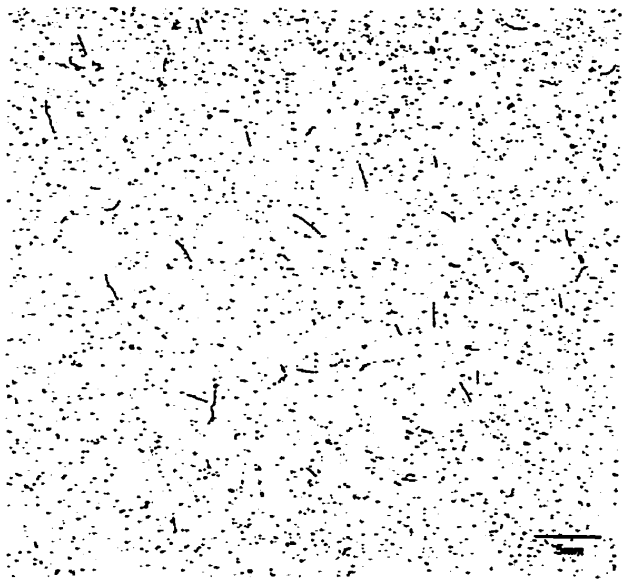

Figure 2.4: Digital silhouette image taken March 5, 1998 at approximately 2m. Note the 5mm scale bar.

Chapter 3

Assessment of Algorithms for Correcting Backscattering Measurements made by the Hydroscat–6

3.1 Introduction

In situ measurement of backscatter is fundamentally important to ocean colour remote sensing because the measured signal is a function of the light scattered into the backward direction by the water and associated matter. Accurate measurement of backscatter is necessary in order to elucidate the link between the remotely sensed signal and the water constituents that affect both the colour and magnitude of light reflected from ocean water. Suspended and dissolved matter composition, concentration and size distribution can be inferred from the spectral shape and intensity of light measured by the remote sensor (Maffione and Dana, 1997; Roesler, 1998). As such, the lack of attention to measurement of *in situ* backscatter is unfortunate.

The Hydroscat–6 (HOBI Labs) is the first commercially available multiwavelength

backscatter sensor. It is calibrated to generate an estimate of the backscattering coefficient (m^{-1}). However, between the source and receiver, light from the instrument LED is attenuated. In particular, absorption modifies the light field spectrally. To account for the effect of attenuation along the path of the beam, a correction factor must be applied. The Hydroscat default correction approximates how typical ocean water would attenuate light. However, with additional information about water constituents or other optical measurements, the user can apply a more specific attenuation correction. The goal of this study is to assess the effects of different attenuation corrections using both the default value and one calculated from other measured optical properties.

3.2 Methods

Backscatter at six wavebands centered on 442, 470, 510, 589, 620 and 671nm was measured using the Hydroscat-6 from the Naval Acoustic barge in Bedford Basin, Nova Scotia (see Figure 2.1). Two profiles were made weekly from February 26 to April 30, 1998 over the course of a spring phytoplankton bloom. From March 26 to April 30, 1998, water samples at the surface, 5, 10, 20 and 40m were taken, and absorption measurements were made.

3.2.1 Correction of measured backscatter

The Hydroscat measures at one angle of the volume scattering function (VSF)–$\sim$135° to $\sim$140° depending on the attenuation efficiency of the water and its constituents. An assumed shape of the VSF is then used to convert the measured value to an estimate of the backscatter coefficient (for details see Maffione and Dana, 1997). Between the LED source and receiver, light is attenuated. In order to account for this loss of light, a pathlength attenuation correction factor (σ) is used. Much of the following about the correction of the Hydroscat measured backscatter is taken from a HOBI Labs user manual (HOBI Labs, 1999).

The attenuation for the Hydroscat LED is actually less than beam attenuation (c). The LED pathlength attenuation coefficient, K_{bb}, is approximated as

$$K_{bb}(\lambda) \cong .75 \cdot b(\lambda) + a(\lambda) \tag{3.1}$$

where b is the total scattering coefficient and a is the total absorption coefficient. K_{bb} can also be parameterized in terms of the backscattering ratio ($\tilde{b_b} = b_b/b$) and the single-scattering albedo ($\omega_o = b/c$) to give

$$\begin{aligned} K_{bb}(\lambda) &= \left(\frac{1}{\omega_o(\lambda)} - .25\right) \cdot \frac{b_b(\lambda)}{\tilde{b_b}(\lambda)} \\ &= \eta(\lambda) \cdot b_b(\lambda) \end{aligned} \tag{3.2}$$

where η is a defined parameter that incorporates $\tilde{b_b}$ and ω_o and parameterizes K_{bb} as a function of backscatter.

The pathlength attenuation correction for the LED from source to receiver is calculated using K_{bb} as

$$\sigma(\lambda) = k_0(\lambda) + k_1(\lambda) \cdot K_{bb}(\lambda) + k_2(\lambda) \cdot K_{bb}^2(\lambda) \tag{3.3}$$

where k_i (i=0, 1, 2) are specific instrument calibration constants. The σ correction can be estimated with Equation 3.3 and pathlength attenuation calculated using either Equation 3.1 or 3.2. Measured b_b is corrected for water pathlength attenuation as

$$b_b(\lambda) = b_b'(\lambda) \cdot \sigma(\lambda) \tag{3.4}$$

where b_b' is the raw backscatter measurement from the Hydroscat that has not yet been corrected for pathlength attenuation. The default correction of backscatter measurements as provided in the Hydroscat software is carried out using the attenuation coefficient estimated with Equation 3.2 with an η=50. The value of η is meant to approximate how typical ocean water would attenuate light.

3.2.2 Absorption estimation

To determine absorption, absorbance measurements were made using a Cary 13 spectrophotometer. Samples were filtered through Whatman GF/F filters with nominal pore size 0.7μm to collect suspended particulate material. Extraction of pigment material from the filters was performed with at least 25mL of methanol or until no chlorophyll was evident in the spectra. Both the pigmented and extracted material absorbance measurements were made using filter holders designed to hold the sample and reference filters close to the light sensor. Reference filters were wetted and kept moist with double filtered source sea water for the pigmented particulates and then flushed with 25mL of methanol for the extracted particulates. Dissolved matter absorbance was measured using the filtrate from each sample placed in 10cm quartz cuvettes with Super-Q water as reference solution.

Filter pad absorbance were corrected according to

$$a(\lambda) = \frac{1}{\log_{10} e} \cdot \frac{D'_f(\lambda) - D'_{fmean(750-800)}}{\gamma \cdot \ell} \tag{3.5}$$

where D'_f is the measured absorbance, $D'_{fmean(750-800)}$ is the mean absorbance from 750-800nm, γ is the pathlength amplification correction factor and ℓ is geometric pathlength (volume filtered over the filter pad effective area) (Kishino *et al.*, 1985; Roesler, 1998). The values from 750–800nm are subtracted out to correct for loss due to scatter because this wavelength band is considered to have negligible absorption by particulates (Roesler, 1998). The value for γ was calculated following

$$\gamma = 1 + .39 \cdot D'_f(\lambda)^{-.69} \tag{3.6}$$

as was calibrated by Aurea Ciotti for the spectrophotometer used (Aurea Ciotti personal communication, 1999). Dissolved absorbance measurements were corrected as

$$a_{DOM}(\lambda) = \frac{1}{\log_{10} e} \cdot 10 \cdot (D'_c(\lambda) - a_o) \tag{3.7}$$

where D'_c is the dissolved absorbance from the cuvette, and a_o is the asymptotic value of the exponent relationship between the dissolved absorbance and wavelength and is

defined as

$$D'_c = a_1 \cdot e^{-\lambda \cdot s} + a_o \tag{3.8}$$

where a_1 is the intercept, s is the slope and a_o is the asymptotic value of the relationship (Sophie Johannessen personal communication, 1999). The offset from zero for the relationship between D'_c and wavelength at wavelengths greater than 750nm is then approximated by a_o.

The values for particulate and dissolved absorption were combined with values of absorption due to water from Pope and Fry (1997) to give estimates of total absorption, a_T with wavelength since

$$a_T(\lambda) = a_p(\lambda) + a_{DOM}(\lambda) + a_w(\lambda) \tag{3.9}$$

where the subscripts stand for p, DOM and w are particulate, water and dissolved respectively.

3.2.3 Comparisons between correction algorithms

Measured absorption coefficients were available from March 26 to April 30. Uncorrected backscatter estimates were corrected using pathlength attenuation coefficients (K_{bb}) calculated both with Equation 3.1 and Equation 3.2. For backscatter corrected with η, the Hydroscat software default η=50 value was used. For backscatter corrected with the measured absorption, a value for the total scattering coefficient (b) had to be estimated since it was not measured. To do this, the uncorrected backscatter (b'_b) and an estimated value for the backscattering ratio ($\tilde{b_b}$) were used to estimate b as

$$b(\lambda) = \frac{b'_b(\lambda)}{\tilde{b_b}} \tag{3.10}$$

Four values of the backscattering ratio, $\tilde{b_b}$=0.01, 0.02, 0.03 and 0.04, were chosen to encompass most natural water from turbid ($\tilde{b_b}$=0.01) to clear ($\tilde{b_b}$=0.04) (HOBI Labs, 1999). The estimated value for $b(\lambda)$ and the measured value of $a(\lambda)$ were

inserted into Equation 3.1 and Equation 3.3 and finally into Equation 3.4 to give a pathlength attenuation corrected value of the backscattering coefficient. Iteration of Equation 3.10 using corrected estimates of backscattering coefficient in order to better approximate b, did not result in considerable changes to the final estimates of the backscattering coefficient. The change in the final estimate of backscatter was, in fact, larger between estimates of the backscattering ratio than the change that resulted from iteration to estimate the scattering coefficient.

Absorption measurements were made at five discrete depths whereas, the Hydroscat measurements were continuous profiles. Therefore, uncorrected backscatter estimates within half a meter of water sample depth were averaged to give a one meter binned uncorrected estimate. Further, the Hydroscat wavelengths actually represent the median of 10nm wavebands. Therefore, absorption measurements used in the correction were the mean of the values within five nanometers of the central Hydroscat–6 wavelength.

Once corrected estimates were calculated, backscatter due to water was estimated from Smith and Baker (1981) and subtracted. The difference between backscatter corrected with the default algorithm (with η=50) and those corrected with the measured absorption and estimated $\tilde{b_b}$ was calculated. Finally, the percent difference was calculated as the difference divided by the default corrected value.

$$\% \text{ diff} = \frac{b_{bp(\eta)}(\lambda) - b_{bp(.75 \cdot b_{est}(\lambda)+a(\lambda))}(\lambda)}{b_{bp(\eta)}(\lambda)} \cdot 100\% \tag{3.11}$$

3.3 Results

The correction of backscatter using the η parameter estimate versus using measured absorption has two potential consequences. The first is the over- or under–estimation of the magnitude of backscatter that arises from inaccurate estimates of the LED pathlength attenuation factor. The second is an inaccurate spectrum for backscatter that could arise because of the wavelength invariance of the default η correction.

Appendix B (Tables B.1–B.4) gives the percent difference for all depths and days

and $\tilde{b_b}$=0.01, 0.02, 0.03 and 0.04. The difference between backscatter corrected with the default algorithm (η=50) and that corrected using measured absorption and estimated backscatter ratio ranges from no difference (April 2 at 20m, 589nm with $\tilde{b_b}$=0.04) to nearly -25% (April 16 at the surface, 442nm with $\tilde{b_b}$=0.01).

Table B.1 shows that the largest percent differences are seen for $\tilde{b_b}$=0.01. Further, all of these values are negative, meaning that with $\tilde{b_b}$=0.01, the default algorithm correction results in backscatter that is the most different and lowest compared with backscatter corrected with measured absorption and estimated scatter. When the backscattering ratio is estimated as 0.02 (Table B.2), a positive percent difference between the correction algorithms is found for April 2 at 40m in the blue to green portion of the spectra. The percent difference decreases when the backscattering ratio is estimated as 0.03, and many positive differences are found (see Table B.3). The smallest differences between the correction algorithms is found when the backscattering ratio is estimated as 0.04 (Table B.4). Although there are still many negative percent differences, more positive percent differences are seen than for the other estimates of the backscattering ratio. This indicates that when $\tilde{b_b}$ is estimated as 0.04 the two correction algorithms are most similar.

The water column of Bedford Basin is fairly turbid and therefore a backscattering ratio of 0.02 is likely a good estimate of what the true value may be. As such, a more in–depth look at the effect of day and depth on the absolute percent difference between the two correction methods was undertaken for $\tilde{b_b}$=0.02. The absolute difference is used since the magnitude of the difference between the correction algorithms is of interest and means are calculated for which adding positive and negative differences would mask the true magnitude of the average difference. Tables 3.1 and 3.2 present the absolute mean and standard deviation for each day and depth respectively. The overall mean and standard deviation for all days and depths for each wavelength are presented in Table 3.3.

The absolute mean percent difference between backscatter corrected with the default correction and that using measured absorption values moderately varies with

Table 3.1: Mean and standard deviation of the absolute percent difference between the default correction and that using absorption measurements with $\tilde{b_b}$=0.02 for day averaged across depth.

			Percent Difference					
Day		# depths	442nm	470nm	510nm	589nm	620nm	671nm
26/03/98	$\overline{\lvert x \rvert}$	2	9.79	4.89	2.93	1.61	3.68	10.52
	SD		0.95	0.68	0.63	0.11	0.09	0.32
02/04/98	$\overline{\lvert x \rvert}$	5	3.43	1.72	0.86	1.55	3.59	10.67
	SD		2.76	1.54	0.86	0.35	0.34	1.19
09/04/98	$\overline{\lvert x \rvert}$	5	6.60	2.81	1.50	1.60	3.69	10.94
	SD		4.39	2.07	1.14	0.31	0.27	0.83
16/04/98	$\overline{\lvert x \rvert}$	5	7.72	3.33	1.72	1.47	3.62	10.15
	SD		6.04	2.94	1.73	0.72	0.41	0.56
23/04/98	$\overline{\lvert x \rvert}$	5	5.75	2.47	1.29	1.50	3.60	9.95
	SD		2.90	1.43	0.89	0.29	0.28	1.32
30/04/98	$\overline{\lvert x \rvert}$	5	2.85	1.17	0.53	1.39	3.51	10.00
	SD		0.87	0.49	0.20	0.08	0.09	0.54

day and depth. The lowest mean difference is seen on April 2, 23 and 30th, after the bloom, while the highest is seen on March 26, April 9 and 16th. However, the high mean value on March 26 may be a result of limited absorption values and a mean based on only surface and 5m backscatter estimates. Depth seems to give a more obvious change in mean percent difference. The highest percent differences are seen for the surface, 5m and to a lesser degree, 10m. Lower percent differences are seen for the 20m and 40m corrected values.

The standard deviation is a measure of the dispersion or spread of the data. April 30 which had the lowest absolute mean values also had the lowest spread in the data meaning that the percent difference for the two correction algorithms for depths on April 30 is fairly constant. Similarly, the largest standard deviations are observed when the absolute percent differences are highest on April 9 and 16th (see Table 3.1). The same is observed for depth where the lowest mean percent differences are associated with the lowest spreads (20 and 40m) and the largest differences have

Table 3.2: Mean and standard deviation of the absolute percent difference between the default correction and that using absorption measurements with $\tilde{b_b}$=0.02 for all depths averaged over all days.

			Percent Difference					
Depth		# days	442nm	470nm	510nm	589nm	620nm	671nm
Surface	$\overline{\lvert x \rvert}$	6	9.95	4.58	2.46	1.79	3.77	10.18
	SD		5.12	2.42	1.55	0.61	0.46	1.00
5m	$\overline{\lvert x \rvert}$	6	6.60	3.01	1.54	1.40	3.52	10.04
	SD		2.62	1.34	0.96	0.21	0.14	0.50
10m	$\overline{\lvert x \rvert}$	5	5.57	2.52	1.34	1.50	3.69	10.79
	SD		1.80	0.81	0.54	0.22	0.25	1.10
20m	$\overline{\lvert x \rvert}$	5	2.69	0.96	0.49	1.34	3.48	9.96
	SD		1.38	0.65	0.30	0.29	0.14	0.63
40m	$\overline{\lvert x \rvert}$	5	2.15	0.86	0.44	1.46	3.56	10.92
	SD		1.35	0.63	0.33	0.20	0.13	1.11

the largest standard deviations (surface) (see Table 3.2).

Perhaps the most noteworthy effect on the calculated percent difference between the two correction algorithms is seen between wavelengths. Table 3.3 gives the absolute mean and standard deviation of the percent difference for all days and depths for each wavelength. The highest mean percent difference between the two algorithms is seen for 671nm. Further, the standard deviation at 671nm is fairly low meaning that the difference is fairly constant with depth and day. The absolute mean value does not include the sign of the difference between the correction algorithms but Table B.2 in Appendix B shows that the percent difference at 671nm is always negative meaning that backscatter calculated with the default correction using an η=50 is always less than that corrected using measured absorption by about 10%. Wavelength 442nm has the next highest percent difference but more interestingly it has the highest standard deviation indicating a larger spread in the percent difference between the algorithms. In fact, the range in percent difference is from 0.16% to -18.17% (see Table B.2 in Appendix B). Therefore, at 442nm, the correction that uses the absorption

Table 3.3: Mean and standard deviation of the absolute percent difference between the default correction and that using absorption measurements with $\tilde{b_b}$=0.02 for all days and depths.

	# data points	Percent Difference					
		442nm	470nm	510nm	589nm	620nm	671nm
$\|\bar{x}\|$	27	5.61	2.49	1.31	1.51	3.61	10.36
SD		4.00	1.95	1.15	0.37	0.27	0.92

measurements is the most variable in how it deviates from the η correction algorithm. The smallest percent differences between the two correction algorithms occurs in the mid-spectrum at 510nm and 589nm.

Since wavelength was seen to have the largest effect on the absolute percent difference between the backscatter corrected with the two algorithms, there should be some visible effect of correction algorithm on the shape of backscatter with wavelength. Figure 3.1 shows backscatter normalized to the value at 442nm for the five absorption sample depths on April 30, 1998. The normalized spectra for all days are given in Appendix B, Figures B.1–B.5.

Although each correction algorithm results in points that are only slightly different, the shape of backscatter with wavelength does change with the largest differences visible in the red end of the spectrum. It is interesting that the spectra flatten and become less variable between correction algorithms with depth. By 40m on April 30, the points lie virtually on top of each other.

3.4 Discussion and Conclusions

The effect of correction method on the absolute value and spectral shape of backscatter measured by the Hydroscat–6 was assessed for measurements made from March 26 to April 30, 1998 in Bedford Basin, NS. The largest absolute percent difference between the default correction method and the method incorporating measurements

of absorption was ~25%. The shape of backscatter with wavelength is affected by correction algorithm and the effect is largest at the ends of the visible spectrum.

Most of the percent differences between backscatter corrected with the default η correction and those corrected with measured absorption are negative. That is for most days, depths and wavelengths, the default correction results in a lower backscatter coefficient relative to that corrected with measured absorption. The default correction with η=50 underestimates the pathlength attenuation correction that is estimated with the measured absorption. The amount of difference between K_{bb} estimates, and therefore the corrected backscatter coefficient estimates, depends on the value of $\bar{b}_b$ used to estimate the scattering coefficient. While for some water, this indicates that estimating pathlength attenuation with an η=50 will be sufficient, it also indicates, that for others it will be insufficient.

When the attenuation of the water and its components is low and little pathlength attenuation correction is required, the sigma correction (see Equation 3.3) makes little difference in the backscatter estimation (Maffione and Dana, 1997). Further, the sigma correction is only a weak function of attenuation (Maffione and Dana, 1997) since k_1 in Equation 3.3 has a value of ~0.12 and k_2 has a value of ~0.02. The estimated pathlength attenuation, when multiplied by these factors, must be fairly large to cause a large change in the value of the sigma correction factor.

When total absorption is high, it can be expected that the η estimate of pathlength attenuation will be worse. Figure 2.2, shows the relative chlorophyll measured throughout the bloom. The highest chlorophyll, which I use as a proxy for phytoplankton population changes, is observed at depths less than 10m for March 26 to April 16. This is also when the highest absolute percent differences are seen (see Table 3.1) with the exception of April 2 when the percent difference is lower. Further, the points in Figure 2.2 that correspond to depths deeper than 20m have the lowest chlorophyll for all days. The lowest percent differences are seen for these depths, supporting the conclusion that absorption from phytoplankton populations will result in the largest difference between the default correction algorithm and one using

measured optical properties.

The highest percent difference for all values of $\tilde{b_b}$ occurs on April 16 in the surface waters. Figure 3.2 shows the measured absorption for this day and depth. The measured a_{DOM} is exceptionally high. When absorption is high, the pathlength attenuation correction estimated with the η parameter will under–estimate the effects of absorption and therefore under–estimate pathlength attenuation and its correction, resulting in a final estimate of backscatter that is lower than that corrected with the measured absorption.

The effect of wavelength on the mean absolute percent difference also points to an effect of absorption by chlorophyllous particles since the largest difference between correction algorithms is seen for 442nm, which is in the absorption band of chlorophyll. Further, absorption at 442nm will change depending on the concentration of chlorophyll and therefore absorption in this region of the spectrum. The highest percent differences between algorithms are seen on days and at depths with high relative chlorophyll concentrations, for example March 26 and for surface, 5 and 10m depths on April 9 and 16th. This is also supported by the high standard deviation of the absolute percent difference found for 442nm as seen in Table 3.3.

Since the percent differences at 671nm are always negative, regardless of backscattering ratio estimate (see Tables B.1–B.4), the default parameter η always under–estimates the pathlength attenuation correction factor at 671nm. The absorption due to water is highest in this region of the visible spectrum. This is also the region for which absorption was seen to be most constant throughout the study (see Figures C.1–C.6), explaining why the standard deviation of the mean absolute percent difference was the lowest.

The correction algorithm that uses measured absorption provides wavelength dependent correction that the default η correction does not. Given that days and depths with high chlorophyll measurements resulted in the largest absolute percent differences between correction algorithms, water that is expected to have high or variable absorption would be most susceptible to inaccurate correction if the default correction

algorithm was used.

Results suggest that the absolute percent difference between correction algorithms on the final backscatter coefficient estimates are at most 25% and typically 10% or less. However, there are differences between wavelengths, days and depths. Therefore, when possible, independent measurements of absorption and scattering should be made to properly correct the backscatter coefficient. Particularly so that wavelength dependence is brought into the correction algorithm. Unfortunately, since absorption measurements were not made for this entire study, the default correction algorithm with η=50 is used throughout this document.

A more detailed study of different water types, particularly oligotrophic, would elucidate the effects of different correction algorithms on the value of backscatter measured by the Hydroscat–6. Further, *in situ* measurement of absorption and total scattering with the same spatial resolution as the Hydroscat, for example by also profiling an AC–9 (WetLabs) to measure estimates of absorption and attenuation, would provide a more comprehensive comparison between algorithms. Finally, the η parameter is not fixed at 50. Varying its value in a way that reflects water column properties and comparing results to those obtained using optical measurements could be a further step to investigate the potential effects of different pathlength attenuation correction algorithms on the final estimate of the backscattering coefficient.

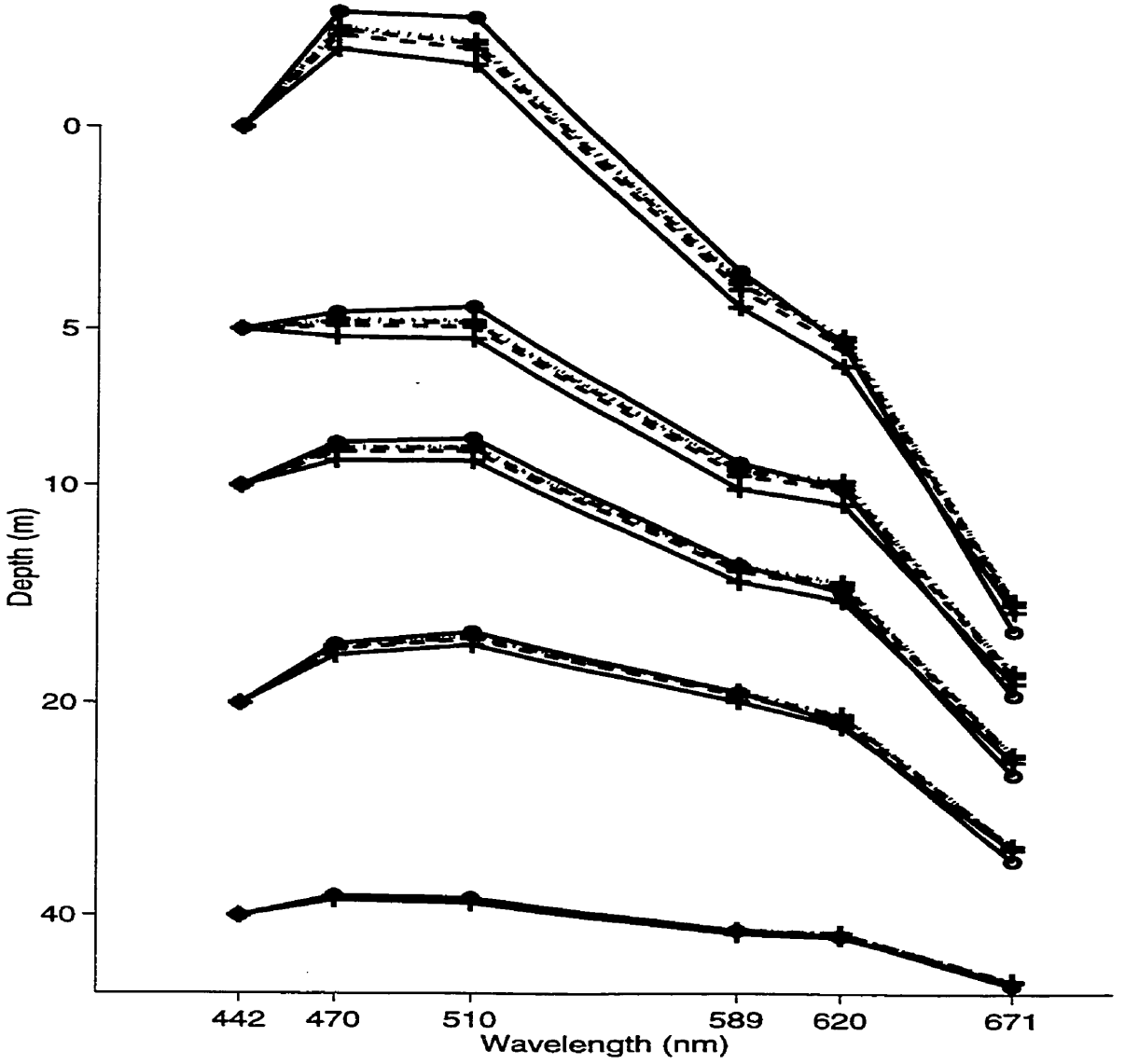

Figure 3.1: Backscatter normalized to the backscatter at 442nm corrected with η and total absorption (measurements of particulate and dissolved absorption as well as that due to water as estimated by Pope and Fry (1997)) with four values of $\tilde{b}_b$ for April 30, 1998 at the five depths for which absorption measurements were made. The normalized values are scaled such that the first data point has an actual value of one but is plotted with a y-value equal to the sample depth. —o— default correction (Equations 3.2, 3.3 and 3.4); —+— $\tilde{b}_{bp}$=0.01; - - + - - $\tilde{b}_{bp}$=0.02; - · + - · $\tilde{b}_{bp}$=0.03; · · + · · $\tilde{b}_{bp}$=0.04 (Equations 3.2, 3.3 and 3.4).

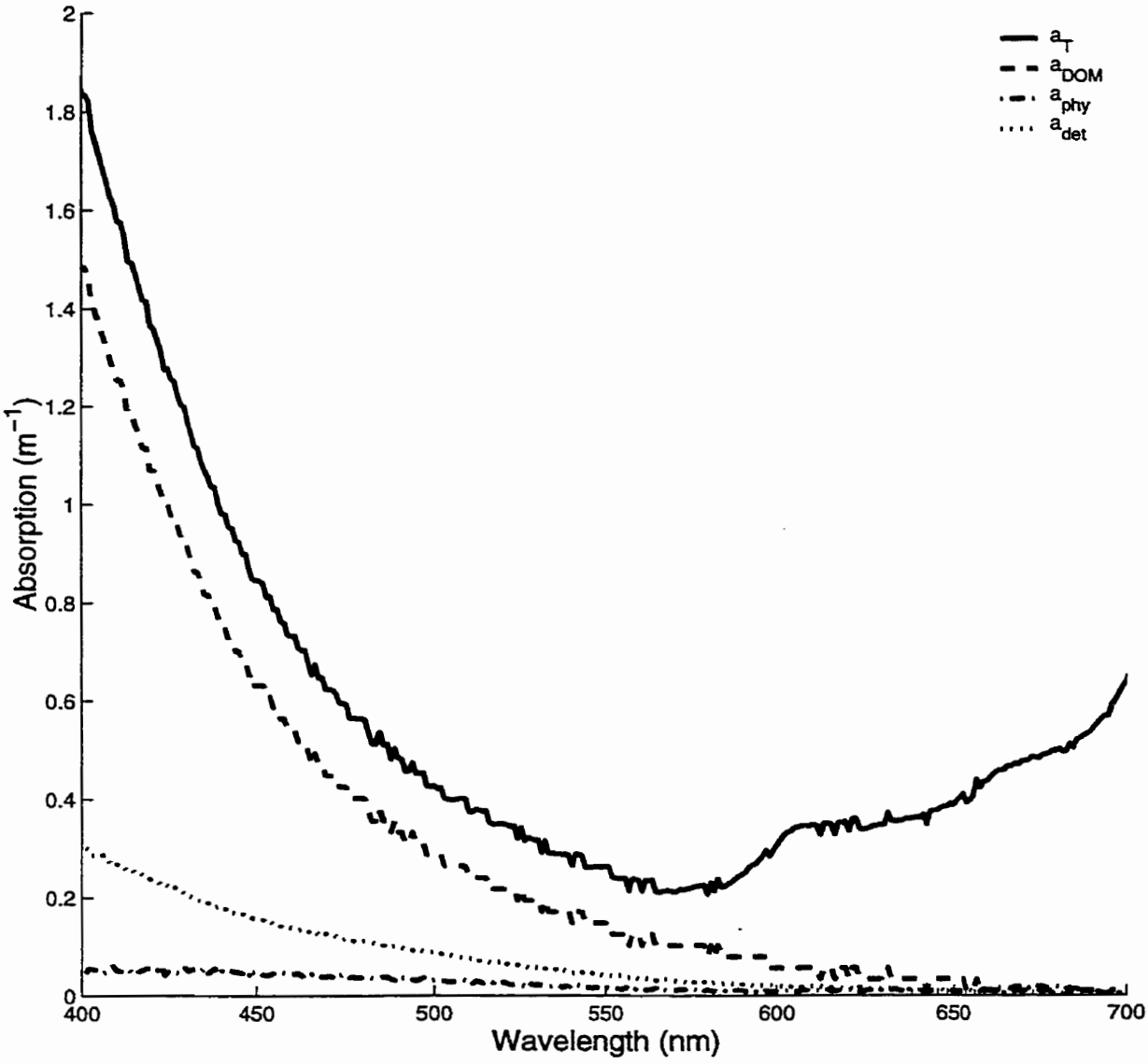

Figure 3.2: Surface water absorption from April 16, 1998. Subscripts are T for total, DOM for dissolved matter, *phy* for pigmented absorption and *det* for detrital or extracted absorption.

Chapter 4

Estimation of Backscatter from Particles Greater than 100μm

4.1 Introduction

The fraction of light scattered into the backward direction by particles suspended in natural waters is an important quantity for many problems in oceanography and limnology. In particular, it is integral for remote sensing and the interpretation of diffuse reflectance which has been shown to be a function of the backscattering coefficient (Morel, 1991; Ulloa *et al.*, 1994). Numerous theoretical studies have been performed to determine the influence of different classes of particles on the backscattering coefficient (for example Brown and Gordon, 1973; Kullenberg, 1974; Bricaud and Morel, 1986; Stramski and Kiefer, 1991; Ahn *et al.*, 1992; Ulloa *et al.*, 1994; Zhang *et al.*, 1998). Most studies have focused on particles less than 100μm. This focus is justified since small particles are more efficient backscatterers and by the assumption that the suspended particle size distribution follows a Junge–type power law relationship of the form

$$n_*(d) = C\left(\frac{d}{d_0}\right)^{-\xi} \tag{4.1}$$

where n_* is the log number concentration of particles in the size increment d to $d+\ln d$, C is the concentration of reference particles of diameter d_0 and ξ is an exponent typically assumed to vary between 3 and 5. Using such size distributions, the value of the particle backscattering coefficient has been found to be controlled by particles less than 100μm and particularly those less than 10μm (Morel, 1991; Stramski and Kiefer, 1991; Conner and Visser, 1992; Ulloa *et al.*, 1994; Mobley, 1994).

In situ measurements of suspended particle size distributions have demonstrated the importance of large amorphous particles, often much larger than 100μm, to the packaging of particulate material (Smetacek, 1985; Kranck and Milligan, 1988; Alldredge and Gotschalk, 1989; Eisma *et al.*, 1990; Riebesell, 1991b, 1991a; Kranck and Milligan, 1992; Kepkay *et al.*, 1993; Kiorbe *et al.*, 1994; Li and Logan, 1995; Milligan, 1996). Few measurements of the *in situ* size distributions in the less than 100μm range have been made. However, Eisma et al.(1990) found a continuous particle size distribution from 3.6-644μm suggesting that distributions less than 100μm may follow those measured for particles greater than 100μm. This provides evidence for a size distribution in which particles larger than 100μm may be more important than is generally considered by optical studies that use a Junge slope of 3–5 since *in situ* floc studies have found suspensions with slopes less than 3 (for example Kranck and Milligan, 1992; Li and Logan, 1995).

The effect of aggregate formation on the optically important particles (less than 100μm) is unknown. Aggregation may scavenge only a small portion of the optically important particles into flocs, resulting in an insignificant change to backscatter. In this case, backscatter would always be dominated by particles less than 100μm. If a wholesale scavenging of optically important particles by aggregation occurs, then observed backscatter would be reduced and the backscatter from large particles would dominate the observed signal. It is also possible that the scavenging of small particles by aggregates would produce some intermediate effect on the number concentration of particles less than 100μm. As a result, aggregation would result in a significant reduction in optically important particles but, no size would dominate measured

backscatter.

The goal of this chapter is to assess the effect of aggregation of a phytoplankton bloom on the magnitude of backscatter and on the relative contribution of large particles to the backscatter coefficient. To do this, Mie theory is used to calculate expected particulate backscatter from measured *in situ* areal particle size distributions of particles larger than 100μm. These estimates are then compared to backscatter measured by the Hydroscat–6, a multiwavelength backscatter sensor. Comparisons are made for ten sampling days over the course of the spring phytoplankton bloom in Bedford Basin, Nova Scotia from February 26 to April 30, 1998.

4.2 Methods

Digital silhouette images of the particles in suspension were taken at approximately 1.5m increments and analyzed using Image Pro-Plus (Media Cybernetics) image analysis software. The area for each visible particle was calculated by summing the total number of pixels greater than a threshold pixel grey–level value. Area was then converted to equivalent circular diameter as

$$D = \sqrt{\frac{4 \cdot A}{\pi}} \tag{4.2}$$

where A is the projected area of the particle. Each particle from an image was binned into size classes separated by one third ϕ units where

$$D(mm) = 2^{-\phi} \tag{4.3}$$

The smallest particle size bin had a median ϕ of 3.3 ($\sim$100μm). Total area in each size class was calculated as the sum of the particle areas measured for each size class bin (see also Eisma *et al.*, 1990). To calculate the total area per–unit–volume in each size class bin, the area in each bin is normalized to the total volume of the image (area of the image multiplied by the depth of field).

To estimate the approximate mean particle area in each image, the graphic mean of the areal probability plot was calculated as

$$M_A = \frac{A_{16} + A_{50} + A_{84}}{3} \tag{4.4}$$

where A_{16}, A_{50} and A_{84} are the 16th, 50th and 84th percentiles of the areal size distribution probability plots respectively (Friedman *et al.*, 1992).

The Hydroscat–6 was set to measure at a frequency of 2 Hz, and drop rate was $0.3\text{m}\cdot\text{s}^{-1}$ resulting in approximately one measure per 0.17m. The average of all measurements of backscatter within half a meter of image depth was calculated to give a corresponding one meter binned average of measured backscatter as a function of wavelength for each image. Backscatter measurements were corrected for pathlength attenuation according to the default correction (Chapter 3 this document, Maffione and Dana, 1997) and the backscatter due to water was subtracted using values from Smith and Baker (1981) resulting in a measurement of particulate, including detrital, backscatter at wavebands centered on 442, 470, 510, 589, 620 and 671nm.

Mie calculations were performed using Matlab code adapted from Bohren and Huffman (1983) by Emmanuel Boss in 1998. The code was verified with results from Stramski and Kiefer (1991) (see Figure 4.1) and proved to reproduce the published values. The solution from Mie is given as a dimensionless efficiency factor for a given diameter, refractive index and wavelength at all angles from 0–180°. The efficiency factor represents the portion of energy incident on the cross-sectional area of the particle that is scattered into any given direction (Stramski and Kiefer, 1991; Mobley, 1994). The code, as used, resolves into one degree increments. The efficiency for scattering angles 90-180° is then integrated to calculate the backscattering efficiency. A backscatter coefficient may then be estimated for a given areal distribution per–unit–volume as

$$\begin{aligned} b_{bp(calc)}(n,\lambda) &= \int_{d_{min}}^{d_{max}} Q_{bb}(n,\lambda,d)\cdot A_v(d)dD \\ &= \sum_{i=1}^{p} Q_{bb}(n,\lambda,d_i)\cdot A_v(d_i) \end{aligned} \tag{4.5}$$

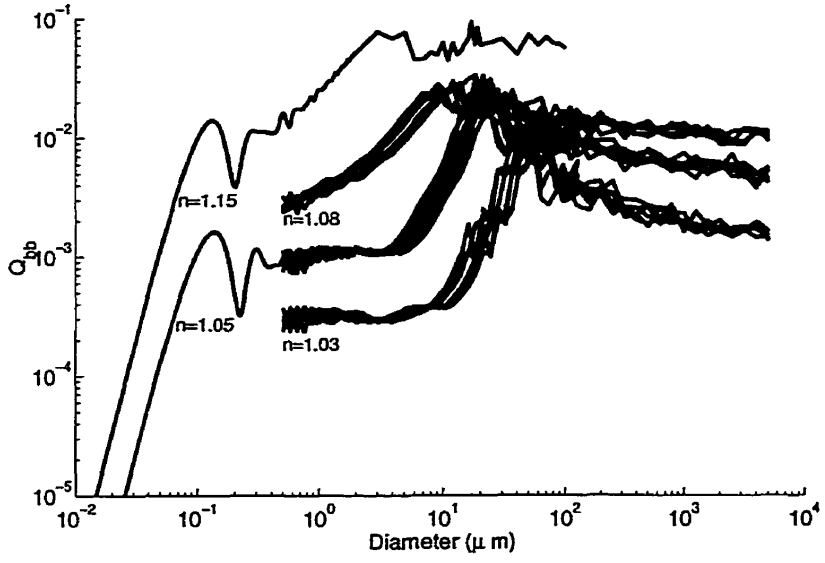

Figure 4.1: Plot of backscattering efficiency (Q_{bb}) from Stramski and Kiefer (1991) at indices of refraction n=1.05 and n=1.15 along with that calculated in this study (at n=1.03, 1.05 and 1.08). Lines from published data are calculated at 550nm and those from this study for 442, 470, 510, 589, 620 and 671nm.

Where i=1,$\cdots$,p are the size classes of measured particle areal size distribution per–unit–volume with median equivalent spherical diameter d_i, Q_{bb} is the backscattering efficiency factor with refractive index n and incident wavelength λ.

Mie runs were performed for the median particle size of bins found in the digital silhouette images (18 bins from $\sim$100μm to $\sim$5000μm equivalent circular diameter separated by one third phi units) and setting the index of refraction to 1.03, 1.05, 1.08 and 1.05-0.0005i for wavelengths 442, 470, 510, 589, 620 and 671nm. Indices of refraction were chosen to encompass the indices expected for a mixture of diatoms and inorganics found in Bedford Basin (Aurea Ciotti personal communication, 1999) and are within expected organic and inorganic refractive index values (see for example

Brown and Gordon, 1973; Morel, 1991; Stramski and Kiefer, 1991). Note that only one run of calculations was performed with a complex index of refraction value greater than zero in order to determine the effect of adding energy loss on the calculation of predicted backscatter from large particles. Wavelengths were chosen to match the median of the wavebands measured by the Hydroscat–6.

Assuming that the image particles are sufficiently homogeneous and that the particle image area can be converted to a representative equivalent circular diameter, calculated efficiency factors for a given index of refraction, wavelength and equivalent circular diameter were used in Equation 4.5 to calculate an estimated backscatter coefficient ($b_{bp(calc)}(\lambda)$) for particles $\geq 100\mu$m as obtained from the images. This estimated backscatter is directly comparable to the corresponding backscatter measurements made by the Hydroscat–6 ($b_{bp(obs)}(\lambda)$), although the calculated backscatter does not include an estimate of backscatter from particles $<100\mu$m.

Sackville River discharge into Bedford Basin was obtained from Fred Lindeijer at Environment Canada in Dartmouth, Nova Scotia. Data are presented for the week previous to sampling until the end of the study and are displayed as the daily discharge in m^3s^{-1}. The discharge data was used to qualitatively approximate the potential fraction of inorganic particulates making up the total suspended material.

Total suspended particulate matter ($mg{\cdot}L^{-1}$) and inorganic volume of particulates per unit volume of suspension for particles greater than 0.8μm were measured at DFO's Bedford Institute of Oceanography (BIO) for 5, 10, 20 and 40m throughout the bloom study. Suspended particulate mass was calculated as the weight of particulates trapped on a 0.8μm cellulose filter for the volume of sample filtered. Inorganic volumetric grain size distributions were calculated from the ashed cellulose filter resuspended in electrolyte and measured using a Coulter Multisizer IIE according to Milligan and Kranck (1991).

Chlorophyll concentrations were estimated from a fluorometer calibrated against extracted chlorophyll *a* samples after the study period was complete. Concentrations are reported in $\mu g\ L^{-1}$ (or equivalent $mg\ m^{-3}$) but should not be taken as absolute

values, rather as relative approximations. More information on the method used to obtain the chlorophyll *a* estimates can be found in Li *et al.* (1998).

4.3 Results

Comparisons between the observed and calculated backscatter for all indices of refraction and all wavelengths resulted in two distinctly different relationships. Figures 4.2, 4.3 and 4.4 show the relationship for all wavelengths at indices of refraction 1.03, 1.05 and 1.08 respectively. Sample day accounts for the two relationships. Sample days from February 26 to March 19 (four in total) result in the relationship that has the higher slope while the last six sample days, from March 26 to April 30th, result in the lower slope value. The points that lie between the two relationships are from the surface waters of March 12 and 19th where diatom chains and the first aggregates were visible in the images. A change in the suspended particles between March 19 and March 26 resulted in a change in the relationship between backscatter calculated from *in situ* areal size distributions larger than 100μm and that observed by the Hydroscat–6. In the first part of the study, particles greater than 100μm tend to under–estimate observed backscatter whereas in the second part of the study, they tend to over–estimate observed backscatter.

For both February 26–March 19 and March 26–April 30, a simple linear regression was performed according to

$$b_{bp(obs)} = slope \cdot b_{bp(calc)} + intercept \tag{4.6}$$

Slopes and intercepts were calculated for each index of refraction and wavelength. Although the addition of a complex value to the index of refraction also resulted in two relationships between observed and calculated backscatter, the absolute values of the calculated backscatter were questionable and the results will not be presented. Table 4.1 gives the range of slopes, intercepts and R^2 value for all wavelengths within each set of days.

Table 4.1: Slopes, intercepts and R^2 values for $b_{bp(obs)}(\lambda)$ versus $b_{bp(calc)}(\lambda)$. Observed backscatter coefficient is presented in the second column as the range for all wavelengths for a given set of days. Outliers from the surface waters of February 26, March 12 and March 19 were excluded from parameter calculations for the first set of days. Sample size is 344 for the first four weeks and 718 for the last six. Model estimated parameters were all significantly greater than zero with p-values less than 0.001 and are presented as the range for all wavelengths for each set of days. A slope greater than one, such as that seen for n=1.03 and 1.05 for the first four weeks, shows that $b_{bp(calc)}(\lambda)$ under–estimates $b_{bp(obs)}(\lambda)$. A slope less than one, such as that seen for n=1.05 and 1.08 for the last six weeks of the study, indicates that the value calculated from the images is over–predicting the observed value.

Days	$b_{bp(obs)}$ ($x10^{-3}$)	n	Slope	95% CI	Intercept ($x10^{-3}$)	95% CI ($x10^{-3}$)	R^2
26/02/98-		1.03	5.14-6.5	4.76-6.97	4.44-6.41	4.08-7.07	.61-.77
19/03/98	4.38-30.9	1.05	1.92-2.65	1.8-2.84	4.44-6.48	4.06-7.14	.61-.76
		1.08	1.26-1.65	1.18-1.76	4.48-6.55	4.08-7.14	.60-.75
26/03/98-		1.03	.655-.925	.614-.975	3.75-4.92	3.65-5.04	.55-.65
30/04/98	2.97-14.8	1.05	.225-.358	.211-.378	3.75-5.02	3.66-5.14	.54-.64
		1.08	.136-.21	.128-.221	3.8-5.07	3.71-5.19	.53-.64

The linear relationship between observed and calculated backscatter accounts for at least 53% and as much as 77% of the variability in the observed backscatter. Since the intercept is always non-zero, there is a portion of backscatter that is not accounted for by that calculated from the images. This is not wholly unexpected since the estimated backscatter is calculated for only particles greater than 100μm.

Also presented in Table 4.1 are the 95% confidence limits surrounding the slopes and intercepts for the two relationships between observed and predicted backscatter. None of the confidence intervals for the slopes overlap between sets of days or between indices of refraction. Therefore, all slopes are significantly different. However, all intercept confidence intervals overlap, and therefore intercepts for the relationship for either set of days and any index of refraction are statistically similar.

4.4 Discussion

Total backscatter is made up of that resulting from water, particles and operationally dissolved substances. It can be expressed as

$$b_{bT} = b_{bw} + b_{bp} + b_{bdet} \tag{4.7}$$

Where the subscripts w, p and det refer to water, particles and detrital material which also includes backscatter from matter that is operationally defined as dissolved ($<0.45\mu$m), respectively. The backscatter from particles of size diameter d_i ($b_{bp}(d_i)$) can be estimated as

$$b_{bp}(d_i) = Q_{b_b}(n_i, \lambda, d_i) \cdot \frac{\pi d_i^2}{4} \cdot N_i \tag{4.8}$$

where $Q_{b_b}(n, \lambda, d_i)$ is the backscattering efficiency of a particle with index of refraction n_i, at incident wavelength λ and diameter d_i. N_i is the number concentration of particles with diameter d_i.

An heuristic model can be used to examine the causes of the two relationships between observed backscatter and that estimated from particles visible in the digital images by partitioning particles into one class containing all those visible in the images and another that falls below the resolution of the camera. For the purpose of this discussion, large particles are those greater than 100μm and small particles are those less than 100μm and therefore not resolvable by the digital camera. The large class of particles is characterized by a mean particle diameter d_L, mean index of refraction n_L, mean backscattering efficiency $Q_{b_b}(n_L, \lambda, d_L)$ and number concentration N_L. Similarly, the small class of particles is characterized by diameter d_S, index of refraction n_S, backscattering efficiency $Q_{b_b}(n_S, \lambda, d_S)$ and number concentration N_S. In order to simplify the model, it is assumed that the concentrations of large and small particles are related, such that

$$N_S = N_{S_0} + m \cdot N_L \tag{4.9}$$

Where N_{S_0} is a background concentration of small particles not related to the concentration of large particles and m is the slope of the linear relationship between

the concentration of small and large particles. The relationship reflects that the large particles visible in the digital images are predominantly composed of smaller particles.

Using Equations 4.8 and 4.9, backscatter due to particles can be written as

$$b_{bp} = Q_{b_b}(n_L, \lambda, d_L) \cdot \frac{\pi d_L^2}{4} \cdot N_L + Q_{b_b}(n_S, \lambda, d_S) \cdot \frac{\pi d_S^2}{4} \cdot (N_{S_0} + m \cdot N_L) \tag{4.10}$$

Collecting all terms with N_L yields

$$\begin{aligned} b_{bp} &= Q_{b_b}(n_S, \lambda, d_S) \cdot \frac{\pi d_S^2}{4} \cdot N_{S_0} \\ &\quad + \left(1 + \frac{m \cdot Q_{b_b}(n_S, \lambda, d_S) \cdot d_S^2}{Q_{b_b}(n_L, \lambda, d_L) \cdot d_L^2}\right) \cdot Q_{b_b}(n_L, \lambda, d_L) \cdot \frac{\pi d_L^2}{4} \cdot N_L \end{aligned} \tag{4.11}$$

Let

$$b_{bp_0} = Q_{b_b}(n_S, \lambda, d_S) \cdot \frac{\pi d_S^2}{4} \cdot N_{S_0} \tag{4.12}$$

$$\alpha = \frac{m \cdot Q_{b_b}(n_S, \lambda, d_S) \cdot d_S^2}{Q_{b_b}(n_L, \lambda, d_L) \cdot d_L^2} \tag{4.13}$$

$$b_{bp_L} = Q_{b_b}(n_L, \lambda, d_L) \cdot \frac{\pi d_L^2}{4} \cdot N_L \tag{4.14}$$

and Equation 4.11 simplifies to

$$b_{bp} = b_{bp_0} + (1 + \alpha) \cdot b_{bp_L} \tag{4.15}$$

In Equation 4.15, b_{bp_0} is the backscatter due to the background particles not correlated to the concentration of large particles, b_{b_L} is the backscatter from large particles and α is a coefficient that describes the enhancement of backscatter that arises from small particles that covary in concentration with large particles.

With Equations 4.7 and 4.15, backscatter due to suspended particulate material, including that operationally defined as dissolved, can be written as

$$b_{bT} - b_{bw} = b_{bp_0} + (1 + \alpha) \cdot b_{bp_L} + b_{bdet} \tag{4.16}$$

Assuming b_{bdet} is uncorrelated with large particle concentrations, b_{bp_0} and b_{bdet} can be combined to form a single backscatter from small, background particles that are uncorrelated with the large image particles. This yields

$$b_{bT} - b_{bw} = b_{b_0} + (1 + \alpha) \cdot b_{bp_L} \tag{4.17}$$

The term b_{bp_L} in Equation 4.17 is the actual backscatter from large particles. However, the true refractive index of the large particles is unknown, they are likely irregularly shaped and not homogeneous which is not considered in Mie calculations. The value of b_{bp_L} that is estimated from the large particle size distributions found in the images may only be proportional to the actual value. Therefore, let

$$\Omega = \frac{b_{bp_L}}{b_{bp(calc)}} \tag{4.18}$$

where $b_{bp(calc)}$ is theoretical backscatter from large particles visible by the camera and Equation 4.17 becomes

$$b_{bT} - b_{bw} = b_{b_0} + (1 + \alpha) \cdot \Omega \cdot b_{bp(calc)} \tag{4.19}$$

Let the left hand side of Equation 4.19 equal the backscatter measured by Hydroscat minus backscatter from water and denote as

$$b_{bp(obs)} = b_{b_0} + (1 + \alpha) \cdot \Omega \cdot b_{b_C} \tag{4.20}$$

Equation 4.20 shows the backscatter measured by the Hydroscat minus that due to water as linearly related to the backscatter estimated from the digital images of particles greater than 100μm. The intercept of this relationship defines the amount of observed backscatter that persists regardless of the relationship between observed and calculated backscatter. The value of the slope depends on the values of α and Ω. In turn, this leads to a dependence on the slope of the relationship between the concentration of large and small particles, the refractive index of large and small particles and the ratio of actual backscatter from particles to backscatter estimated from large particles visible in the digital images.

The intercept of the linear relationship between observed and predicted backscatter did not significantly change between indices of refraction nor between the sets of days (see Table 4.1). The magnitude of the intercept indicates that the background backscatter (b_{b_0})–which has been parameterized as both detrital backscatter and backscatter due to particles uncorrelated with the large particles visible in the digital images–accounts for 13-100% of the total measured backscatter from February 26 to March 19 and 25-100% of the measured backscatter from March 26 to April 30 (see Table 4.1 for minimum and maximum of observed backscatter and 95% confidence interval for the intercept value). The constancy in the absolute value of the intercept value suggests that the variability over the study period of the detrital and small particles uncorrelated to those visible in the images is low.

The slope of the linear relationship between observed and predicted backscatter was different between the two sets of days regardless of index of refraction. The slope in the second part of the study (March 26 to April 30) was significantly lower than that seen in the first part (February 26 to March 19). This reduction in slope must have resulted from a reduction in the model parameters α or Ω.

A reduction in α could arise from a change in value in a few parameters (see Equation 4.13). A reduction in the slope (m) of the linear relationship between the number concentration of small particles and the number concentration of large particles would result in a reduction of α. Such a reduction could arise from an increase in the efficiency of small particle scavenging by flocs. A reduction in α could also arise from a reduction in the ratio of the backscattering efficiency of small to large particles. Such a reduction could occur if the refractive index of small particles decreased while the large particle index of refraction increased independently. However, since the large particle flocs are composed of the smaller particles and become increasing porous as they accumulate (Li and Logan, 1995), it is unlikely that such a change would occur. Finally, α could be reduced if the ratio of the small to large particle diameter squared was reduced. This would require a reduction in the small particle

diameters independent of, and/or coincidental to, an increase in the large particle diameters. This would require plankton populations to decrease in individual diameters and/or a coincidental increase in floc size.

A reduction in Ω is either a result of decreased actual backscatter from large particles to that predicted from the digital image areal size distributions and/or an increase in the predicted backscatter to the actual (see Equation 4.18). The Mie solution of scattering of light by a homogeneous sphere is rigorous and exact for all wavelengths, indices of refraction and sizes (Mobley, 1994). However, predicting backscatter from measured areal particle size distributions involves making assumptions in order to use Mie theory.

The Mie calculations are based on homogenous spherical particles. This study involves agglomerations of particles, that are not homogenous. The composition of the aggregate likely changes with orientation making the actual refractive index a function of position (Brown and Gordon, 1973). However, a single refractive index must be assumed, its value one that can be expected to characterize the dominant particles. A reduction in Ω could arise from a compositional shift from higher index of refraction particles, such as inorganics, to those with lower indices of refraction, such as organics. A decrease in the actual backscatter from large particles would occur but the corresponding change in predicted backscatter would not occur unless an adjustment was made to the index of refraction used for prediction.

This study focuses on relatively large particles ($>100\mu$m) which tend to be more nonspherical than smaller particles and more complex in structure (Jonasz, 1987) and light scattering properties (Gibbs, 1978). Shape becomes particularly important when the effective area of a particle–the particle area that actually intersects light–is larger than its equivalent spherical area–area calculated from the volume of the particle such as is measured by a Coulter Counter–(Kullenberg, 1974). Nonspherical particles, when averaged over all orientations, have effective areas larger than those of spheres with equal volume (Jonasz, 1987; Carder and Costello, 1994). This supports the use of *in situ* areal size distributions from images versus those from a volume sensitive

Coulter Counter which may underestimate the actual projected area of a nonspherical particle (Jonasz, 1987). This is particularly true if the system is dominated by fragile aggregates that tend to at least partially disaggregate upon sampling. It is unclear exactly what effect the irregular shape of the large particles will have on the ratio of actual to predicted backscatter. The use of *in situ* images should provide a good estimate of effective area and the largest errors are likely to occur in estimating the equivalent circular diameter from the irregularly–shaped projected area in order to use Mie theory. A reduction in Ω would arise from an effective area that is too large, such as if the image analysis program systematically over-estimated area, or over–estimation of the equivalent circular diameter, such as if particles were consistently measured at their largest cross-sectional area or flocs overlapped in the digital images (Milligan, 1996).

Slopes less than one in the relationship between observed backscatter and that predicted from *in situ* particle areal size distributions greater than 100μm indicate that the value of Ω is less than one (since $(1 + \alpha)$ is always greater than one). This is true for all slopes for the period March 26 to April 30 at all indices of refraction. This indicates that the estimates of backscatter are inaccurate and larger than the actual values of backscatter from large particles.

The shift in the slope of the relationship between observed and calculated backscatter that occurred between March 19 and March 26 must have resulted from some change in the composition or size distribution of the suspended particles. Using ancillary data collected during the spring bloom study provides clues to the potential changes. Figure 4.5 shows the ancillary data versus sample day as well as the magnitude of observed and predicted backscatter at 442nm.

Changes in composition would arise if changes in the relative amounts of inorganic to organic particulates changed. The Sackville River discharge is given in the second panel of Figure 4.5. If the discharge were higher in the week previous to a sample day, it would be expected that inorganics and/or coloured dissolved matter would increase. Discharge is highest for the period previous to March 19. Total disaggregated

inorganic parts per million ($mm^3\ dm^{-3}$), which represents the sum of inorganic particulates greater than $\sim 1\mu m$ per–unit–volume from the Multisizer, is a direct measure of changes to the amount of inorganic material in suspension and is given in the third panel of Figure 4.5. It is highest on March 12 and 19th, and declines after the 19th. Chlorophyll is an indirect measure of the amount of organic material present in the system. In general, chlorophyll is low before March 19 although the surface waters of March 12 and 19th are fairly high (see the fourth panel of Figure 4.5). Overall chlorophyll values peak by April 16 and then decline to the lowest levels on April 30.

From this evidence, it is possible that a shift from a more inorganic system on sampling days February 26 to March 19 to one with more organics after March 26 occurred. This is also supported by calculations of backscatter from the images from February 26 to March 19 having a slope closer to one for a higher index of refraction, n=1.08, and those from March 26 to April 30 having a slope closer to one for a lower index of refraction, n=1.03 (see Table 4.1).

Changes to the *in situ* size distribution could also have caused the observed change in relationship between the measured and calculated backscatter coefficient. The sum of area per unit volume from the images (panel five of Figure 4.5) shows that the total area of visible particles increases throughout the study but specifically from March 26 to April 16, after which it decreases again. When this sum increases, particles greater than $100\mu m$ have increased. Further, the increase in graphic mean (panel six Figure 4.5) beginning March 26 and lasting until April 23 points to an increase in particle size.

This shift in particle size provides a simple model for what may have caused the shift between March 19 and 26th in the relationship between the observed and calculated backscatter. Larger particles began to appear in the surface waters of March 12 and 19th as diatoms began to bloom and form chains. The first flocs appear in the surface waters of March 19. These flocs begin to incorporate all other particles less than what is visible by the camera. By March 26, the first flocs have swept the water column of smaller, likely more inorganic in nature and therefore more

optically efficient particles, which were present after winter. This results in an overall decrease in the magnitude of backscatter (panel seven Figure 4.5) and the change in ability of large particles to predict backscatter. Further evidence for this model lies in the persistence of the relationship even after the concentration of flocs has decreased.

A similar sequence of events was evident in the 1986 spring bloom. The diatom population was seen to progress from a state of chains to clusters of chains. Finally, solid looking aggregates in which individual chains were difficult to distinguish appeared (Kranck and Milligan, 1988).

A simple schematic of this model is found in Figure 4.6. In the first four weeks of sampling (February 26–March 19) backscatter predicted from the *in situ* size distribution greater than 100μm typically under–predicts the observed backscatter. This system is potentially dominated by smaller particles that covary with those seen in the images. Beginning in the surface waters of March 12 and 19th where the more steeply sloped relationship between observed and calculated backscatter begins to shift towards the less steep, the smaller particles begin to be incorporated into larger aggregates. By March 26, the relationship between observed and predicted backscatter has shifted to a much less steep relationship wherein backscatter predicted from particles greater than 100μm tends to over–predict observed backscatter. This suggests that the aggregates have effectively cleared the system of smaller particles, an idea which is supported by the relationship holding after the large aggregates have disappeared from the system by April 30. Some of the change in relationship may also be attributed to a change in composition of the suspended particles from inorganic to organic. Evidence for the change in composition comes from the decrease in Sackville River discharge and the increase in chlorophyll concentration. The clearing by aggregates potentially fostered this compositional shift.

4.5 Conclusions

The calculation of backscattering coefficient from the *in situ* particle size distribution greater than 100μm as seen in digital silhouette images over a phytoplankton bloom shows two distinctly different relationships to the observed backscatter. The two relationships seem to be a result of some shift in the suspended particles between March 19 and 26th since time–period explains the two relationships. A simple model of the change in relationship suggests that smaller, potentially more inorganic, particles dominate the first four weeks of the study and result in a steeper relationship between observed and calculated backscatter. When aggregates begin to form in the surface waters of March 12 and 19th, the relationship begins to shift towards the less steep and by March 26, the shift is complete. At this time, the model suggests that aggregates have repackaged the smaller particles into larger aggregates and potentially cleaned the water column of smaller more efficient backscatterers.

It is interesting that the intercepts for the two sets of days are statistically equal. This suggests that there may be a background backscatter that is uncorrelated with the particles visible in the images that remains virtually constant throughout the study.

The relatively high R^2 values for the relationship between observed and predicted backscatter is an interesting result (see Table 4.1). This shows that backscatter from particles greater than 100μm may be more important than previous optical studies have assumed.

Previous theoretical studies of the backscattering coefficient from different populations of particles have placed less importance on particles greater than 100μm (for example Stramski and Kiefer, 1991; Ulloa *et al.*, 1994). This is mainly because the size distributions used typically overemphasize the importance of small sizes. The distributions are chosen to represent results from Coulter Counter studies that may not represent the actual *in situ* particle distributions due to breakup of fragile aggregates in the sample. The present study shows that the *in situ* size distribution of particles greater than 100μm can predict a large portion of the backscattering coefficient, even

over–estimate its value. This has implications in remote sensing where a flocculation event could rapidly change the optical signal received by the sensor that may be misinterpreted as a change in particle concentration or composition. Flocculation in the present study was found to decrease the overall backscatter after aggregate formation and clean-out of the water column of smaller particles(see Figure 4.5, panels six and seven).

The potential importance of particles greater than 100μm to the optical properties of natural waters has been under–predicted. The relationship between observed backscatter and that predicted from particles greater than 100μm indicates that further study into the effects of the formation of large aggregates and their subsequent effects on the smaller particles is warranted.

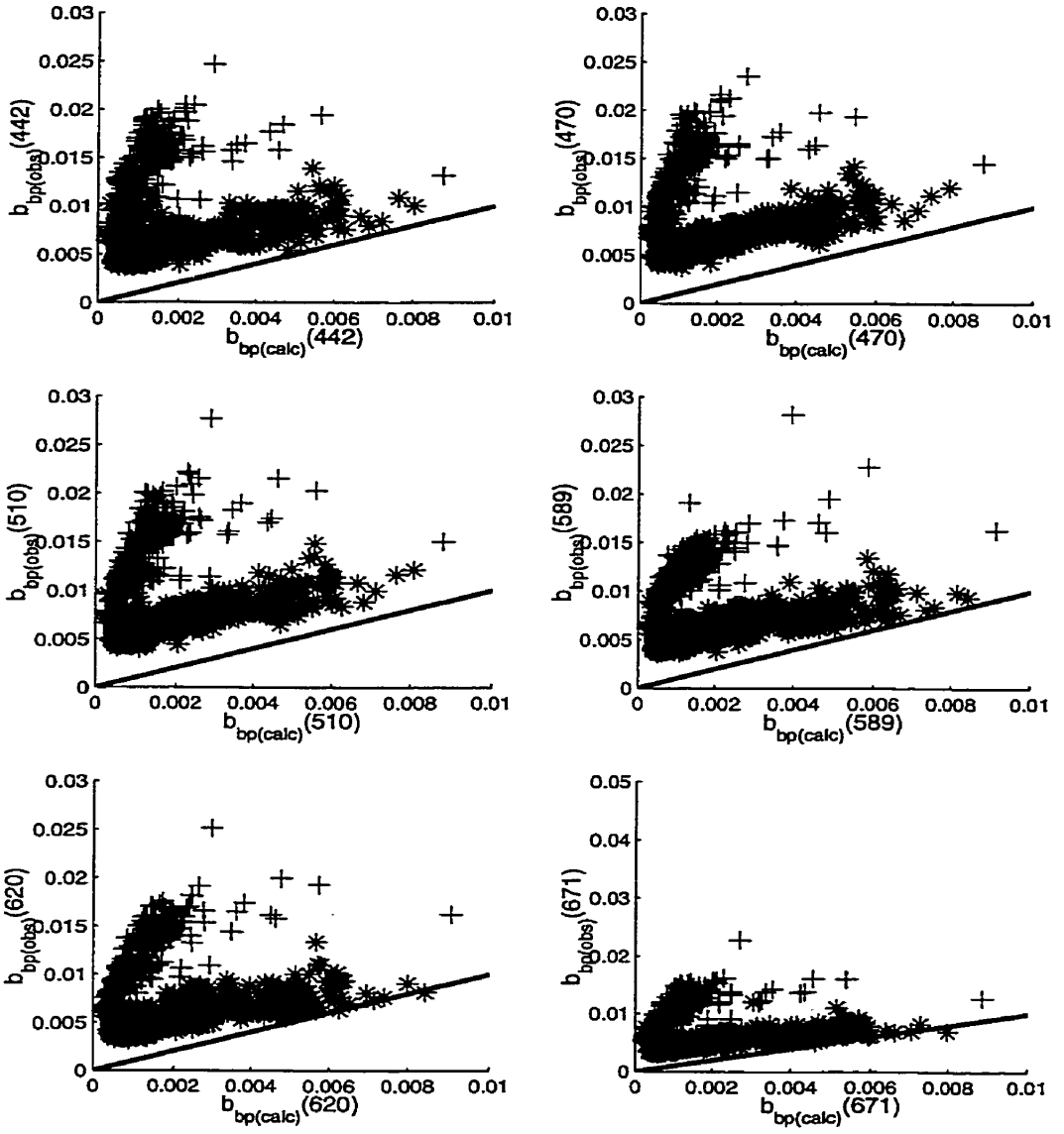

Figure 4.2: Observed versus predicted backscatter coefficient for the six Hydroscat wavelengths at n=1.03. The solid line is a one to one relationship between observed and predicted backscatter. Days February 26 to March 19 of the study are delimited with + while days March 26 to April 30 are delimited with $*$.

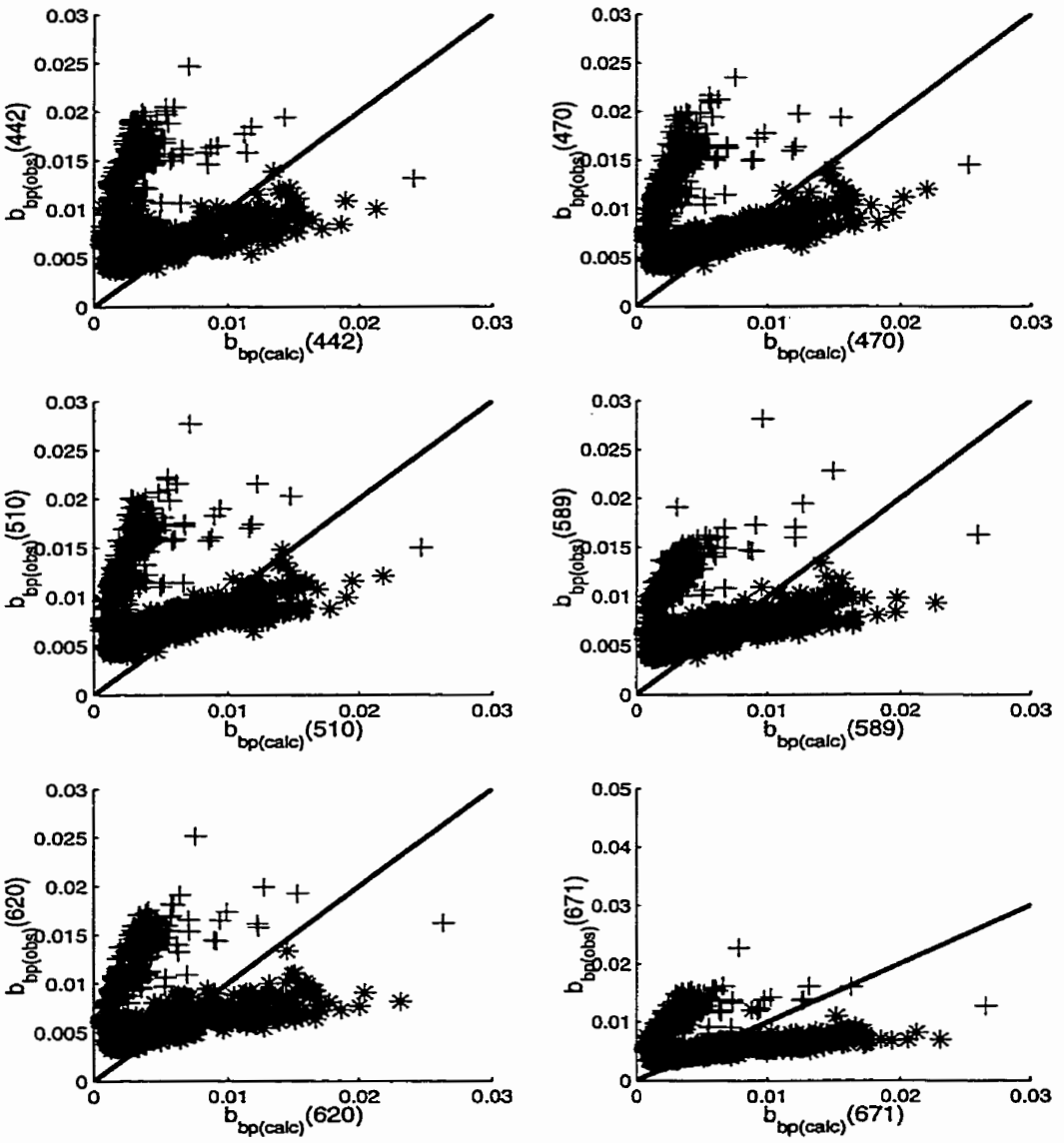

Figure 4.3: Observed versus predicted backscatter coefficient for the six Hydroscat wavelengths at n=1.05. The solid line is a one to one relationship between observed and predicted backscatter. Days February 26 to March 19 of the study are delimited with + while days March 26 to April 30 are delimited with $*$.

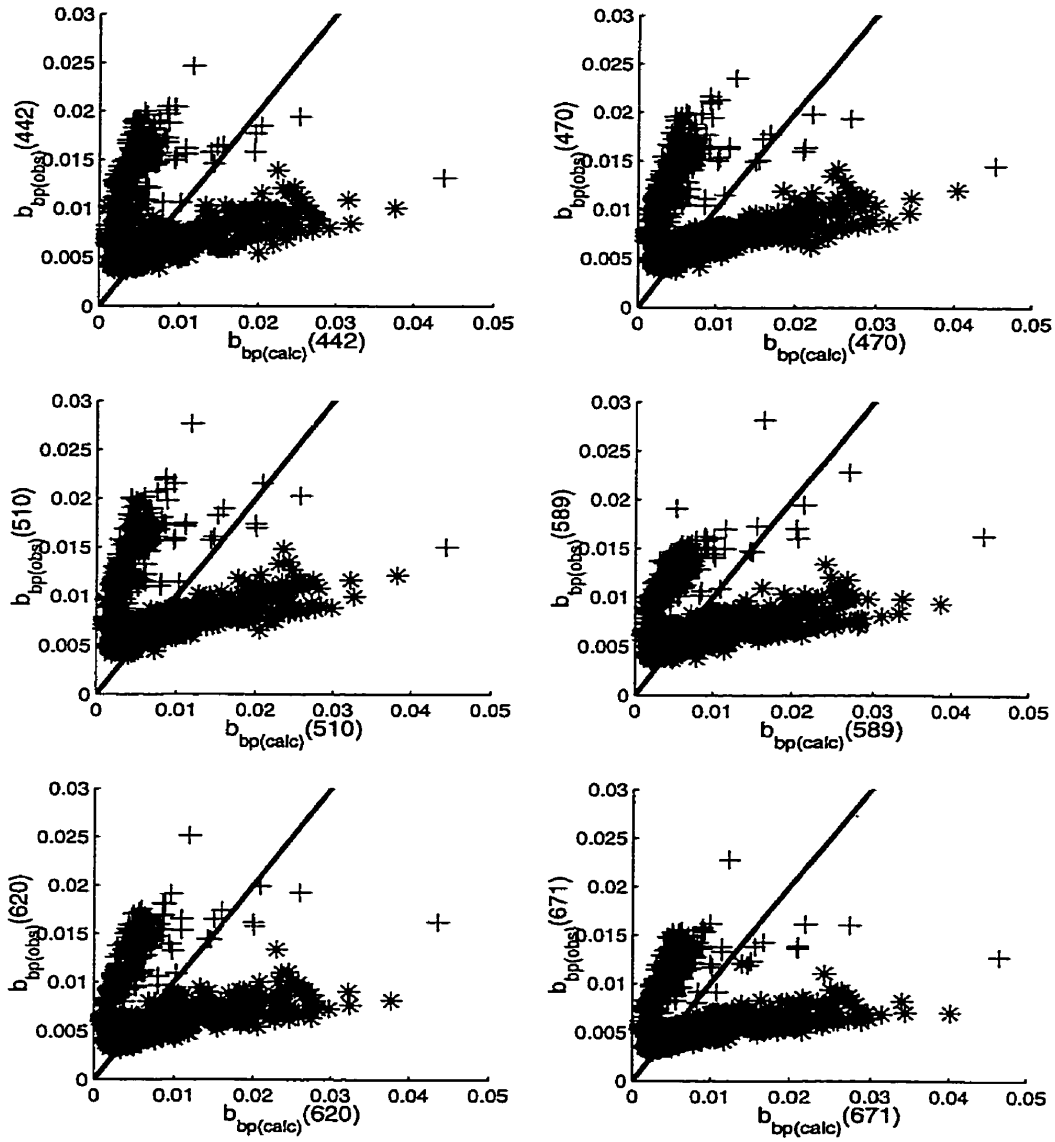

Figure 4.4: Observed versus predicted backscatter coefficient for the six Hydroscat wavelengths at n=1.08. The solid line is a one to one relationship between observed and predicted backscatter. Days February 26 to March 19 of the study are delimited with + while days March 26 to April 30 are delimited with $*$.

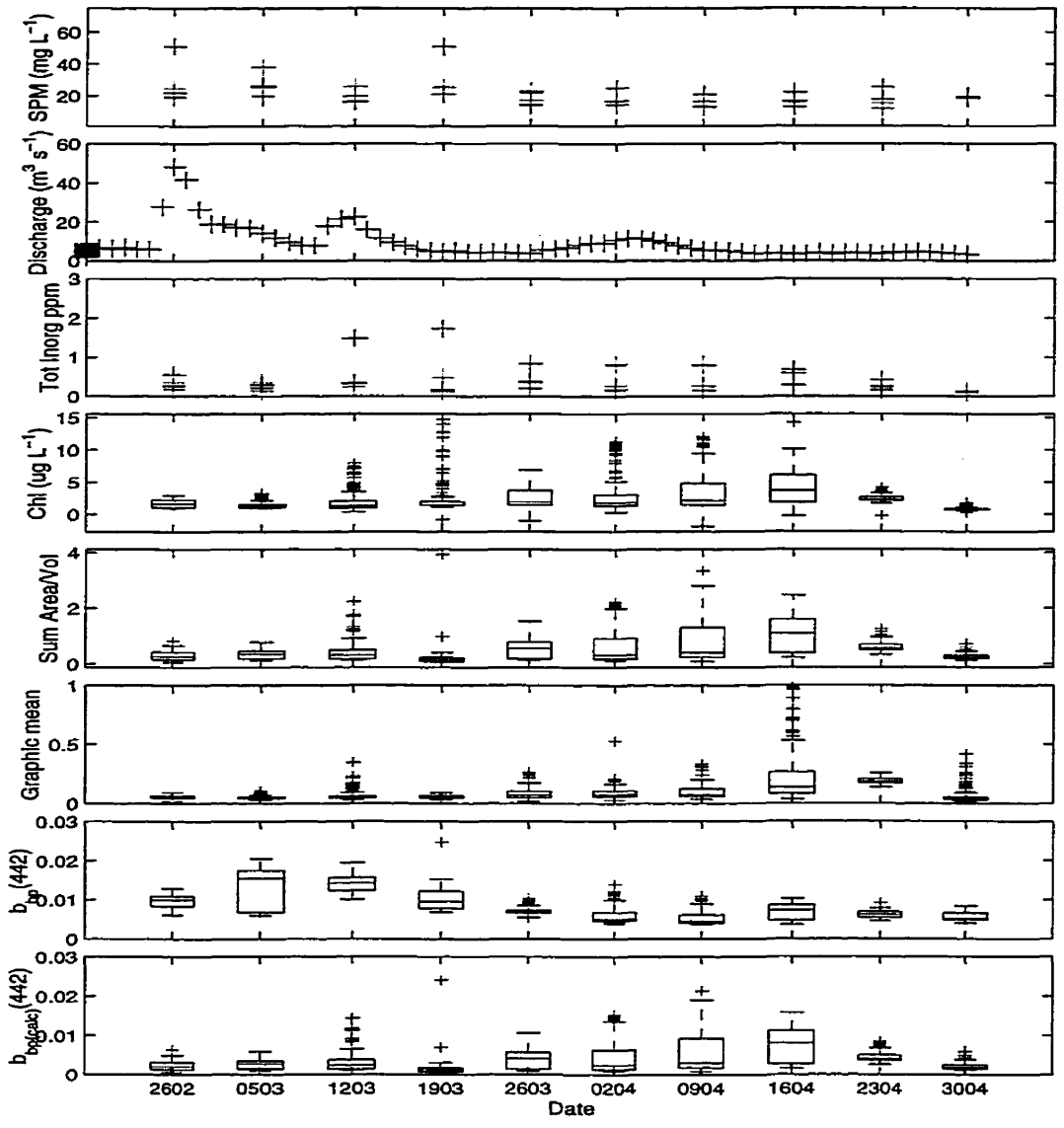

Figure 4.5: Ancillary data for the Spring Bloom 1998 experiment. Some data is displayed as box plots which show a box that encompasses the 25th to 75th percentiles of the data and lines extending to 1.5 times the respective percentile. Outliers for the box plots are the individual markers. The first panel represents the total suspended particulate matter (mg L^{-1}) captured on a 0.8μm filter. The second panel is the Sackville river discharge in m^3 s^{-1}. The third panel is total inorganic concentration (mm^3 dm^{-3}) captured on a 0.8μm filter. The fourth panel shows estimated chlorophyll *a* concentration (μg L^{-1}) from a profiled fluorometer. The fifth panel is the sum of image particle projected area for all median size bins normalized to the total image volume. The sixth panel shows the graphic mean of the particle area frequency distribution (see Equation 4.4). The seventh panel is observed backscatter at 442nm. The final panel is backscatter calculated using Mie theory at 442nm.

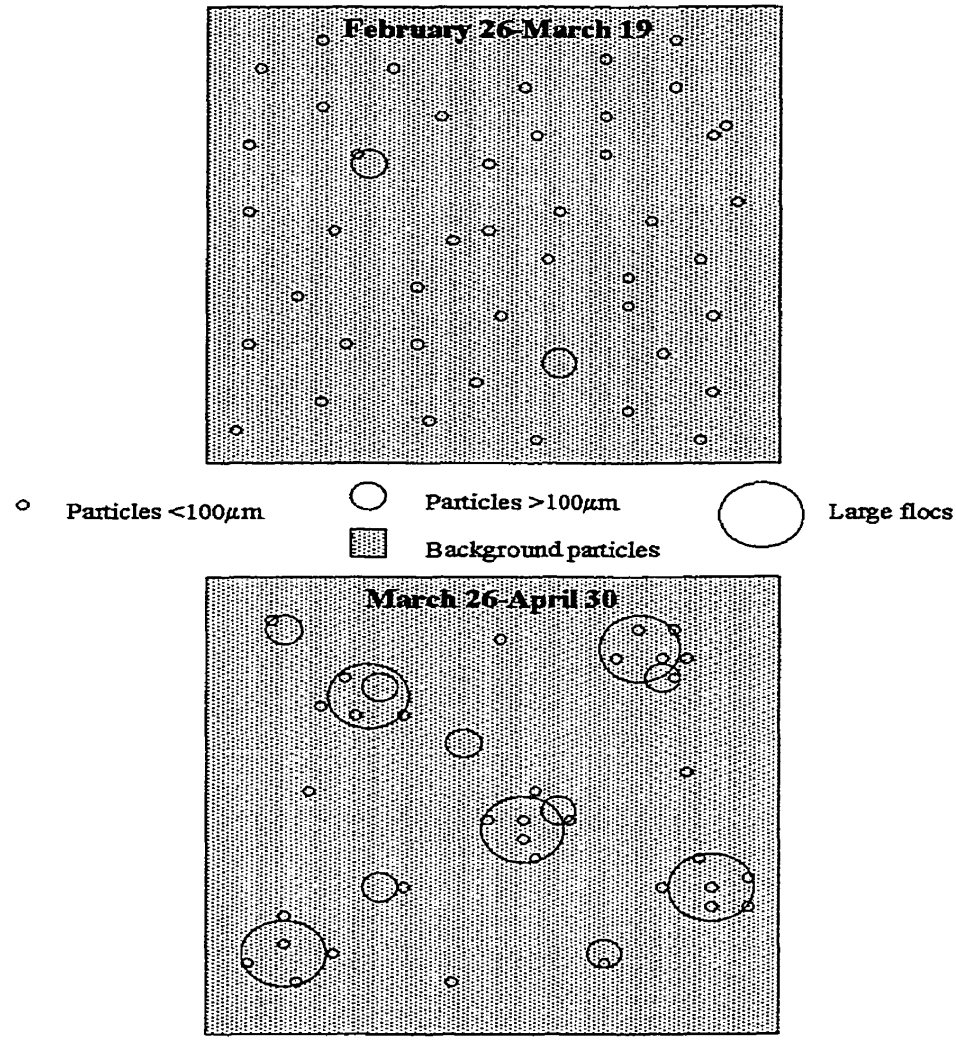

Figure 4.6: Model of the particle sizes present before and after the shift in the relationship between observed and calculated backscatter. The stippled particles represent those uncorrelated with particles visible in the images. The smallest circles represent particles that are not visible in the images but are correlated with those that are and contribute to the correlation between observed and calculated backscatter.

Chapter 5

Aggregation of Particles and the Wavelength Dependence of the Backscatter Coefficient

5.1 Introduction

The measurement of the spectral shape of backscatter is integral to the study of ocean colour since backscatter and absorption govern reflectance (Morel, 1991). The amount and colour of backscatter from a given parcel of water depends on the concentration, shape, refractive index and size of the ambient particles. Ulloa *et al.* (1994) suggest that the wavelength dependence of the particle backscatter coefficient b_{bp} follows

$$b_{bp}(\lambda) \propto \lambda^{(3-\xi)} \tag{5.1}$$

where λ is the wavelength of the source light and ξ is the slope of the Junge power–law particle size distribution for which the log area density function (a_*(d)) follows

$$a_*(d) = C\frac{\pi d_0^2}{4}\left(\frac{d}{d_0}\right)^{(2-\xi)} \tag{5.2}$$

where d is the particle diameter, d_0 is the reference particle diameter (not necessarily equal to the minimum resolvable particle diameter), C is the number concentration

of d_0 particles and ξ varies with environment. Any changes in the shape of the suspended particle size distribution should be reflected in ξ and therefore in the wavelength dependence of the backscatter coefficient.

Light scatter from large particles is diffractive in nature and therefore results in largely forward scattering (Kirk, 1994). Smaller particles, especially those <10μm, dominate backward scatter (Morel, 1991; Conner and Visser, 1992; Ulloa *et al.*, 1994; Mobley, 1994) as light is refracted and reflected off the surface of the particle. Large "fluffy" aggregates however, can be efficient scatterers of light at all angles, including the backward direction (Kullenberg, 1974; Mobley, 1994).

Aggregation of suspended particulate matter will change the *in situ* particle size distribution. Flocculation of phytoplankton blooms has been observed to occur rapidly, resulting in amorphous, aggregated material (Smetacek, 1985; Kranck and Milligan, 1988; Alldredge and Gotschalk, 1989; Riebesell, 1991b, 1991a; Kranck and Milligan, 1992; Kepkay *et al.*, 1993; Kiorbe *et al.*, 1994; Li and Logan, 1995). The relatively rapid aggregation of suspended material will change the particle areal density distribution as larger particle sizes increase and may result in a corresponding change in the spectral dependence of the backscattering coefficient. Little is known, however, about how aggregation affects the size distribution of the particles less than 100μm. Aggregates may be unbiased samplers of the optically important, less than 100μm portion of the suspended particle size distribution. As such, with aggregation, no change in the shape of spectral backscatter from small particles will to occur. Alternatively, aggregates may be size selective and therefore, with aggregation, a change in the shape of spectral backscatter may occur.

This investigation makes *in situ* measurements that will elucidate the effect of flocculation on the spectral dependence of backscatter in a coastal environment. The goal is to investigate the evolution of the suspended particle size distribution over the course of a phytoplankton bloom and explore correlations with the observed changes to the backscattering coefficient relative to wavelength.

5.2 Methods

The Hydroscat–6 (Hobi Labs) measures the backscattering coefficient at six wavelengths, 442, 470, 510, 589, 620 and 671nm. The instrument was profiled weekly from February 26 to April 30, 1998 at a sampling frequency of 2 Hz and drop rate of 0.3m s^{-1} resulting in a measure of backscatter approximately every 0.17m. Backscatter estimates at each wavelength were corrected using the default correction algorithm (see Chapter 3, Maffione and Dana, 1997) and backscatter due to water was subtracted using estimates from Smith and Baker (1981). Finally, the particulate backscatter coefficient estimate was binned to within plus and minus 0.25m from the corresponding image depth. Binned backscatter was used to decrease the noise in the data and increase confidence in the mean value. The binned backscatter values were then normalized to the value at 442nm so that changes in the shape of the backscatter versus wavelength were more obvious.

Digital silhouette images were analyzed using Media Cybernetics' Image Pro Plus (IPP) image analysis software. The area for each particle was calculated as the sum of adjoining pixels with a 256 grey scale pixel value greater than 226. The threshold value of 226 was chosen because it provided the clearest particles without adding noise. Particle areas from IPP were exported to a Microsoft Access database and equivalent circular diameters were calculated as

$$D = \sqrt{\frac{4 \cdot A}{\pi}} \tag{5.3}$$

where A is the area of the particle. All particles in an image were binned into one of 28 size class bins with median diameters separated by 0.3ϕ units where

$$\phi = \frac{-\ln d(mm)}{\ln 2} \tag{5.4}$$

Maximum ϕ was 3.3, corresponding to a minimum equivalent circular diameter of approximately 100μm. Once binned into a size class, the total area in each class was calculated as the sum of all areas for particles with equivalent circular diameters falling into that class. The particle areal size distribution was used in this study

since it is the projected area of a particle that is important for scattering efficiency (Kullenberg, 1974; Morel, 1991).

The area fraction for each size class ($A_f(d_i)$) was calculated as

$$A_f(d_i) = \frac{A(d_i)}{A_T} \tag{5.5}$$

where i=1,...,28 are the size class bins, $A(d_i)$ is the particle area in a given size class and

$$A_T = \sum_{i=1}^{28} A(d_i) \tag{5.6}$$

is the total area of particles in a given image. The area of particles per–unit–volume (m^2m^{-3}) for each size class ($A_v(d_i)$) was calculated as

$$A_v(d_i) = \frac{A(d_i)}{V_{photo}} \tag{5.7}$$

where i and $A(d_i)$ are as defined above and V_{photo} is the volume of the photo ($5.77\times10^{-5}(m^3)$) which was calculated as the area of the image analyzed by the depth of field of the photo. A total of 1078 image size distributions with corresponding backscatter versus wavelength, spanning all ten weeks of data collection, were available for the study.

Cluster analysis was used to partition images into groups based on their areal size distribution. Cluster analysis seeks to form groups such that objects (images) in the same group are similar to each other with respect to parameter values, whereas objects in different groups are as dissimilar as possible. Agglomerative hierarchical cluster analysis starts with all objects apart and fuses objects or groups successively based on distances between objects and/or groups until all have been joined into one cluster (Spath, 1980; Kaufman and Rousseeuw, 1990). The distance between objects is calculated as the difference between the object parameters. Parameters for this study were either the areal fraction or area per–unit–volume in each of the size class bins. Only the first eighteen of the 28 size classes were found to contain data for some images and therefore the zero values for classes 19 to 28 ($\geq$6350μm equivalent circular diameter) were excluded during analysis because a parameter containing no

information acts to make clustering results less apparent (Kaufman and Rousseeuw, 1990). Distances between objects can be calculated using a variety of algorithms (for examples Hartigan, 1975; Spath, 1980; Kaufman and Rousseeuw, 1990). For simplicity and because they are geometrically easy to understand, both Euclidian and city block (Manhattan) distances (δ) were used. Euclidian distance is calculated as

$$\delta_{euc}(i,j) = \sqrt{(x_{i1} - x_{j1})^2 + \cdots + (x_{ip} - x_{jp})^2} \tag{5.8}$$

where 1,...,i,...,j,...,r are the objects (images) and 1,...,p are the parameters (area per–unit–volume or area fraction in size class). Euclidian distance represents the true geometric distance (shortest straight line) between two objects (Kaufman and Rousseeuw, 1990). City block distance is calculated as

$$\delta_{cb}(i,j) = |x_{i1} - x_{j1}| + \cdots + |x_{ip} - x_{jp}| \tag{5.9}$$

where notation is the same as Equation 5.8.

Once the distance between objects is calculated, agglomerative hierarchical clustering joins the two objects with the least distance thereby creating a group or cluster. The linkage distance between objects and clusters or between clusters and other clusters can also be calculated using different algorithms (for example Hartigan, 1975; Spath, 1980; Kaufman and Rousseeuw, 1990). For this study, two linkage algorithms were used, average and complete. Average linkage is the mean of all distance $\delta(k,l)$'s where k is an element of one group and l is an element of another (where here a group may be a single object). Complete linkage uses the largest distance $\delta(k,l)$ between elements of groups to determine linkage distance. The average linkage algorithm is relatively robust to finding groups whether they are well separated or not. Complete linkage tends to result in compact clusters into which outlying points are not easily incorporated and may result in clusters that are not well separated since they will not be joined as long as two elements remain distant (Kaufman and Rousseeuw, 1990).

The combination of distance and linkage algorithms results in four different clusterings for a given data set. In order to determine which combination resulted in the

'best' clustering of the data, the cophenetic correlation (cc) coefficient was calculated. The cc–coefficient compares the distances calculated for the objects to the final clustering linkages. The final linkages should be strongly correlated with the distances and therefore the better the clustering solution, the closer the cc–coefficient value should be to one (Matlab, 1999). As such, the combination of distance and linkage algorithms that resulted in the highest cc–coefficient was used.

Once clusters of the areal size distributions were obtained, they were taken as groups of images that represented water with different particle size compositions. These groups were used as dummy independent variables to test for differences in the shape of the corresponding measured backscatter normalized to backscatter at 442nm using a 2-way repeated measures (on wavelength) MANOVA (multivariate analysis of variance). For the test, the groups of particle size distributions became the between images variable while wavelength was the within image variable.

The desired test within the 2-way repeated measures MANOVA is for significance of interaction between the levels of cluster group and levels of wavelength. A significant interaction term indicates a shape effect for cluster group within the wavelengths. Therefore, the spectral shape of backscatter is not the same for all cluster groups if the interaction term is significant. The null hypothesis of the test for interaction is that the spectral shapes of backscatter ratios for different cluster groups are the same shape. The alternative hypothesis is that, for different particle size distribution groups, the spectral shape of backscatter is different.

5.3 Results

Clustering was performed on the area fraction and the area per–unit–volume data. The resulting cophenetic correlation coefficients for area fraction data were <0.5 in all combinations of distance and linkages whereas area per–unit–volume cc-coefficient values were >0.5. Therefore, clustering was performed on the area per–unit–volume data and only the results involving the area per–unit–volume are presented.

An examination of the removal of outliers–objects that remained singular until the final clusters were formed–from the clusters of the whole data set (1078 size distributions) resulted in robust clusters within the same combinations of distance and linkage algorithms chosen. Therefore, for final clustering, no outliers were removed.

Because a different relationship was seen for the observed versus predicted backscatter data from February 26 to March 19 than that from March 26 to April 30 (see Chapter 4), the two sets of days were split for clustering. For both sets of days, the highest cc coefficient was observed when an average linkage was chosen regardless of distance. The resulting clusters using both euclidian and city block distance were fairly robust and final cluster groups for both sets of days were chosen based on the results of clustering and examination of the images within a cluster. For each plotted mean, the standard error was calculated as

$$se = \frac{\mathrm{SD}}{\sqrt{r}} \tag{5.10}$$

where SD is the standard deviation of the data, and r is the number of data points. The standard error value is presented as an error bar for the mean value. Figure 5.1 shows the resulting mean size distributions for the final five clusters for February 26 to March 19. The first cluster (cl=1) has the largest number of images forming the size distribution, 345 in total. This cluster also has overall smaller particles at a lower concentration (see the y–intercept of Figure 5.1) than the other four clusters (cl=2–5) which had fewer images per cluster (r=1–9) but larger particles (see Figure 5.1). Figure 5.2 also shows the clustering for days February 26 to March 19 but, the four small clusters from Figure 5.1 were combined to increase the total number of images of larger particles at higher concentrations grouped into one cluster. The two clusters of image particle size distributions in Figure 5.2 are separated, but the standard error bars in the larger particle sizes of cluster number two are larger than when the clusters were not grouped into one. Figure 5.3 shows the resulting mean size distributions for the final four clusters from March 26 to April 30. Similar to the clusters found for February 26 to March 19, the cluster for March 26 to April 30 with the largest number of objects (cl=1) also has the lowest concentration and smaller

particles than the other three clusters. However, this set of days contains a cluster with 103 images (cl=2) that has a higher concentration of particles although most are less than 1000μm.

The two-way repeated measures MANOVA was run for both sets of days and the two clusterings of February 26 to March 19. The cluster group numbers associated with each normalized spectrum were used as the independent dummy variables and the five ratios of measured backscatter to backscatter at 442nm were used as the repeated measure dependent variables. Note that the backscatter at 442nm ratio to itself was not included since in all cases its value equals one. The null hypothesis for the test of interaction between the backscatter ratios and the cluster groups is that there is no interaction effect between the levels of particle size distribution cluster group and the shape of the backscatter ratios as a function of wavelength. If the spectral shape of the backscatter ratios between cluster groups are not the same, then a significant interaction term will be found. For all tests, the interaction between cluster group and wavelength was found to be significant with a p-value less than 0.001 (see Table 5.1). Both the Wilk's Lambda and Pillai Trace test statistics are presented

Table 5.1: Results of the test for interaction effects in the two-way repeated measures MANOVA between cluster groups of particle areal size distributions and measured backscatter ratios as a function of wavelength.

Day	# Groups	# Samples	Test Stat	p-value
26/02/98-	5	360	Wilk's Lambda	<0.0001
19/03/98	5	360	Pillai Trace	<0.0001
26/02/98-	2	360	Wilk's Lamdba	<0.0001
19/03/98	2	360	Pillai Trace	<0.0001
26/03/98-	4	718	Wilk's Lambda	<0.0001
30/04/98	4	718	Pillai Trace	<0.0001

as multivariate analysis of variance test statistics. They are essentially equal for large samples although Pillai's Trace is more robust against non-normality (Johnson and Wichern, 1998).

To better understand these results, Figure 5.4 shows the mean backscatter with wavelength for the corresponding measurements to the image size distribution cluster groupings found for February 26 to March 19 with five clusters and Figure 5.5 shows the same for two cluster groups. The normalized spectra with five clusterings shows that the spectra associated with images of larger particles (cl=2, 3, 4 and 5) are basically flat to positive, although all values dip at 671nm. The spectra for images with smaller particles has an overall more negative slope (cl=1). When the spectra are combined to form only two clusters, the difference is more obvious. The spectra associated with larger particles (cl=2) is higher for all wavelengths but particularly for those in the green–yellow region (510nm and 589nm). It is also interesting to note that none of the standard errors for the wavelength ratio means of the different clusters overlap.

Figure 5.6 shows the corresponding backscatter with wavelength for clusters found for March 26 to April 30. These spectra are much less different than those seen for the clusterings from the first set of days. Most of the standard errors for the ratio means overlap with the exception of 589, 620 and 671nm of cluster number four which represents the cluster with the largest particles (see Figure 5.3). These spectra are more peaked at 470 and 510nm than those seen for February 26 to March 19 but lie between the two spectra from Figure 5.5 for 589nm and at the same level as 620 and 671nm for the cluster of smaller less concentrated particles.

5.4 Discussion and Conclusions

Changes in *in situ* particle areal size distribution were found and the corresponding wavelength dependence of backscatter were assessed to determine if corresponding changes occurred. Results show significant interaction effects and therefore that the shape of backscatter with wavelength is not equal for all levels of particle size distribution groups. Images with different particle areal size distributions have corresponding shapes of backscatter spectra that are not the same.

The main goal of clustering is to group and summarize data into smaller subsets of the larger set (Hartigan, 1975; Sandland and Young, 1979). Therefore, if an object in a cluster has a given characteristic, it can be expected that other objects in the same cluster will have the same characteristic (Hartigan, 1975). However, clusters are only as revealing as the data they are based on. Further, clustering algorithms may impose structure where none is present (Sandland and Young, 1979).

The basic problems in clustering data arise from the selection of distances, linkage algorithms, and final cluster number, as well as the choice of variables (Spath, 1980). By using two distance and two linkage algorithms and choosing the best combination based on the cophenetic correlation coefficient and comparisons between results, the final clustering can be assumed to be robust and genuine (Green, 1979). Further, by using practical interpretation of the final clustering to decide on the number of groups to keep, chances of meaningful clustering were improved (Spath, 1980).

The number of images was such that it eliminated the use of many clustering methods in available statistics programs. Matlab could handle calculating the $\frac{n\cdot(n-1)}{2}$ (=64 000, 260 000) distances between objects that had to be calculated. While hierarchical methods can not repair a linkage that was made in a previous step, they offer the advantage of not requiring a user defined number of final clusters. Hierarchical methods also tend to be computationally less restrictive and do not require subsampling of the data set as k-means methods on large data sets require (Kaufman and Rousseeuw, 1990). Therefore, agglomerative hierarchical clustering was chosen over a k-means method because the computation algorithms were available, required the least computer time cost and hierarchical clustering techniques do not require that the final number of clusters be chosen before clustering.

Figures 5.4, 5.5 and 5.6 show the mean normalized backscatter with wavelength and the standard error of each mean for the areal size distribution cluster groups. Although the curves for February 26–March 19 appear to be different, the error bars for March 26–April 30 overlap at two points. Further, no discernable consistent change in the shape of backscatter spectra was observed for like changes in the particle size

distribution between sets of days (small to large particles and low to relatively high concentration). A similar difference in the particle size distribution, the difference between the clusters which represent images that contain fewer and smaller particles (cl=1 for all clusterings) versus the other clusters found, did not result in a similar change in the corresponding spectral shapes of backscatter. The backscattering spectral shape for cluster #1 of February 26 to March 19 was less curved than the shape of the backscatter associated with cluster number one for March 26 to April 30. Although the statistical test showed significant differences between cluster groups, there may be reason to question the result since the same change in the shape of spectral backscatter was not observed between groups of days. Further, the shape of the backscatter as a function of wavelength curve for the cluster of larger, more highly concentrated particles for February 26 to March 19 was more flat than the shape for the clusters of larger particles from March 26 to April 30.

Using a MANOVA test requires that assumptions be made about the probability distribution and independence of the data (Stevens, 1986; Johnson and Wichern, 1998). The distribution of backscattering ratios is required to be multivariate normal. Multivariate normality requires that all distributions be univariately normal; each backscattering ratio must have a normal distribution. However, even if all are univariate normal, this does not assure multivariate normality. A nonparametric Lilliefor's test for normality on each of the five sets of ratios resulted in rejection of the null hypothesis that the data were normally distributed at p-values less than 0.01. Figures 5.7 and 5.8 show the frequency distributions for the ratios for each set of days. Although the data are not normally distributed according to the Lilliefor's test, the frequency distributions are relatively bell–shaped. A variety of transformations did not normalize the backscatter ratios. Since univariate normality was not met, multivariate normality could not be. However, because the data sets are so large (r=360, 718), it can be assumed that the test is fairly robust to the deviations from normality.

The MANOVA also requires independence between samples. Independence requires that all measurements of backscatter be uncorrelated with one another. Because the data are measured in a profile over depth, and a few times at each depth for each day, it is probable that some spatial and/or temporal autocorrelation may be present. The effects of this autocorrelation can be presented in terms of the degrees of freedom in the statistical test. The presence of autocorrelated data results in an overestimation of the actual degrees of freedom used in the statistical test (Legendre and Legendre, 1998). The overestimation would occur in the degrees of freedom associated with the number of images within wavelengths and effectively decreases the value of the test statistic, tending to result in significance where none is actually present. However, p-values were zero to three decimal places suggesting a strong effect in spite of the tenuous assumptions of independence and normality.

It is interesting to note that the largest portion of images in both sets of days had lower concentrations and smaller sizes (see Figures 5.1, 5.2 and 5.3). Inspection of the images showed that those that made up the clusters with more and larger material were generally found in the surface waters ($\leq$5m) from March 19 to April 9 but on April 16 and for one image on April 23, images with more and/or larger particles were found in deeper waters. It is likely that this was a result of the bloom senescence and loss of high particulate load in the surface waters via sinking aggregates.

The results of the statistical tests point to a change in the shape of the backscattering coefficient with wavelength when a change in the particle areal size distribution is observed. Differently shaped spectra are definitely observed. However, the results of the statistical test may be of less practical significance than statistical. The large sample numbers and partial autocorrelation may have given results more significant than are actually present. Isolated very different spectra may be causing the significance. For example, Figure A.4 in Appendix A has an interesting and different backscatter spectrum at $\sim$5m on March 19 with a peak in the measured backscatter at 589nm. This spectrum is correlated with a particle areal size distribution that was classified into a cluster grouping of smaller, less concentrated material (cl=1,

Figure 5.1 or 5.2). However, the chlorophyll measured by the fluorometer, presented in the fourth panel of Figure A.4, was also peaked at ~5m. Other factors both correlated and not correlated with the changes in particle areal size distribution may be combining to give the significant result.

None of the shapes of backscatter with wavelength look like what was expected from theoretical studies (see Equation 5.1). All were either humped at some portion of the spectrum, typically in the blue to green (470 and/or 510nm) or green to yellow (589nm). This may be a function of the correction algorithm since the default algorithm used is not wavelength dependent and may underestimate correction at particularly 442 and 671nm (see Chapter 3). Further, backscatter will be changed by the absorption spectra of light in the system as was observed by Stramski and Reynolds (1993).

This is an important step towards understanding the shape of the backscattering spectra, and more study into the effects of changes in the *in situ* size distribution should be made. Specifically, a study of the *in situ* size distribution less than 100μm combined with that greater than 100μm and measurement of the backscatter coefficient as a function of wavelength could elucidate why the shape of backscatter with wavelength was so similar for the latter half of the bloom (after March 26, see Figure 5.3).

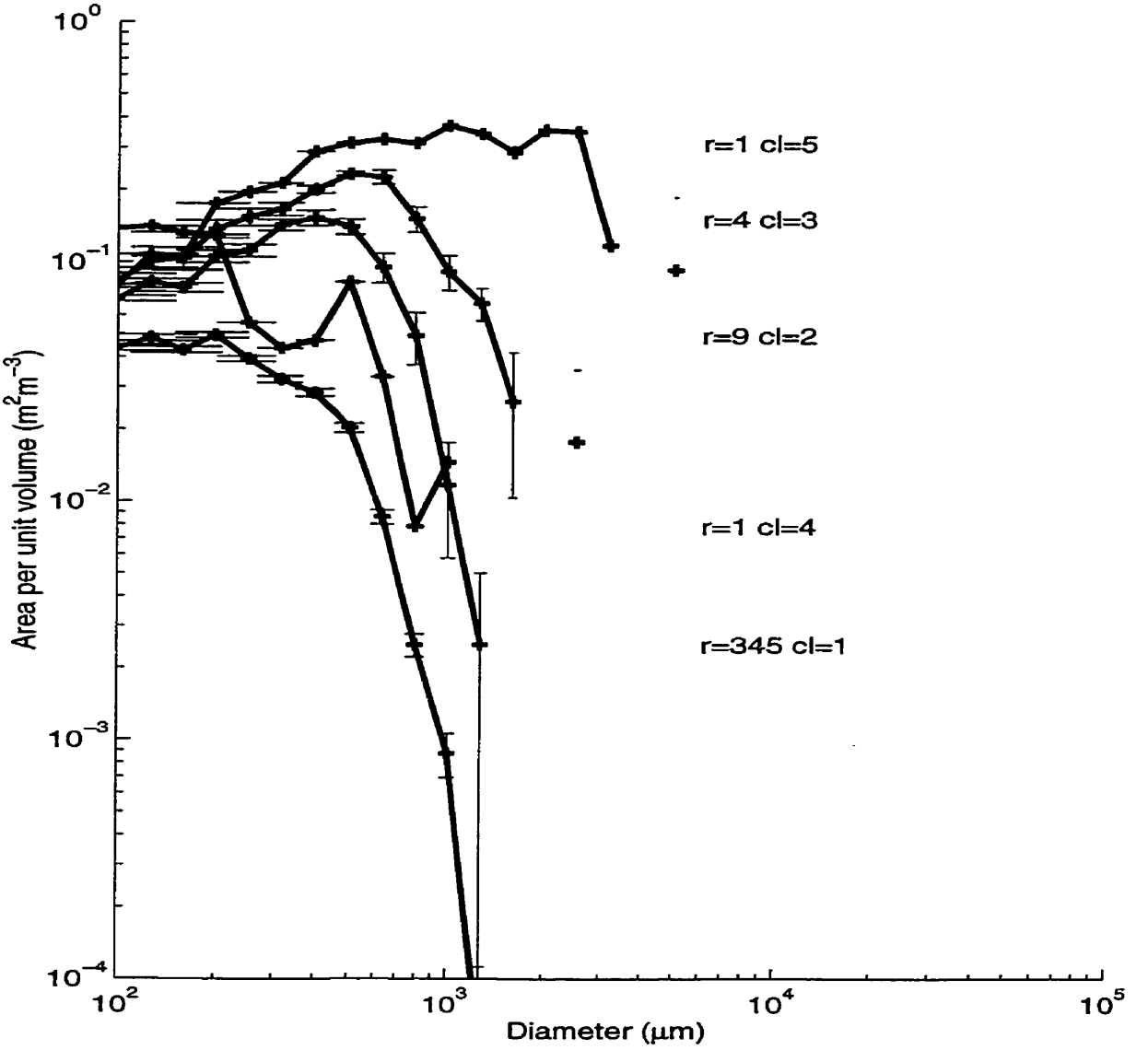

Figure 5.1: Particle mean areal size distribution with standard error about the mean for clusterings from February 26 to March 19, 1998. The number of images for each curve is given as r and the cluster number is cl.

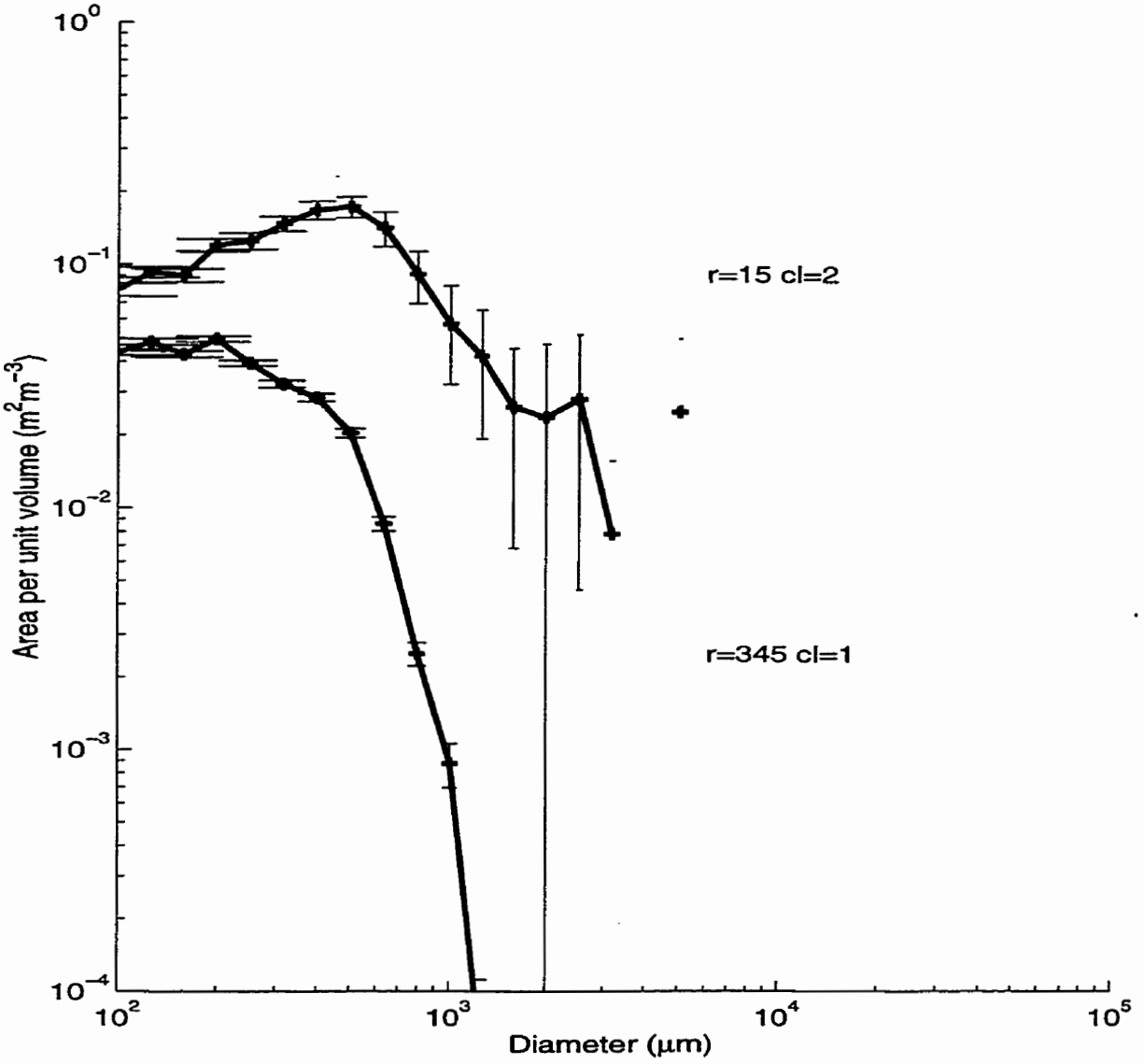

Figure 5.2: Particle mean areal size distribution with standard error about the mean for combined clusterings from February 26 to March 19, 1998. The number of images for each curve is given as r and the cluster number is cl.

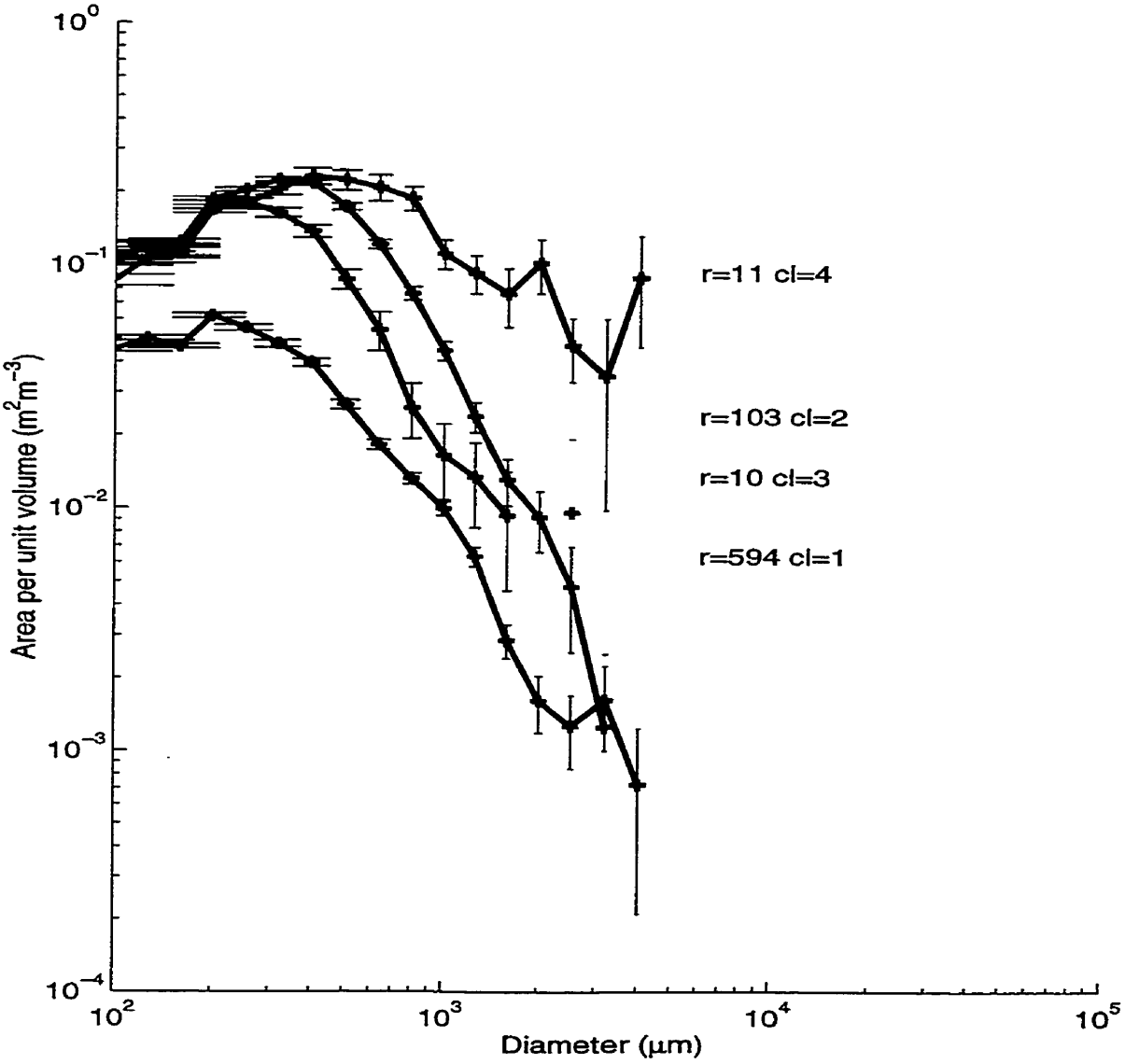

Figure 5.3: Particle mean areal size distribution with standard error about the mean for clusterings from March 26 to April 30, 1998. The number of images for each curve is given as r and the cluster number is cl.

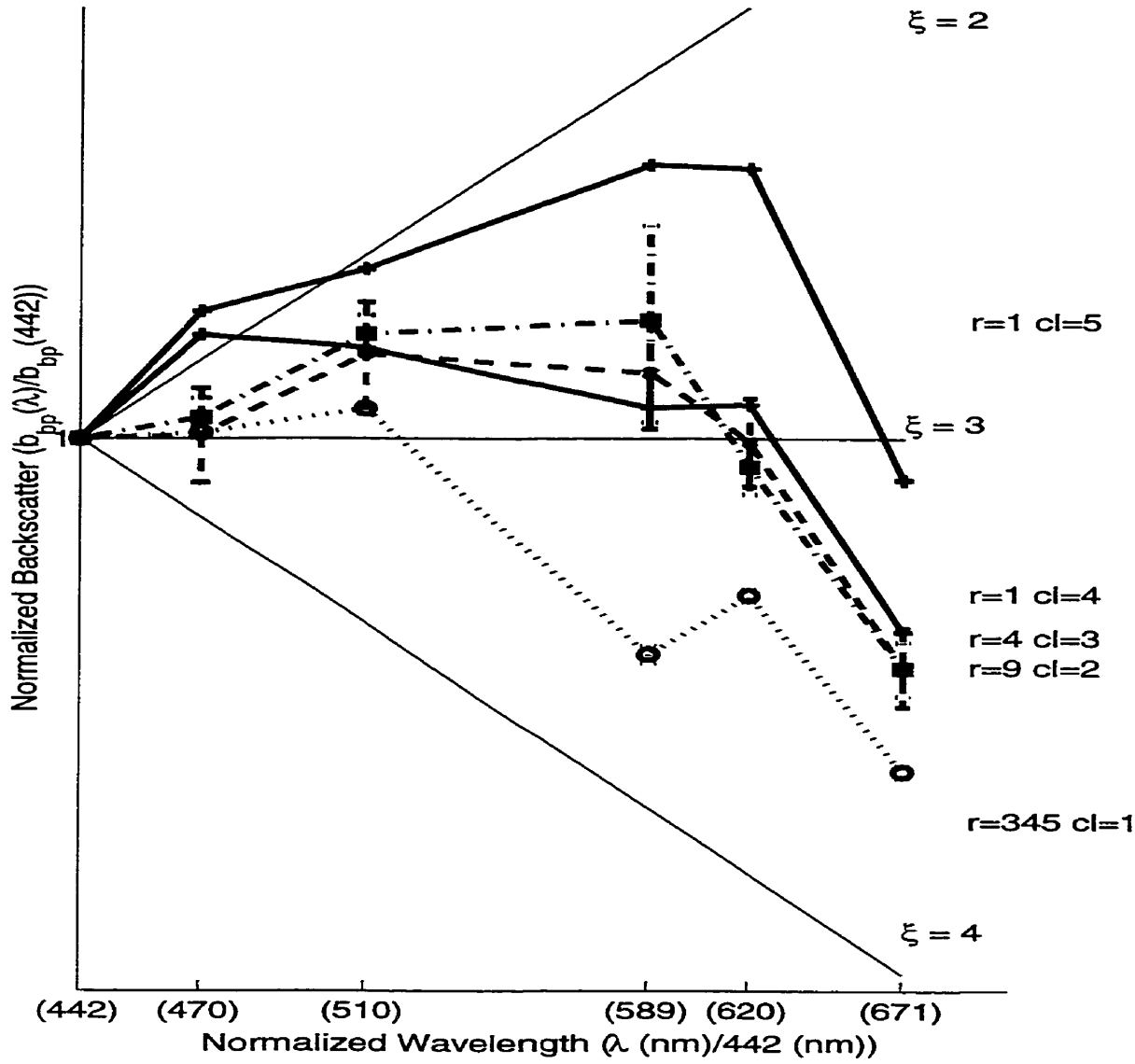

Figure 5.4: Mean backscatter ratios versus normalized wavelength on log–log axes and corresponding to the particle area size distribution clusters of Figure 5.1 with standard error about the mean for February 26 to March 19, 1998. The number of images for each curve is given as r and the cluster number is cl. Also plotted on the graph are the theoretically expected shapes of spectral backscatter for Junge slope values of ξ=2, 3 and 4 with resulting theoretical slope values of -1, 0 and 1 respectively.

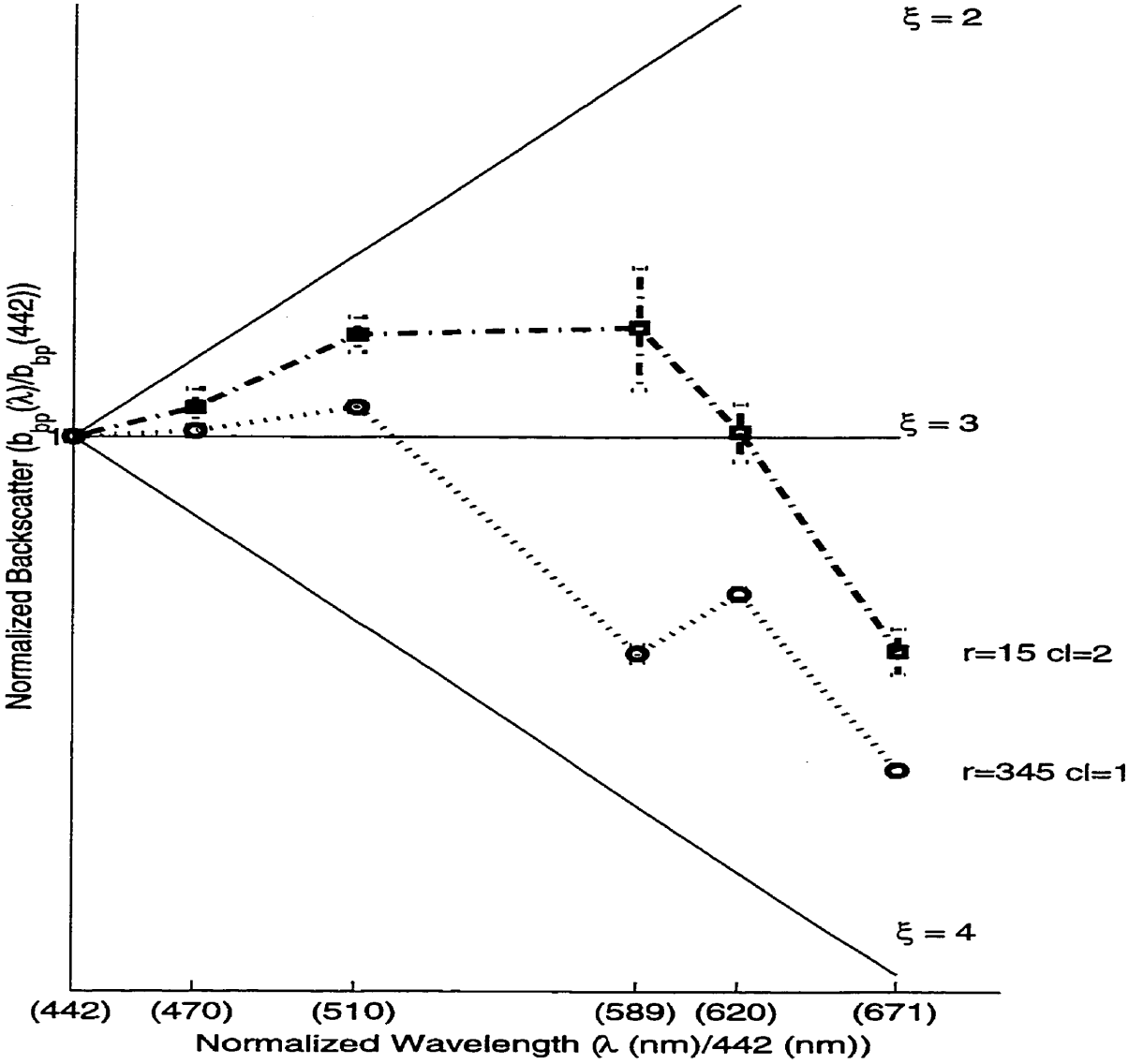

Figure 5.5: Mean backscatter ratios versus normalized wavelength on log–log axes and corresponding to the combined particle area size distribution clusters of Figure 5.2 with standard error about the mean for February 26 to March 19, 1998. The number of images for each curve is given as r and the cluster number is *cl*. Also plotted on the graph are the theoretically expected shapes of spectral backscatter for Junge slope values of ξ=2, 3 and 4 with resulting theoretical slope values of -1, 0 and 1 respectively.

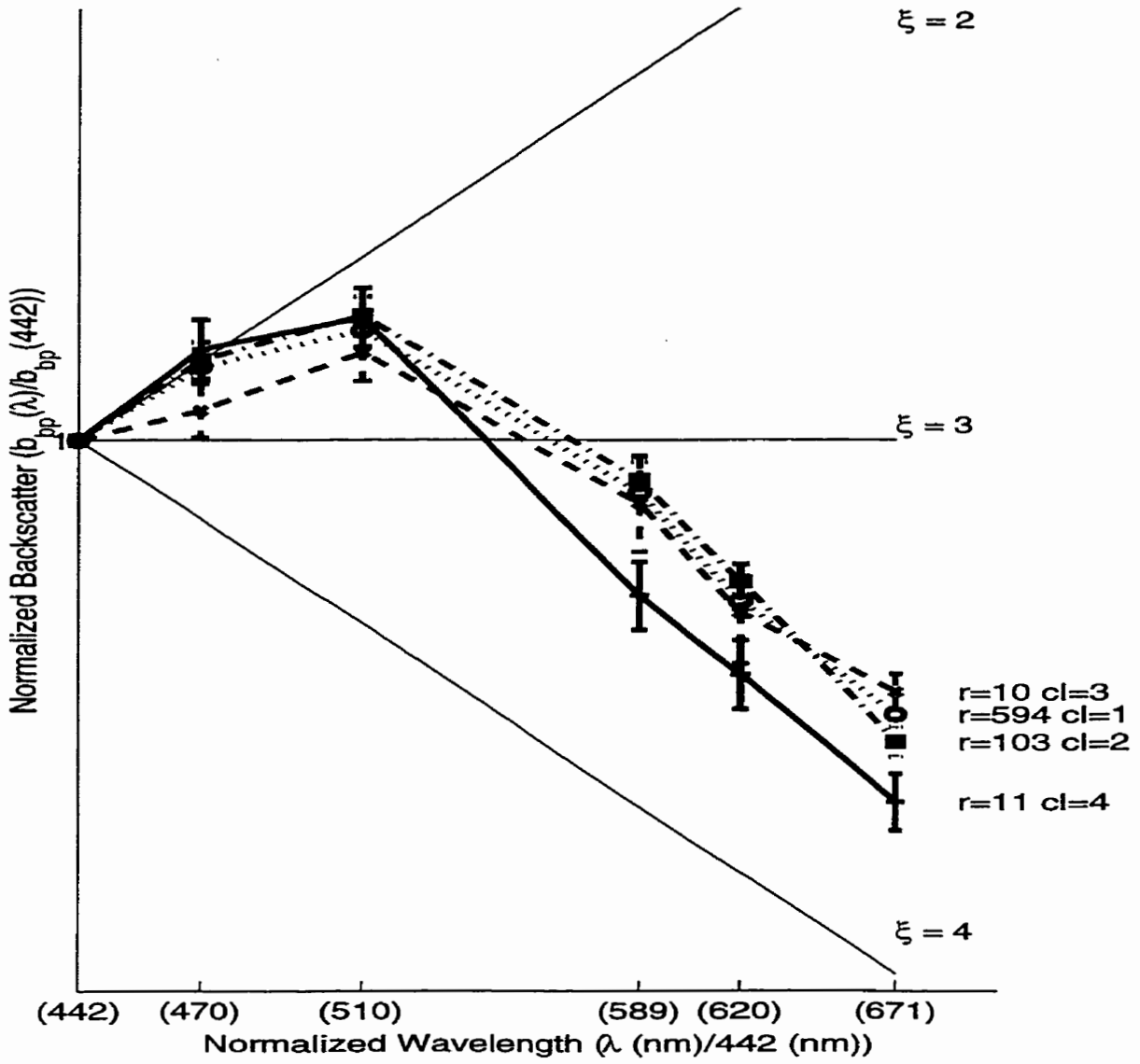

Figure 5.6: Mean backscatter ratios versus normalized wavelength on log–log axes and corresponding to the particle area size distribution clusters of Figure 5.3 with standard error about the mean for March 26 to April 30, 1998. The number of images for each curve is given as r and the cluster number is cl. Also plotted on the graph are the theoretically expected shapes of spectral backscatter for Junge slope values of ξ=2, 3 and 4 with resulting theoretical slope values of -1, 0 and 1 respectively.

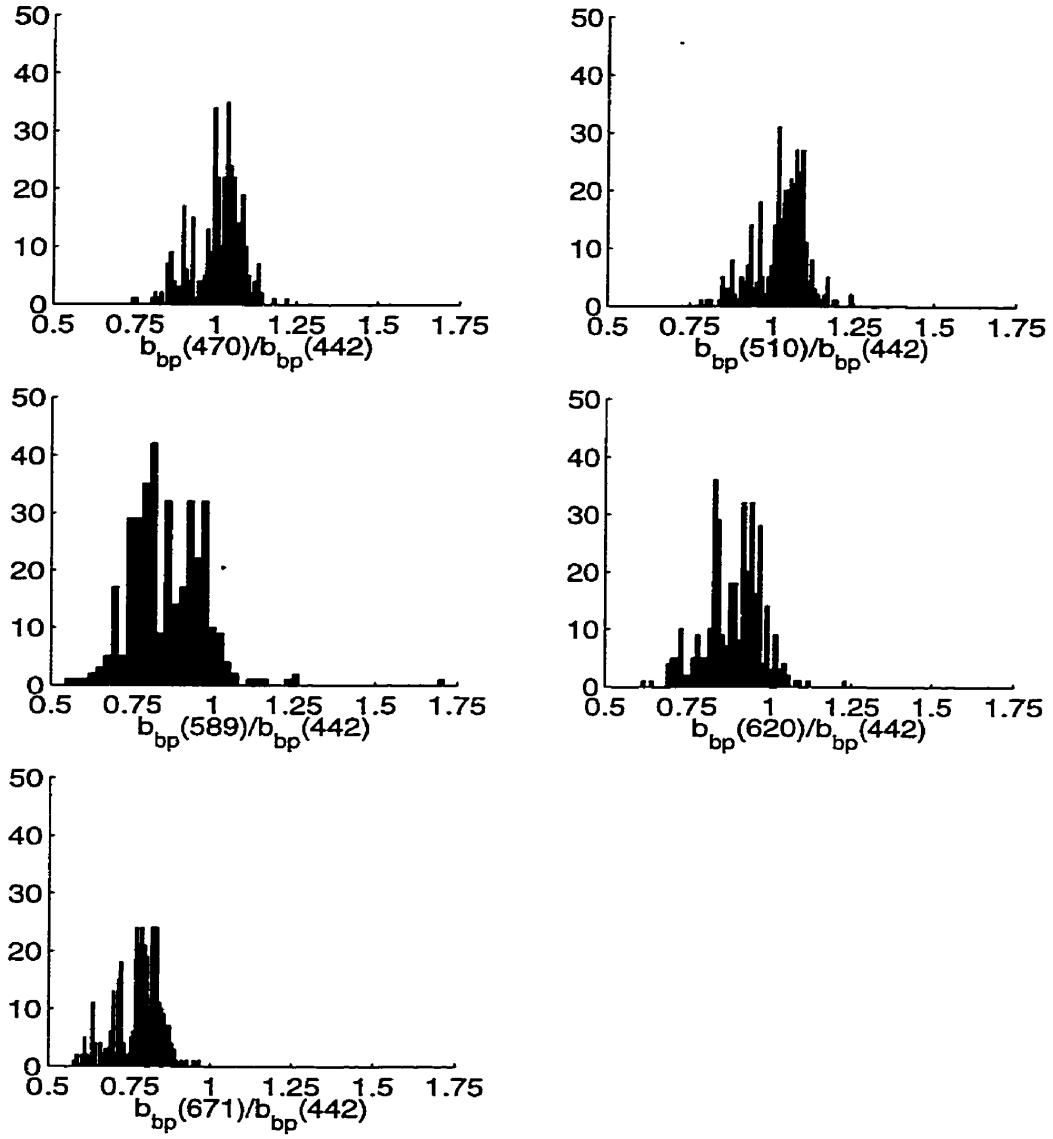

Figure 5.7: Frequency distributions of the backscattering ratios used as the dependent variables in the MANOVA test for days February 26 to March 19.

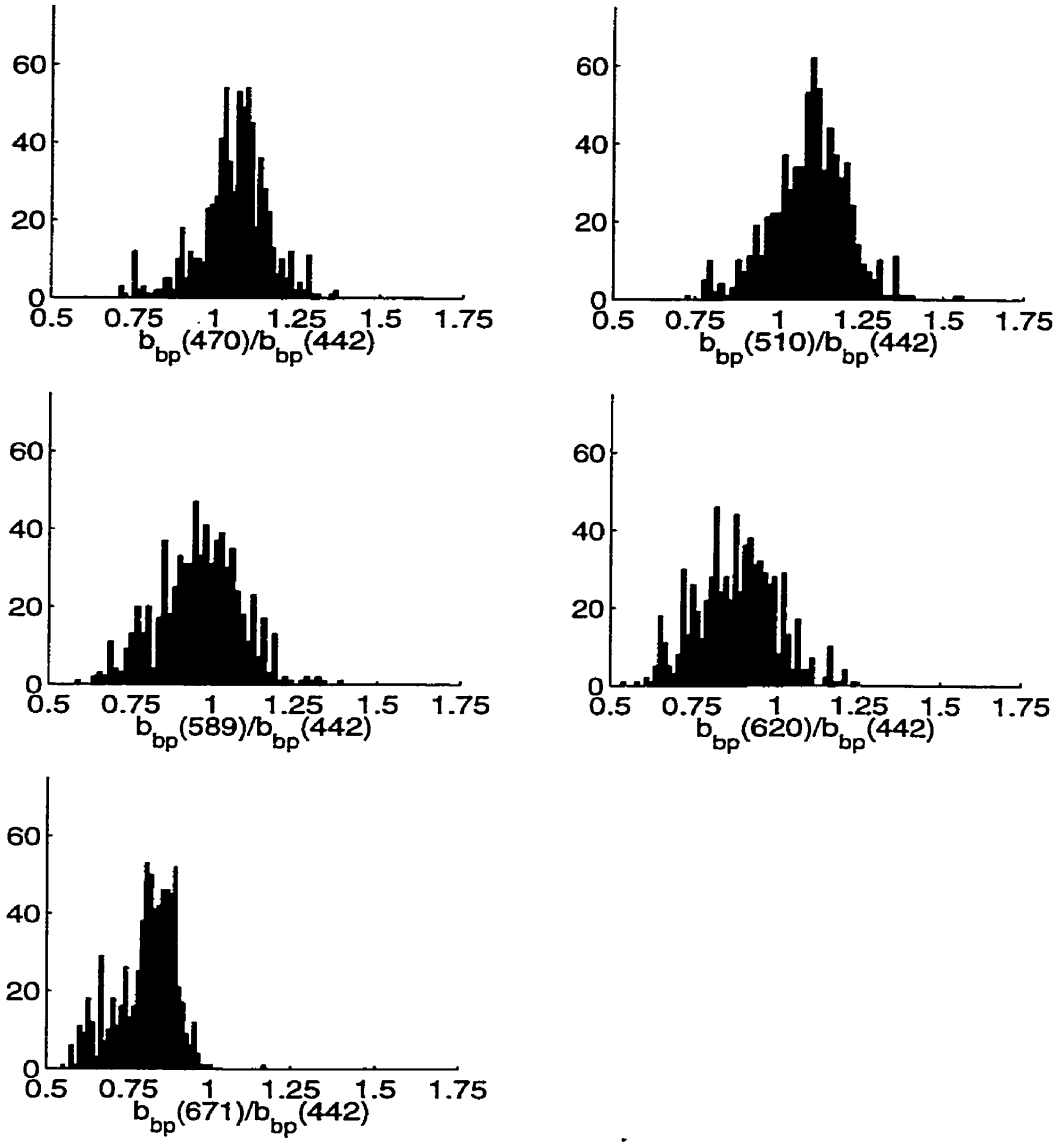

Figure 5.8: Frequency distributions of the backscattering ratios used as the dependent variables in the MANOVA test for days March 26 to April 30.

Chapter 6

Conclusions

This study is the first to present simultaneous measurements of *in situ* particle size distributions and wavelength dependent backscattering coefficients. The measurements, made over the course of the 1998 spring phytoplankton bloom in Bedford Basin, NS, allow for estimation of the accuracy of the correction algorithm for the Hydroscat pathlength attenuation, the prediction of backscatter from particles $\geq 100\mu$m and facilitate the examination of the correlation between the shape of the wavelength dependence of the backscattering coefficient and particle distributions $\geq 100\mu$m.

The correction algorithm for pathlength attenuation of the Hydroscat LED beam was found, in this study, to cause at most a 25% difference in the final estimate of particulate backscattering coefficient regardless of the estimate of the backscattering ratio. This lends confidence to the backscatter estimates that are corrected with the default algorithm when no supplemental optical measurements are available. Inspection shows that the largest effects of correction algorithm occurs between wavelengths although some effect is seen with depth and day. This wavelength effect is likely a result of the wavelength dependence of absorption that is not accounted for with the default correction algorithm. The largest differences between the correction algorithms were found when the relative chlorophyll *a* concentrations were also the highest and therefore the absorption was expected to be highest.

Although the correction for the pathlength attenuation algorithm did not make

a large difference (generally less than 10%) in the final backscatter estimate, the wavelength effect in the correction difference is noteworthy. Hydroscat measurements should be corrected with independently measured optical properties when available in order to include wavelength dependence and potential difference between surface and deeper water optical properties.

An interesting result from this study is the strong relationship between measured backscatter and predicted backscatter based on the size and concentration of particles greater than 100μm. Two different relationships between observed and calculated backscatter were found, with sampling day determining which relationship was appropriate. The intercepts for the relationship between predicted and observed backscatter were statistically similar, suggesting a relatively constant background backscatter from particles that do not covary with the particles visible in the images. The relationship seen for sampling days February 26 to March 19 (the first part of the study) had significantly higher slopes ($\geq$1.2) than those seen for March 26 to April 30 ($\leq$.98), regardless of index of refraction and/or wavelength. The difference in slopes suggests that the particles visible in the images from the first set of days under–predict the observed backscatter, whereas those in the second set of days tend to over–predict observed backscatter. Ancillary data and parameters calculated from the measured data were used to give clues as to the cause of the shift in relationship. The data give evidence for a potential shift not only in the organic/inorganic composition of suspended particles but also their size distribution. Between March 19 and March 26 the shift in relationship between observed and calculated backscatter may have resulted from a shift towards more organic and larger particles that was potentially initiated by the formation of aggregates in the surface waters of March 12 and 19th. The flocs effectively swept the water column of smaller, potentially more inorganic particles present before March 26, changing the relationship between observed and calculated backscatter.

These results suggest the importance of particles >100μm has been underestimated in optical studies. Suspended particle focus within the optical literature is on

single free floating particles as evidenced by calculation and analysis on particles in the range of submicrometer viruses to microplanktonic cells of order 1–10μm in diameter (for example Stramski and Kiefer, 1991). However, literature abounds on marine aggregates composed of such individual particles in large masses typically on the order of 1000μm (for example Kranck and Milligan, 1988; Alldredge and Gotschalk, 1989). This study shows that these particles may account for more of the optical properties of a water mass than has previously been recognized. As such, it is important that *in situ* size distributions be used in optical studies and these distributions be extended into the range <100μm with improved technology to that measure *in situ*.

Groups of particle area per–unit–volume size distributions described at least two types of images. For both the first (February 26–March 19) and the second set of days (March 26–April 30), the largest portion of images were found to contain smaller particles and lower concentrations. Smaller groups were found to contain larger particles with higher concentrations. Inspection of the depth of the images with larger particles showed most were from the surface waters with the exception of those later in the bloom that extended to depths of 10m by April 2 and over 20m on April 16. These groups showed significant interaction effects with backscatter ratios as a function of wavelength . The significant interaction indicates that the spectral shape of the measured particulate backscattering coefficient changes when the particle size distribution changes. However, no consistent change in the shape of the spectral backscatter ratios was observed for similar changes in size distribution between the two groups of days. Although different shapes of the particle backscattering coefficient were observed and detected, the grouping by shape of particle size distribution is likely only one contributing factor and the significance of this result should be looked at with caution. Further, since the change in particle size distribution shape was observed for particles greater than 100μm, more evidence that a similar change in the particles less than 100μm would be invaluable for seeking correlations between changes in shape of the particle size distribution and spectral backscatter coefficient ratios. The measured backscatter as a function of wavelength also did not follow

theoretically expected shapes of the wavelength dependence of backscatter.

It is unclear if the significant change in backscatter shape is a result of the change in particle size distribution. Other factors were likely contributing. A repetition of this study that included more accurate measurement of the factors affecting the index of refraction could prove invaluable and result in better conclusions on the effect of changes in particle size distribution and its effect on the shape of the backscattering coefficient with wavelength.

The accurate and reliable measurement of the backscattering coefficient in natural waters is integral to ocean colour studies, particularly for remote sensing. For these purposes, *in situ* measurements are required. Further, it is important that these measurements be made with little disruption to the ambient particle size distribution so that the optical properties of large fragile aggregates are maintained. This study gives evidence for the importance of aggregates on the optical characteristics of natural waters. Evidence points to aggregates changing the magnitude of backscatter. Their effect on the spectral shape of backscatter, however, remains unclear. Future studies that measure the *in situ* particle size distribution both greater than and less than 100μm as well as the particulate backscatter as a function of wavelength could help to further elucidate the effects of aggregate formation on size distributions and water column optical properties.

Appendix A

Methods: Data summary

Figures A.1–A.10 summarize the data collected throughout the bloom study.

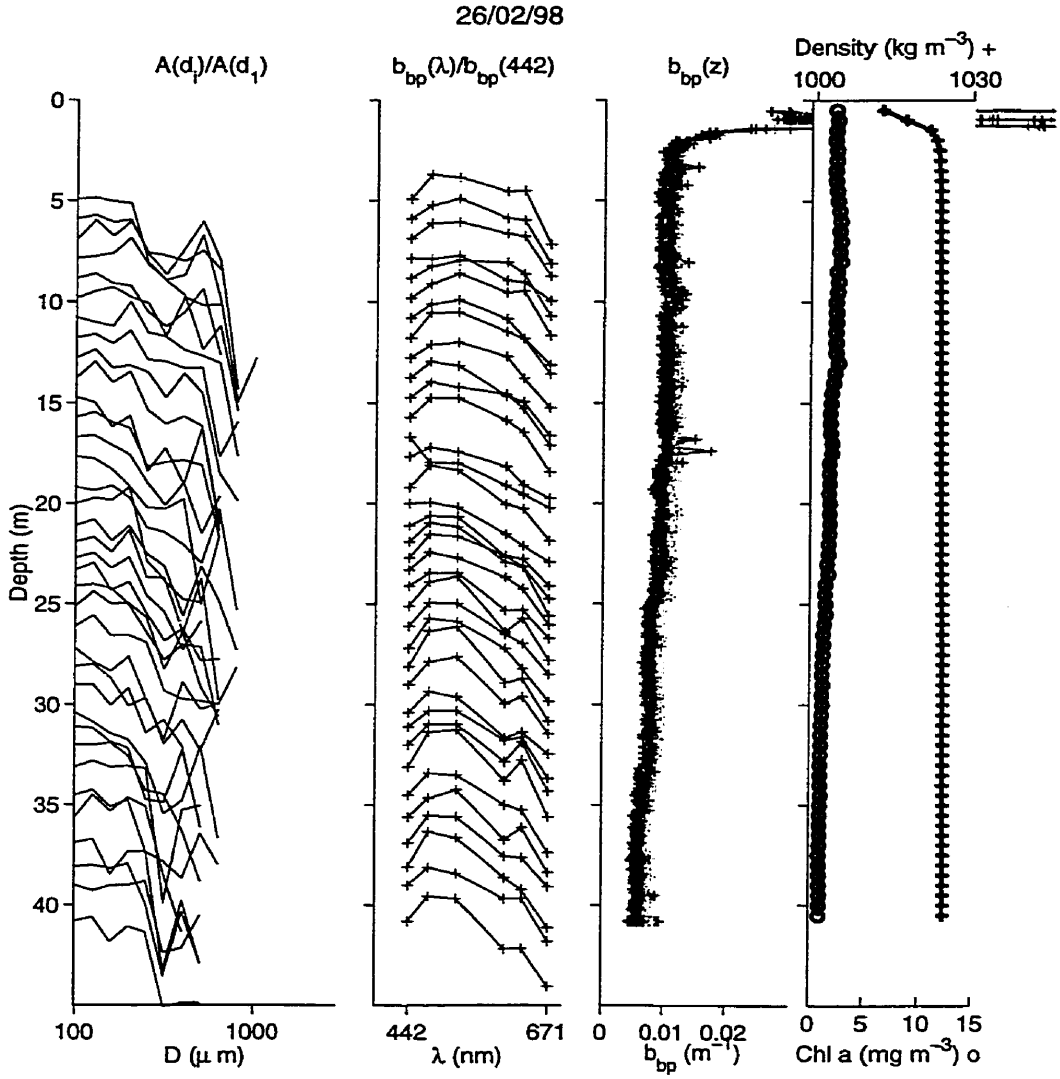

Figure A.1: Plot of all data used in this study collected on February 26, 1998. The first panel shows particle areal size distributions normalized to the value in the first bin and scaled to plot to depth of image capture. The second shows particulate backscatter spectra normalized to the value at 442nm and scaled as in the first panel. The third panel is particulate backscatter profiles for all wavelengths. The fourth panel shows calculated density (+) and estimated chlorophyll *a* (o) profiles.

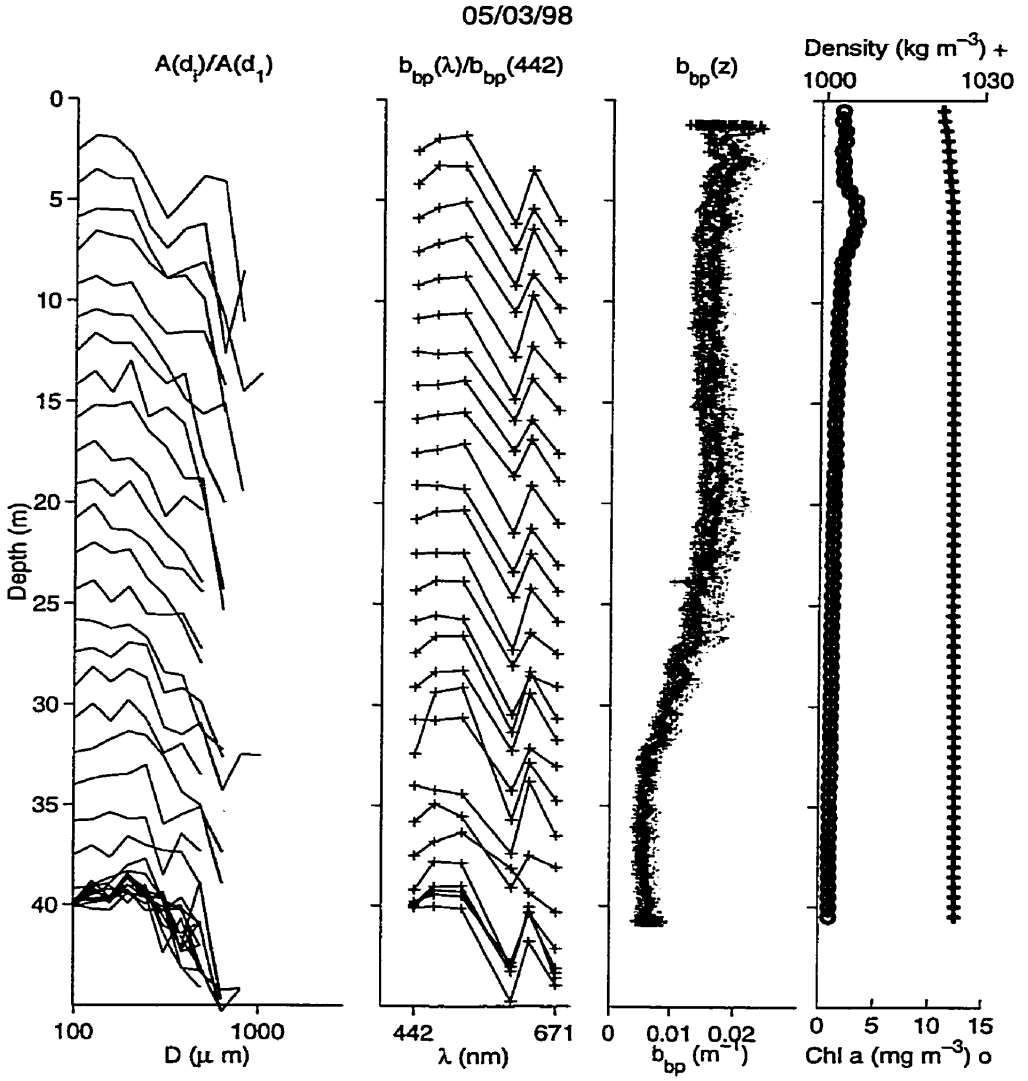

Figure A.2: Plot of all data used in this study collected on March 5, 1998. The first panel shows particle areal size distributions normalized to the value in the first bin and scaled to plot to depth of image capture. The second shows particulate backscatter spectra normalized to the value at 442nm and scaled as in the first panel. The third panel is particulate backscatter profiles for all wavelengths. The fourth panel shows calculated density (+) and estimated chlorophyll *a* (o) profiles.

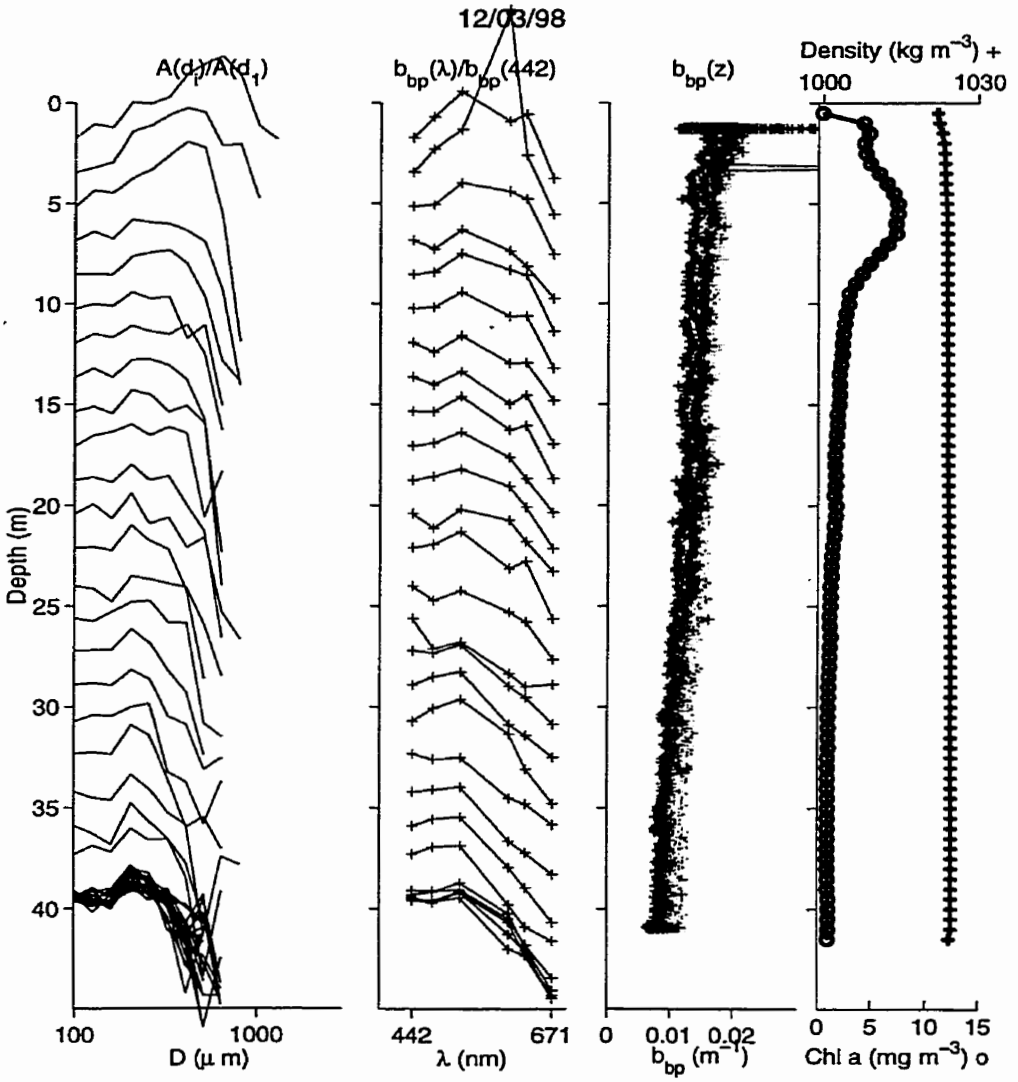

Figure A.3: Plot of all data used in this study collected on March 12, 1998. The first panel shows particle areal size distributions normalized to the value in the first bin and scaled to plot to depth of image capture. The second shows particulate backscatter spectra normalized to the value at 442nm and scaled as in the first panel. The third panel is particulate backscatter profiles for all wavelengths. The fourth panel shows calculated density (+) and estimated chlorophyll a (o) profiles.

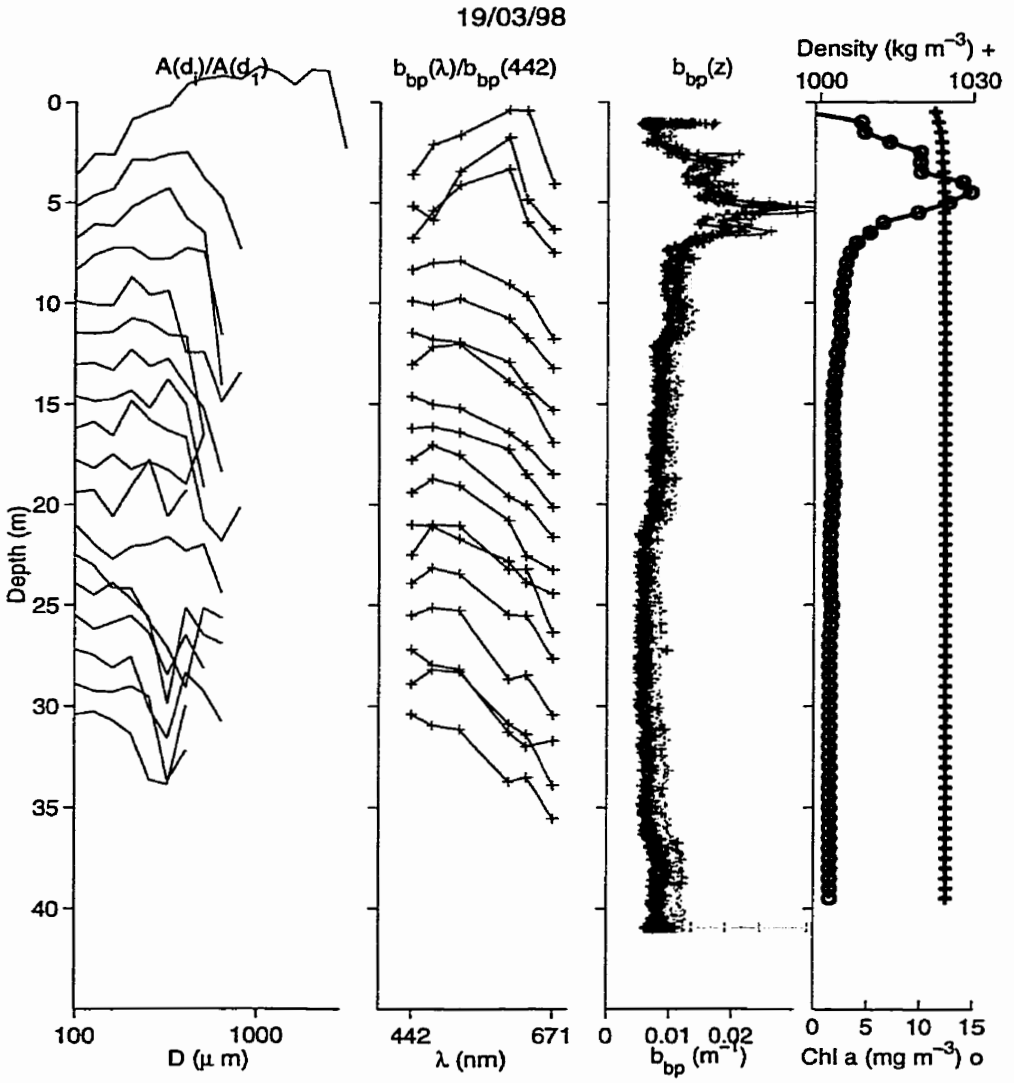

Figure A.4: Plot of all data used in this study collected on March 19, 1998. The first panel shows particle areal size distributions normalized to the value in the first bin and scaled to plot to depth of image capture. The second shows particulate backscatter spectra normalized to the value at 442nm and scaled as in the first panel. The third panel is particulate backscatter profiles for all wavelengths. The fourth panel shows calculated density (+) and estimated chlorophyll *a* (o) profiles.

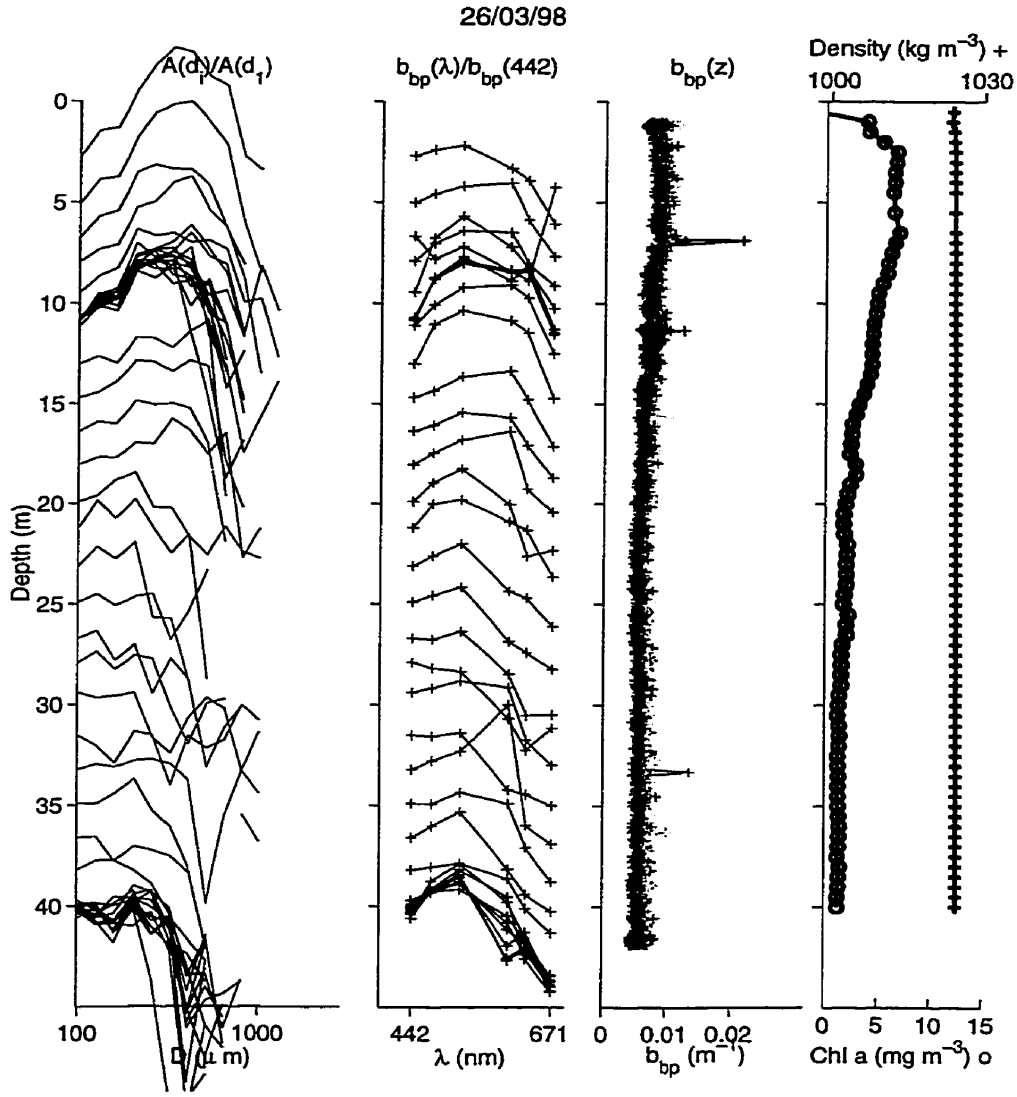

Figure A.5: Plot of all data used in this study collected on March 26, 1998. The first panel shows particle areal size distributions normalized to the value in the first bin and scaled to plot to depth of image capture. The second shows particulate backscatter spectra normalized to the value at 442nm and scaled as in the first panel. The third panel is particulate backscatter profiles for all wavelengths. The fourth panel shows calculated density (+) and estimated chlorophyll *a* (o) profiles.

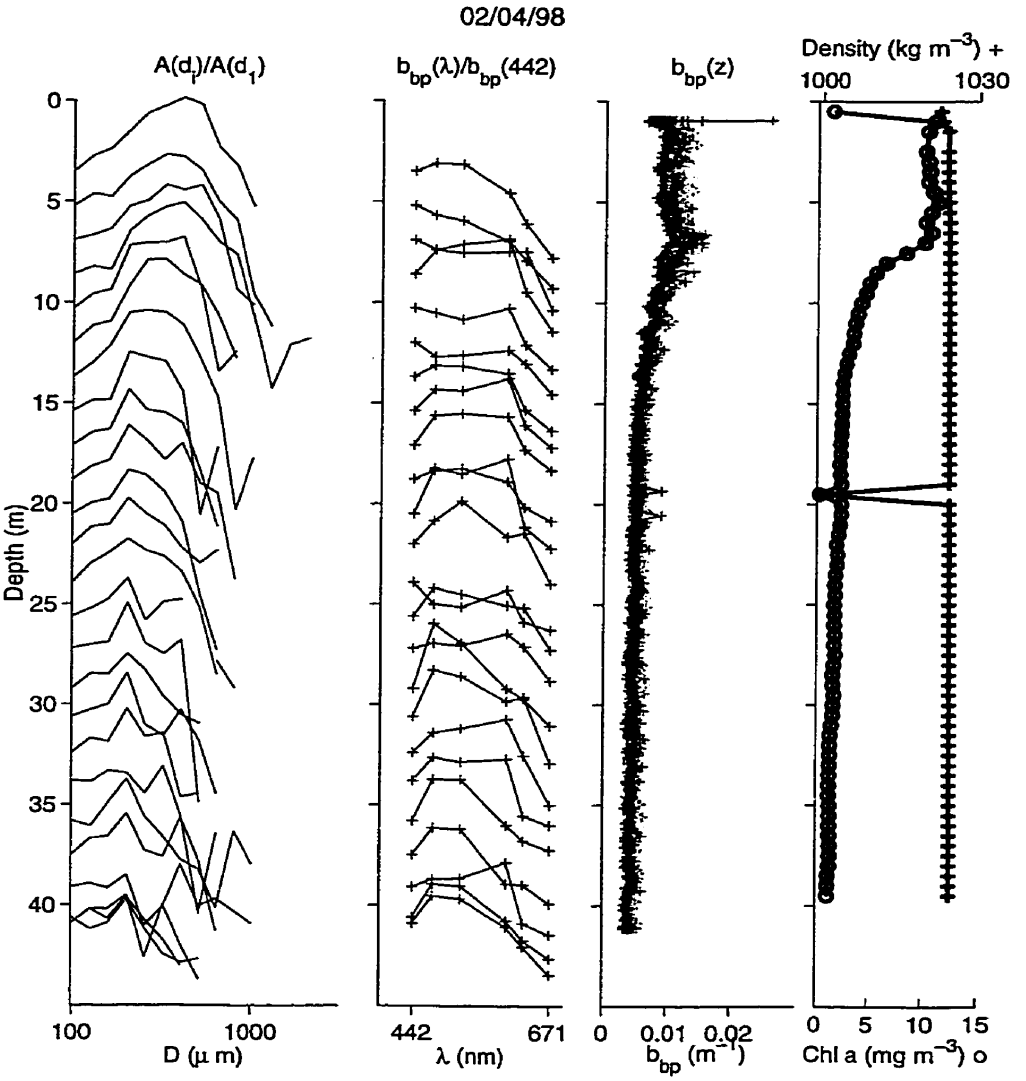

Figure A.6: Plot of all data used in this study collected on April 2, 1998. The first panel shows particle areal size distributions normalized to the value in the first bin and scaled to plot to depth of image capture. The second shows particulate backscatter spectra normalized to the value at 442nm and scaled as in the first panel. The third panel is particulate backscatter profiles for all wavelengths. The fourth panel shows calculated density (+) and estimated chlorophyll *a* (o) profiles.

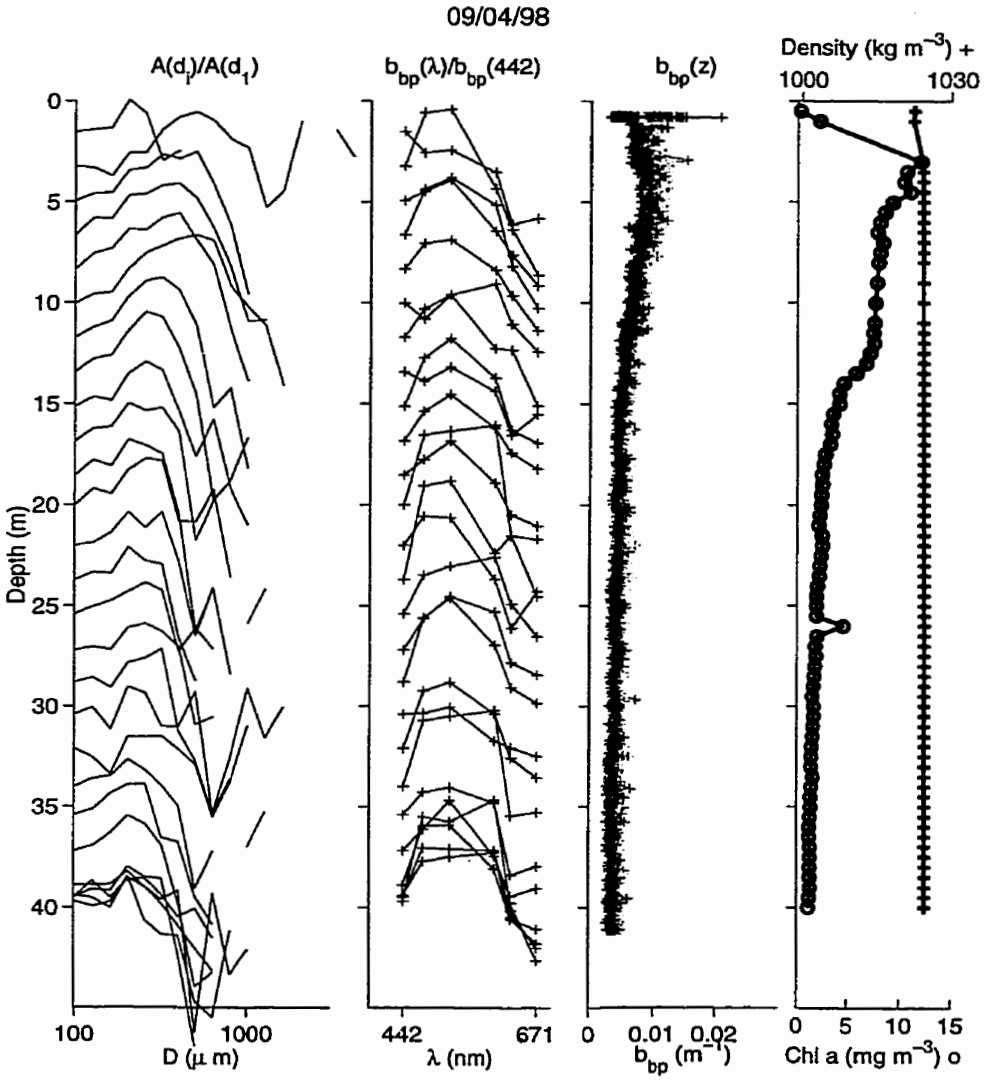

Figure A.7: Plot of all data used in this study collected on April 9, 1998. The first panel shows particle areal size distributions normalized to the value in the first bin and scaled to plot to depth of image capture. The second shows particulate backscatter spectra normalized to the value at 442nm and scaled as in the first panel. The third panel is particulate backscatter profiles for all wavelengths. The fourth panel shows calculated density (+) and estimated chlorophyll *a* (o) profiles.

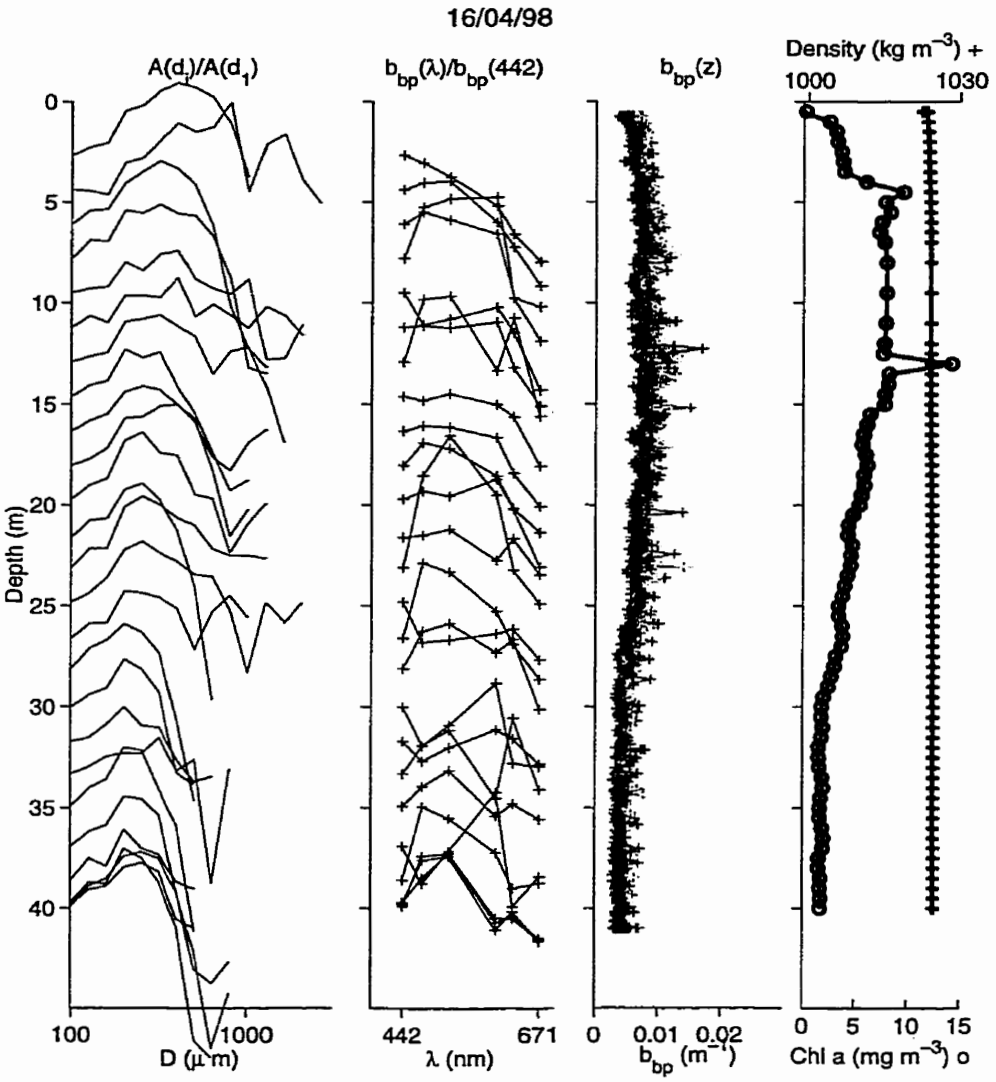

Figure A.8: Plot of all data used in this study collected on April 16, 1998. The first panel shows particle areal size distributions normalized to the value in the first bin and scaled to plot to depth of image capture. The second shows particulate backscatter spectra normalized to the value at 442nm and scaled as the first panel. The third panel is particulate backscatter profiles for all wavelengths. The fourth panel shows calculated density (+) and estimated chlorophyll *a* (o) profiles.

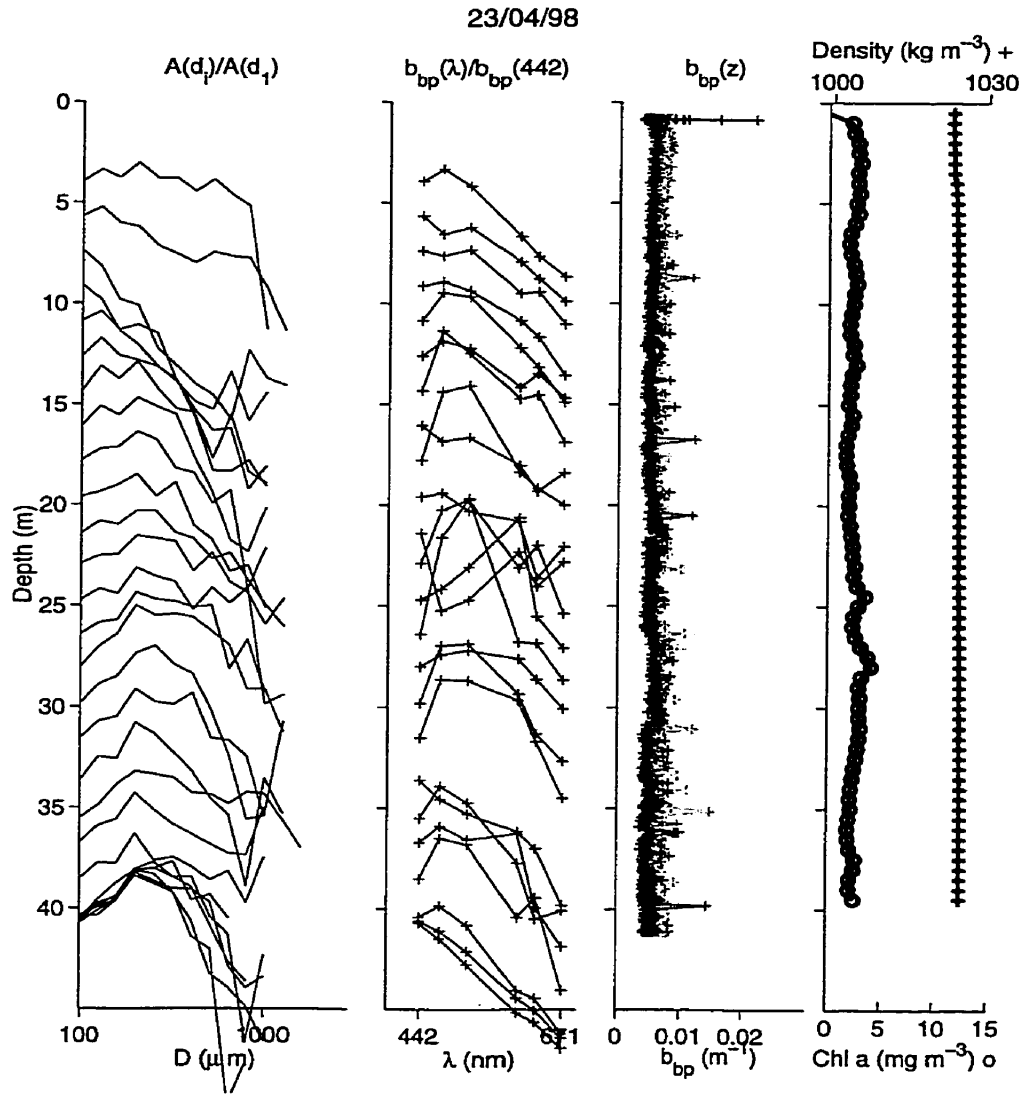

Figure A.9: Plot of all data used in this study collected on April 23, 1998. The first panel shows particle areal size distributions normalized to the value in the first bin and scaled to plot to depth of image capture. The second shows particulate backscatter spectra normalized to the value at 442nm and scaled as in the first panel. The third panel is particulate backscatter profiles for all wavelengths. The fourth panel shows calculated density (+) and estimated chlorophyll *a* (o) profiles.

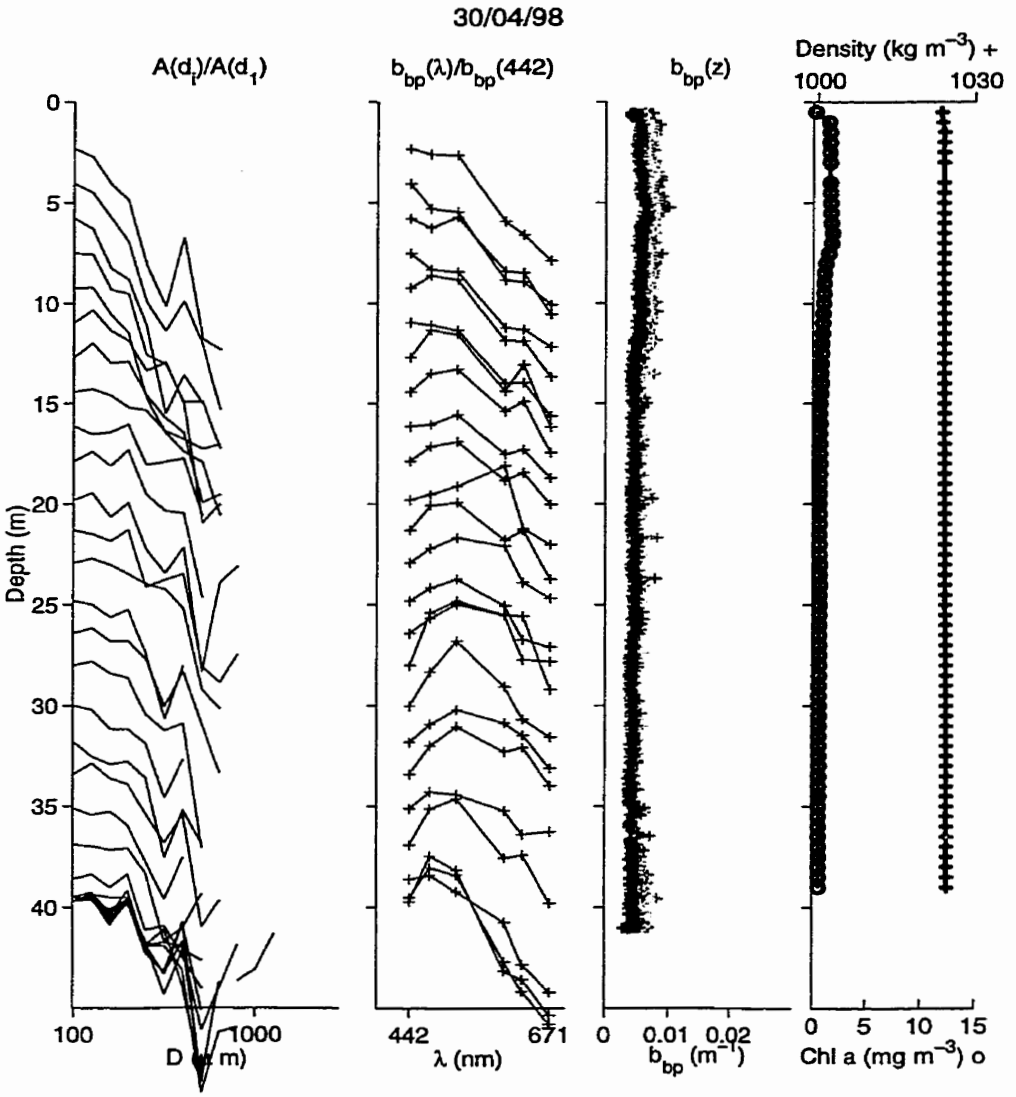

Figure A.10: Plot of all data used in this study collected on April 30, 1998. The first panel shows particle areal size distributions normalized to the value in the first bin and scaled to plot to depth of image capture. The second shows particulate backscatter spectra normalized to the value at 442nm and scaled as in the first panel. The third panel is particulate backscatter profiles for all wavelengths. The fourth panel shows calculated density (+) and estimated chlorophyll a (o) profiles.

Appendix B

Measurement and Correction of Backscatter

Tables B.1, B.2, B.3 and B.4 give the percent difference between backscatter calculated with the default correction (η=50) and that corrected with absorption and an estimate of the backscattering ratio. The percent difference was calculated as in Equation 3.11. Figures B.1–B.5 show backscatter normalized to the value at 442nm for the absorption sample depths on each given sample day.

Table B.1: Percent difference between HOBI Lab's default correction with η=50 and correction using measured absorption and estimated backscatter ratio ($\tilde{b_b} = b_b/b$) as 0.01. A negative percent difference indicates that the default correction has resulted in a final backscatter coefficient that is less than that corrected with measured absorption. This indicates that the default correction has underestimated pathlength attenuation.

		Percent Difference					
Day	Depth(m)	442nm	470nm	510nm	589nm	620nm	671nm
26/03	surf	-16.75	-10.56	-8.36	-7.22	-8.99	-16.79
26/03	5	-18.33	-11.78	-9.56	-7.63	-9.08	-16.46
02/04	surf	-13.58	-9.03	-6.96	-7.22	-8.19	-14.77
02/04	5	-13.95	-9.93	-8.48	-8.15	-9.65	-17.66
02/04	10	-12.31	-8.53	-7.21	-7.15	-8.62	-17.19
02/04	20	-6.51	-4.31	-4.11	-5.42	-7.03	-15.48
02/04	40	-5.10	-3.40	-3.39	-4.97	-6.52	-16.27
09/04	surf	-19.22	-10.54	-7.64	-6.50	-7.60	-16.35
09/04	5	-16.70	-10.05	-7.75	-7.02	-8.55	-16.08
09/04	10	-13.74	-8.08	-6.58	-6.03	-7.67	-16.06
09/04	20	-7.83	-4.61	-4.15	-4.64	-6.40	-14.92
09/04	40	-7.79	-4.51	-3.95	-4.45	-6.24	-16.62
16/04	surf	-24.95	-13.32	-9.03	-6.27	-7.38	-14.93
16/04	5	-14.62	-8.43	-6.51	-5.92	-7.67	-15.51
16/04	10	-13.57	-8.39	-6.79	-6.27	-7.84	-15.51
16/04	20	-10.95	-6.88	-5.86	-6.07	-7.47	-14.90
16/04	40	-8.49	-4.88	-4.20	-4.62	-6.55	-15.68
23/04	surf	-17.12	-9.72	-7.20	-5.70	-7.16	-14.07
23/04	5	-10.91	-6.47	-5.24	-5.00	-6.81	-14.39
23/04	10	-13.32	-7.70	-6.41	-5.41	-7.25	-17.06
23/04	20	-9.86	-6.10	-5.57	-5.16	-7.02	-14.01
23/04	40	-9.69	-6.21	-5.20	-5.31	-7.27	-14.73
30/04	surf	-10.08	-6.13	-5.04	-4.95	-6.68	-15.34
30/04	5	-10.60	-6.91	-5.75	-5.58	-7.38	-14.53
30/04	10	-8.98	-5.73	-4.91	-5.14	-6.85	-14.35
30/04	20	-7.71	-4.66	-4.27	-4.80	-6.58	-14.47
30/04	40	-7.80	-4.93	-4.35	-4.74	-6.56	-14.92

Table B.2: Percent difference between HOBI Lab's default correction with η=50 and correction using measured absorption and estimated backscatter ratio ($\tilde{b_b} = b_b/b$) as 0.02. A negative percent difference indicates that the default correction has resulted in a final backscatter coefficient that is less than that corrected with measured absorption. This indicates that the default correction has underestimated pathlength attenuation.

		Percent Difference					
Day	Depth(m)	442nm	470nm	510nm	589nm	620nm	671nm
26/03	surf	-9.12	-4.40	-2.48	-1.53	-3.74	-10.75
26/03	5	-10.46	-5.37	-3.37	-1.69	-3.62	-10.29
02/04	surf	-5.53	-2.53	-0.75	-0.95	-2.99	-8.66
02/04	5	-5.38	-2.74	-1.56	-1.58	-3.76	-10.87
02/04	10	-5.18	-2.84	-1.73	-1.71	-3.85	-11.34
02/04	20	-0.90	-0.16	-0.08	-1.75	-3.69	-10.74
02/04	40	0.16	0.32	0.19	-1.78	-3.67	-11.75
09/04	surf	-12.64	-5.69	-3.25	-2.13	-4.14	-11.32
09/04	5	-8.60	-3.64	-1.58	-1.42	-3.47	-9.99
09/04	10	-7.06	-3.11	-1.74	-1.63	-3.70	-10.84
09/04	20	-2.31	-0.73	-0.46	-1.38	-3.48	-10.41
09/04	40	-2.36	-0.88	-0.49	-1.43	-3.65	-12.12
16/04	surf	-18.17	-8.46	-4.78	-2.72	-4.33	-10.33
16/04	5	-7.08	-2.66	-1.03	-1.08	-3.37	-9.99
16/04	10	-6.03	-2.65	-1.32	-1.18	-3.49	-9.89
16/04	20	-4.27	-1.77	-0.85	-0.94	-3.31	-9.54
16/04	40	-3.07	-1.09	-0.63	-1.44	-3.60	-11.01
23/04	surf	-10.28	-4.77	-2.74	-1.94	-3.78	-9.29
23/04	5	-4.51	-1.94	-0.93	-1.33	-3.47	-9.65
23/04	10	-6.93	-2.90	-1.50	-1.63	-3.99	-12.29
23/04	20	-3.87	-1.45	-0.70	-1.35	-3.41	-9.20
23/04	40	-3.17	-1.28	-0.57	-1.22	-3.34	-9.33
30/04	surf	-3.94	-1.64	-0.76	-1.49	-3.61	-10.70
30/04	5	-3.56	-1.72	-0.73	-1.33	-3.44	-9.44
30/04	10	-2.65	-1.11	-0.43	-1.36	-3.40	-9.57
30/04	20	-2.10	-0.69	-0.37	-1.30	-3.52	-9.89
30/04	40	-2.01	-0.71	-0.33	-1.45	-3.56	-10.41

Table B.3: Percent difference between HOBI Lab's default correction with η=50 and correction using measured absorption and estimated backscatter ratio ($\tilde{b_b} = b_b/b$) as 0.03. A negative percent difference indicates that the default correction has resulted in a final backscatter coefficient that is less than that corrected with measured absorption. This indicates that the default correction has underestimated pathlength attenuation.

		Percent Difference					
Day	Depth(m)	442nm	470nm	510nm	589nm	620nm	671nm
26/03	surf	-6.69	-2.48	-0.59	0.24	-2.06	-8.81
26/03	5	-7.95	-3.37	-1.39	0.16	-1.88	-8.31
02/04	surf	-2.97	-0.51	1.24	0.99	-1.33	-6.70
02/04	5	-2.67	-0.52	0.65	0.45	-1.89	-8.70
02/04	10	-2.91	-1.05	0.03	-0.01	-2.33	-9.45
02/04	20	0.92	1.16	1.23	-0.58	-2.61	-9.20
02/04	40	1.86	1.51	1.36	-0.76	-2.74	-10.28
09/04	surf	-10.52	-4.15	-1.83	-0.77	-3.02	-9.69
09/04	5	-6.02	-1.64	0.39	0.32	-1.85	-8.04
09/04	10	-4.92	-1.54	-0.18	-0.23	-2.41	-9.15
09/04	20	-0.53	0.51	0.74	-0.33	-2.53	-8.95
09/04	40	-0.61	0.28	0.64	-0.46	-2.81	-10.65
16/04	surf	-15.98	-6.91	-3.41	-1.58	-3.34	-8.84
16/04	5	-4.67	-0.85	0.73	0.45	-1.99	-8.21
16/04	10	-3.62	-0.85	0.44	0.41	-2.09	-8.08
16/04	20	-2.13	-0.17	0.76	0.66	-1.97	-7.81
16/04	40	-1.31	0.12	0.54	-0.42	-2.64	-9.49
23/04	surf	-8.08	-3.20	-1.30	-0.75	-2.69	-7.74
23/04	5	-2.46	-0.51	0.46	-0.16	-2.39	-8.11
23/04	10	-4.87	-1.38	0.08	-0.43	-2.93	-10.74
23/04	20	-1.94	0.01	0.87	-0.14	-2.25	-7.64
23/04	40	-1.08	0.27	0.93	0.08	-2.07	-7.59
30/04	surf	-1.97	-0.22	0.63	-0.38	-2.62	-9.20
30/04	5	-1.32	-0.10	0.89	0.01	-2.18	-7.79
30/04	10	-0.62	0.35	1.01	-0.16	-2.28	-8.01
30/04	20	-0.29	0.57	0.89	-0.19	-2.53	-8.40
30/04	40	-0.14	0.63	0.97	-0.40	-2.58	-8.94

Table B.4: Percent difference between HOBI Lab's default correction with η=50 and correction using measured absorption and estimated backscatter ratio ($\tilde{b_b} = b_b/b$) as 0.04. A negative percent difference indicates that the default correction has resulted in a final backscatter coefficient that is less than that corrected with measured absorption. This indicates that the default correction has underestimated pathlength attenuation.

		Percent Difference					
Day	Depth(m)	442nm	470nm	510nm	589nm	620nm	671nm
26/03	surf	-5.49	-1.54	0.34	1.10	-1.24	-7.85
26/03	5	-6.72	-2.39	-0.42	1.06	-1.02	-7.34
02/04	surf	-1.72	0.47	2.22	1.93	-0.52	-5.74
02/04	5	-1.34	0.56	1.73	1.43	-0.97	-7.63
02/04	10	-1.79	-0.18	0.90	0.82	-1.58	-8.52
02/04	20	1.81	1.80	1.88	0.00	-2.07	-8.44
02/04	40	2.70	2.09	1.94	-0.26	-2.29	-9.55
09/04	surf	-9.47	-3.40	-1.12	-0.10	-2.47	-8.89
09/04	5	-4.75	-0.67	1.36	1.17	-1.05	-7.07
09/04	10	-3.86	-0.77	0.59	0.45	-1.78	-8.32
09/04	20	0.35	1.11	1.34	0.18	-2.06	-8.22
09/04	40	0.26	0.84	1.19	0.02	-2.39	-9.92
16/04	surf	-14.90	-6.15	-2.73	-1.02	-2.85	-8.10
16/04	5	-3.49	0.03	1.59	1.19	-1.31	-7.33
16/04	10	-2.44	0.02	1.31	1.19	-1.40	-7.18
16/04	20	-1.07	0.62	1.56	1.44	-1.31	-6.95
16/04	40	-0.45	0.71	1.11	0.08	-2.16	-8.74
23/04	surf	-7.00	-2.43	-0.59	-0.16	-2.15	-6.97
23/04	5	-1.44	0.20	1.15	0.41	-1.86	-7.35
23/04	10	-3.86	-0.64	0.86	0.16	-2.41	-9.97
23/04	20	-0.99	0.73	1.64	0.45	-1.68	-6.86
23/04	40	-0.05	1.02	1.66	0.71	-1.45	-6.73
30/04	surf	-0.99	0.47	1.31	0.16	-2.13	-8.45
30/04	5	-0.21	0.70	1.68	0.67	-1.55	-6.97
30/04	10	0.38	1.07	1.73	0.43	-1.73	-7.25
30/04	20	0.60	1.19	1.52	0.36	-2.04	-7.66
30/04	40	0.78	1.28	1.61	0.12	-2.10	-8.21

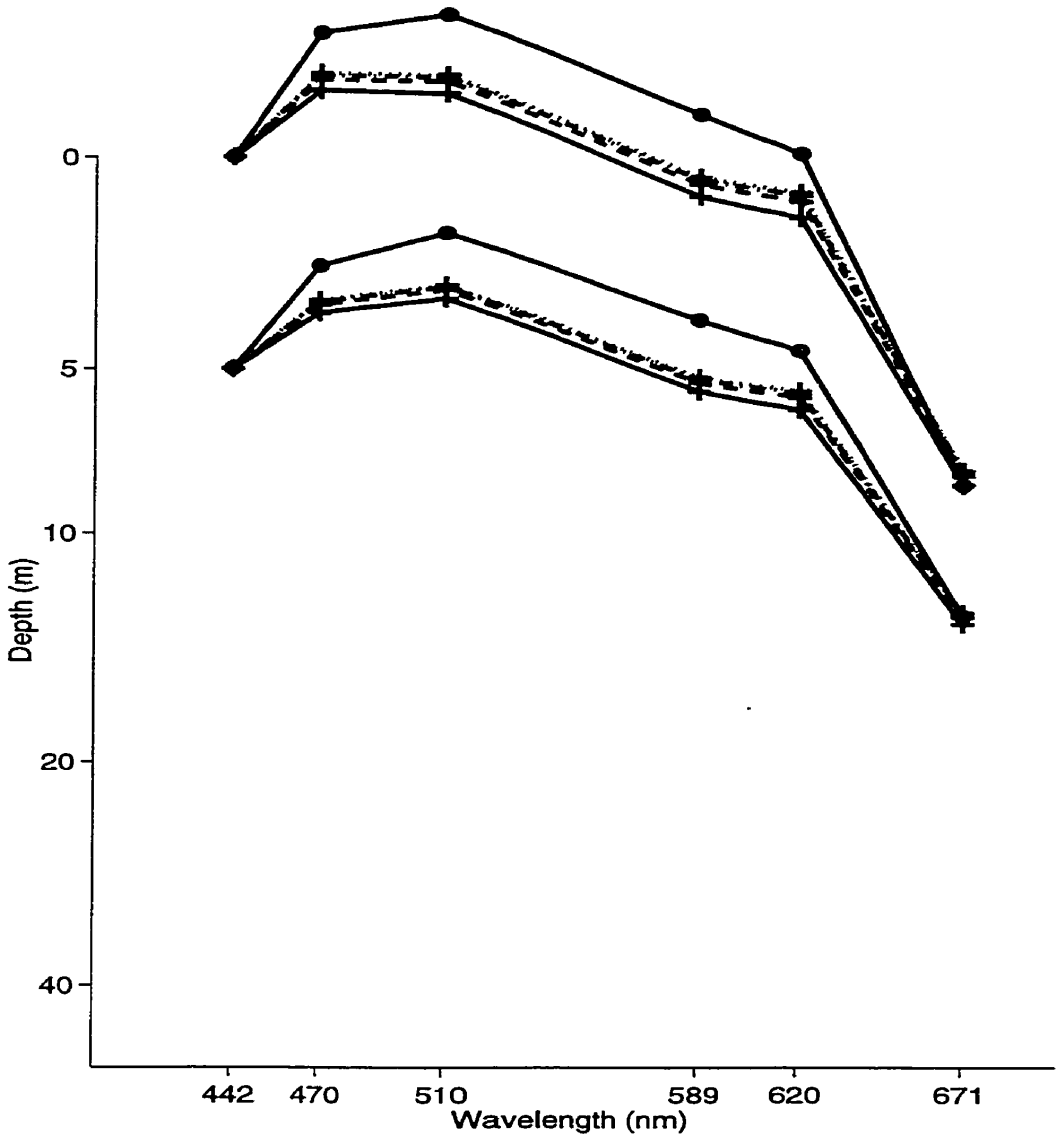

Figure B.1: Backscatter normalized to the backscatter at 442nm corrected with η and total absorption (measurements of particulate and dissolved absorption as well as that due to water as estimated by Pope and Fry (1997)) with four values of $\tilde{b}_b$ for March 23, 1998 at the five depths for which absorption measurements were made. The normalized values are scaled such that the first data point has an actual value of one but is plotted with a y-value equal to the sample depth. —o— default correction (Equations 3.2, 3.3 and 3.4); —+— $\tilde{b}_{bp}$=0.01; - - + - - $\tilde{b}_{bp}$=0.02; - - + - · $\tilde{b}_{bp}$=0.03; - - + - · $\tilde{b}_{bp}$=0.04 (Equations 3.2, 3.3 and 3.4).

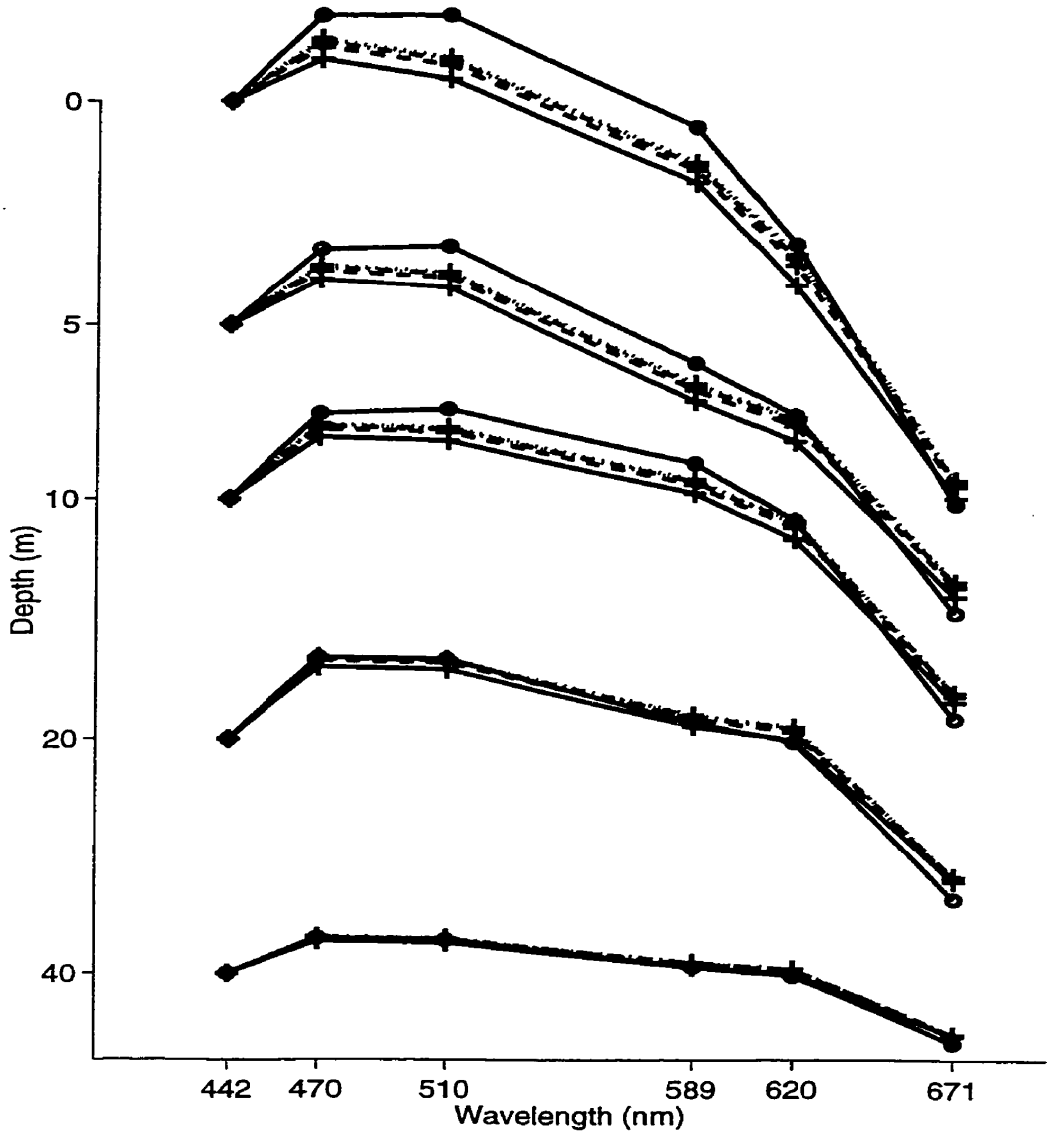

Figure B.2: Backscatter normalized to the backscatter at 442nm corrected with η and total absorption (measurements of particulate and dissolved absorption as well as that due to water as estimated by Pope and Fry (1997)) with four values of $\tilde{b}_b$ for April 2, 1998 at the five depths for which absorption measurements were made. The normalized values are scaled such that the first data point has an actual value of one but is plotted with a y-value equal to the sample depth. —o— default correction (Equations 3.2, 3.3 and 3.4); —+— $\tilde{b}_{bp}$=0.01; - - + - - $\tilde{b}_{bp}$=0.02; - · + - · $\tilde{b}_{bp}$=0.03; · ·+· · $\tilde{b}_{bp}$=0.04 (Equations 3.2, 3.3 and 3.4).

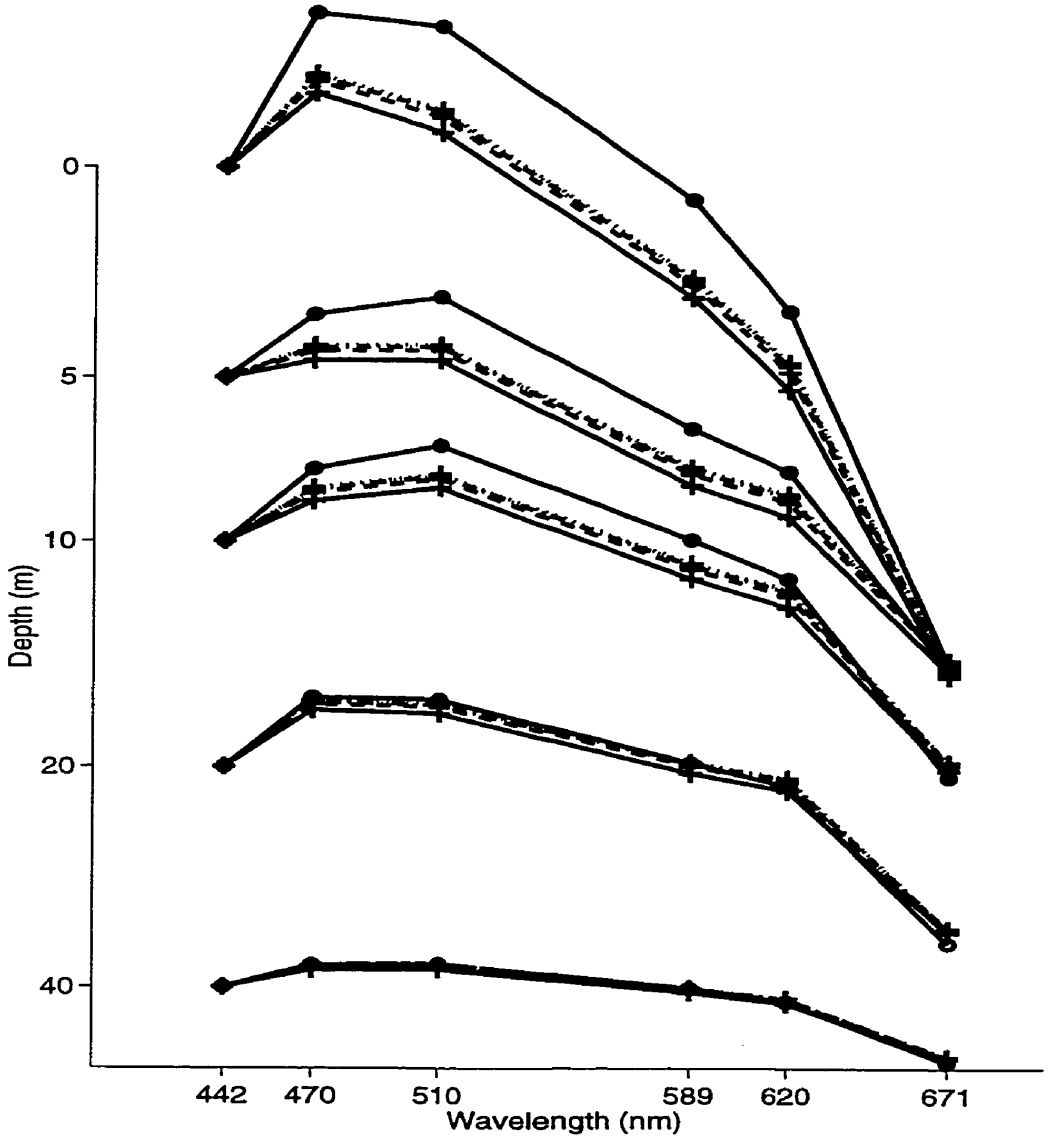

Figure B.3: Backscatter normalized to the backscatter at 442nm corrected with η and total absorption (measurements of particulate and dissolved absorption as well as that due to water as estimated by Pope and Fry (1997)) with four values of $\tilde{b}_b$ for April 9, 1998 at the five depths for which absorption measurements were made. The normalized values are scaled such that the first data point has an actual value of one but is plotted with a y-value equal to the sample depth. —o— default correction (Equations 3.2, 3.3 and 3.4); —+— $\tilde{b}_{bp}$=0.01; - - + - - $\tilde{b}_{bp}$=0.02; - · + - · $\tilde{b}_{bp}$=0.03; · · + · · $\tilde{b}_{bp}$=0.04 (Equations 3.2, 3.3 and 3.4).

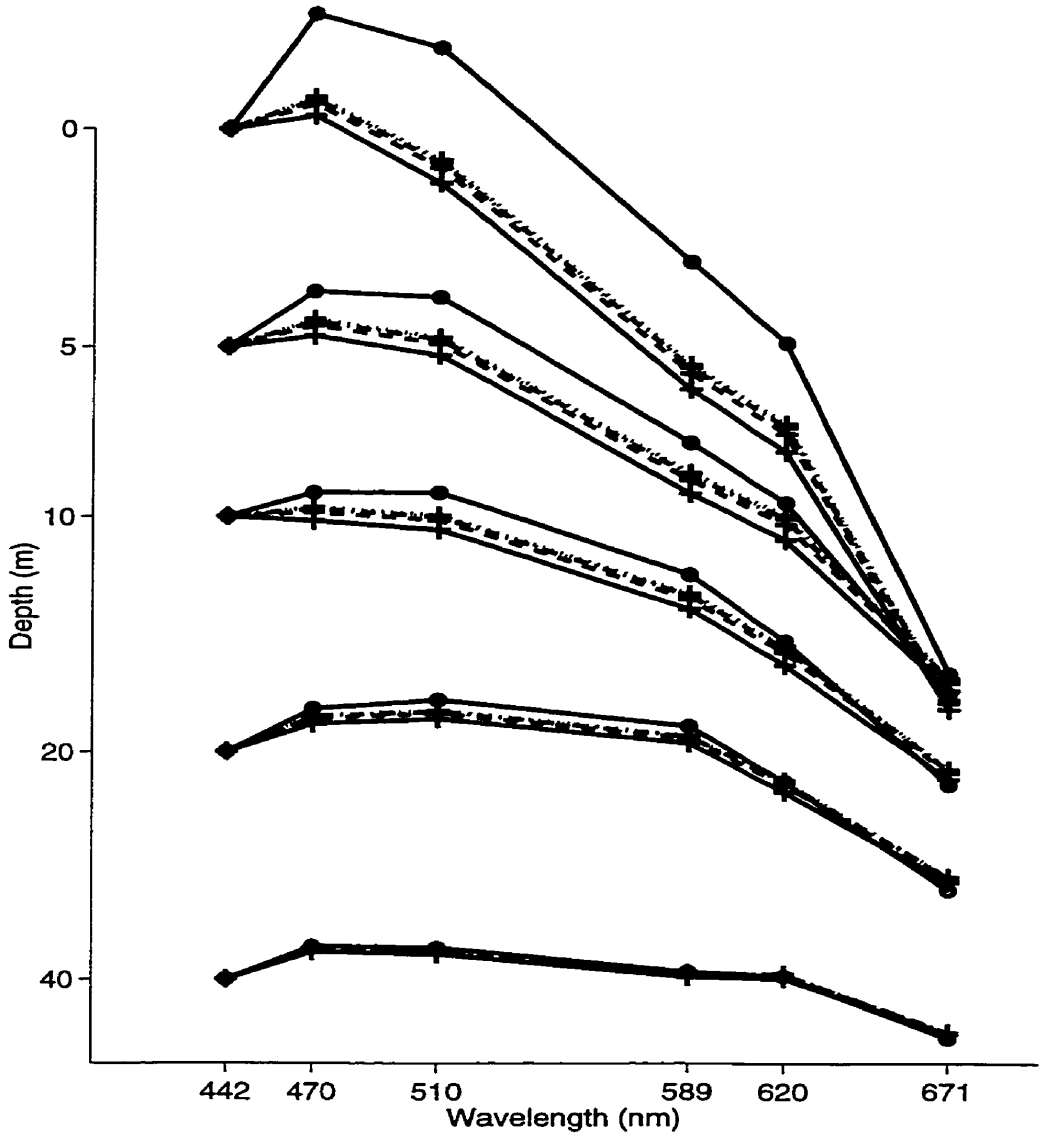

Figure B.4: Backscatter normalized to the backscatter at 442nm corrected with η and total absorption (measurements of particulate and dissolved absorption as well as that due to water as estimated by Pope and Fry (1997)) with four values of $\tilde{b_b}$ for April 16, 1998 at the five depths for which absorption measurements were made. The normalized values are scaled such that the first data point has an actual value of one but is plotted with a y-value equal to the sample depth. —o— default correction (Equations 3.2, 3.3 and 3.4); —+— $\tilde{b_{bp}}$=0.01; - - + - - $\tilde{b_{bp}}$=0.02; - · + - · $\tilde{b_{bp}}$=0.03; · · + · · $\tilde{b_{bp}}$=0.04 (Equations 3.2, 3.3 and 3.4).

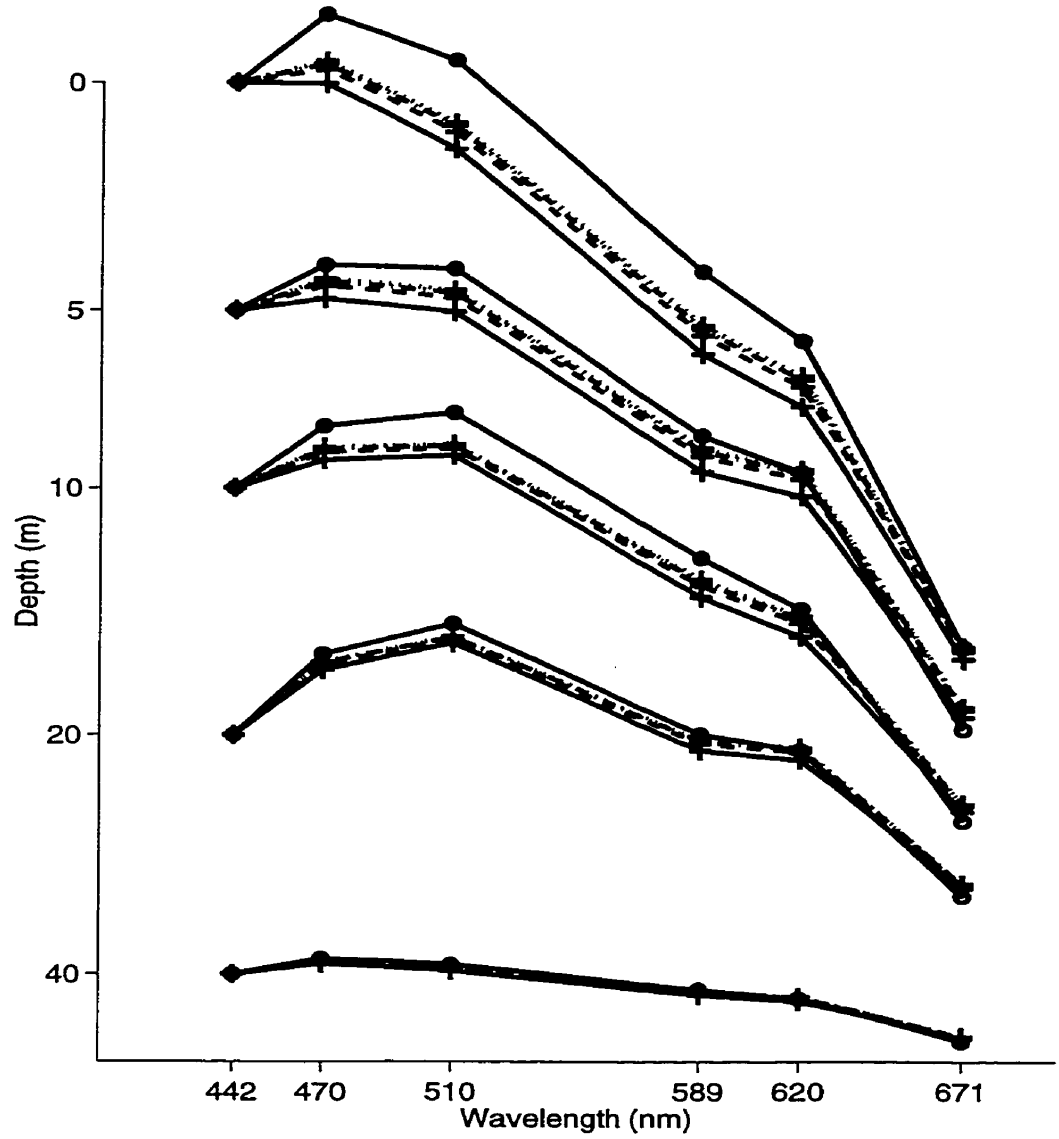

Figure B.5: Backscatter normalized to the backscatter at 442nm corrected with η and total absorption (measurements of particulate and dissolved absorption as well as that due to water as estimated by Pope and Fry (1997)) with four values of $\tilde{b_b}$ for April 23, 1998 at the five depths for which absorption measurements were made. The normalized values are scaled such that the first data point has an actual value of one but is plotted with a y-value equal to the sample depth. —o— default correction (Equations 3.2, 3.3 and 3.4); —+— $\tilde{b_{bp}}$=0.01; - - + - - $\tilde{b_{bp}}$=0.02; - · + - · $\tilde{b_{bp}}$=0.03; · · + · · $\tilde{b_{bp}}$=0.04 (Equations 3.2, 3.3 and 3.4).

Appendix C

Absorption Data

Figures C.1–C.6 show the measured absorption for the discrete sampling depths for sampling days after March 26, 1998. Each plot includes measurements of pigmented absorption (a_{phyt}), dissolved absorption (a_{DOM}), extracted absorption (a_{det}) and total absorption (a_T) which included absorption due to water as estimated by Pope and Fry (1997).

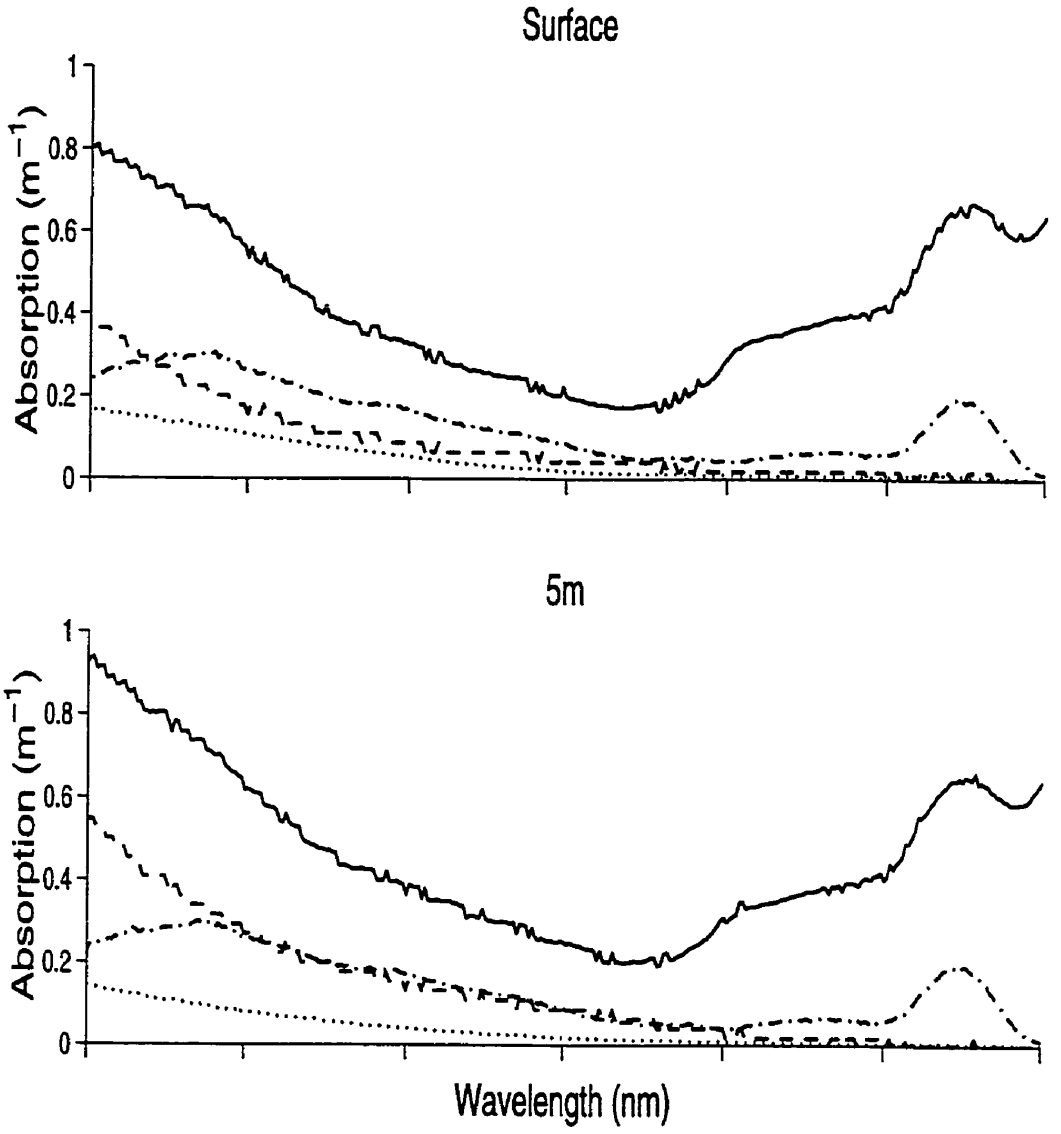

Figure C.1: Measured absorption (m^{-1}) for each depth of discrete water samples on March 26, 1998. Lines are plotted for —— a_T; - - - - a_{DOM}; - · - ·· a_{phyt}; · ···· a_{det}

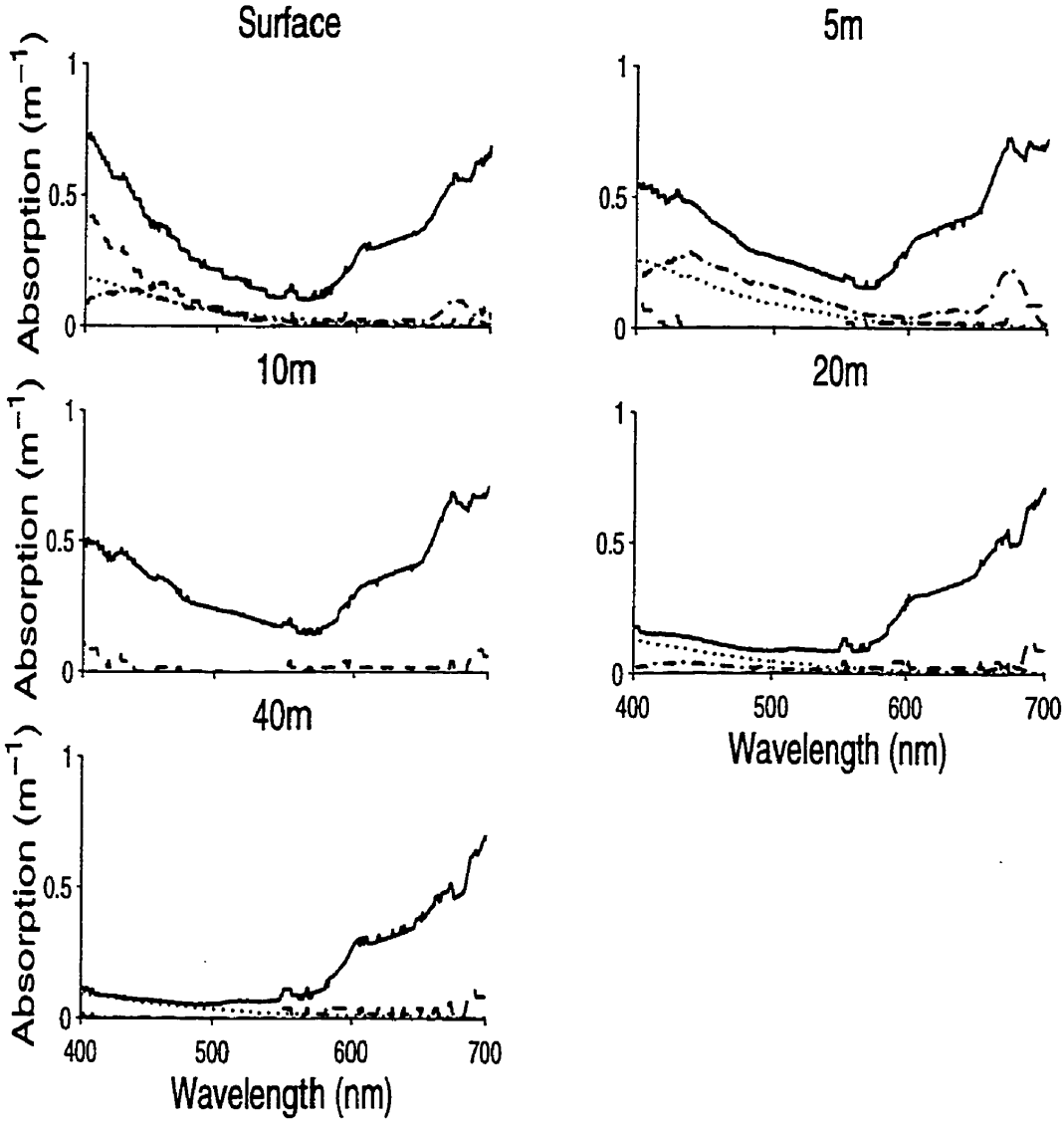

Figure C.2: Measured absorption (m^{-1}) for each depth of discrete water samples on April 2, 1998. Lines are plotted for —— a_T; - - - - a_{DOM}; - ·-· - a_{phyt}; · · · · a_{det}

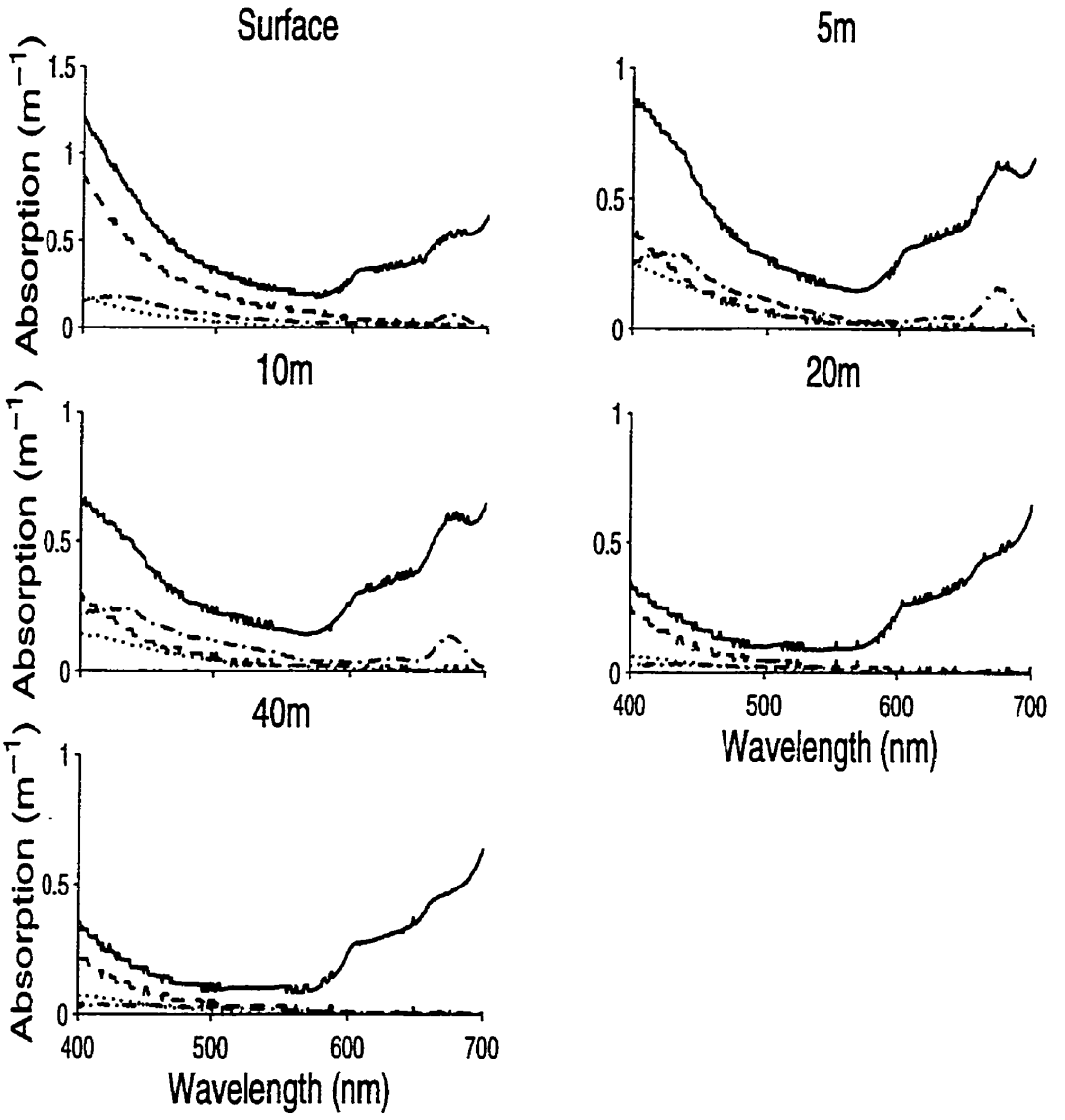

Figure C.3: Measured absorption (m^{-1}) for each depth of discrete water samples on April 9, 1998. Note that surface absorption is plotted with a different vertical axis scale. Lines are plotted for —— a_T; - - - - a_{DOM}; - · - · a_{phyt}; · · · · a_{det}

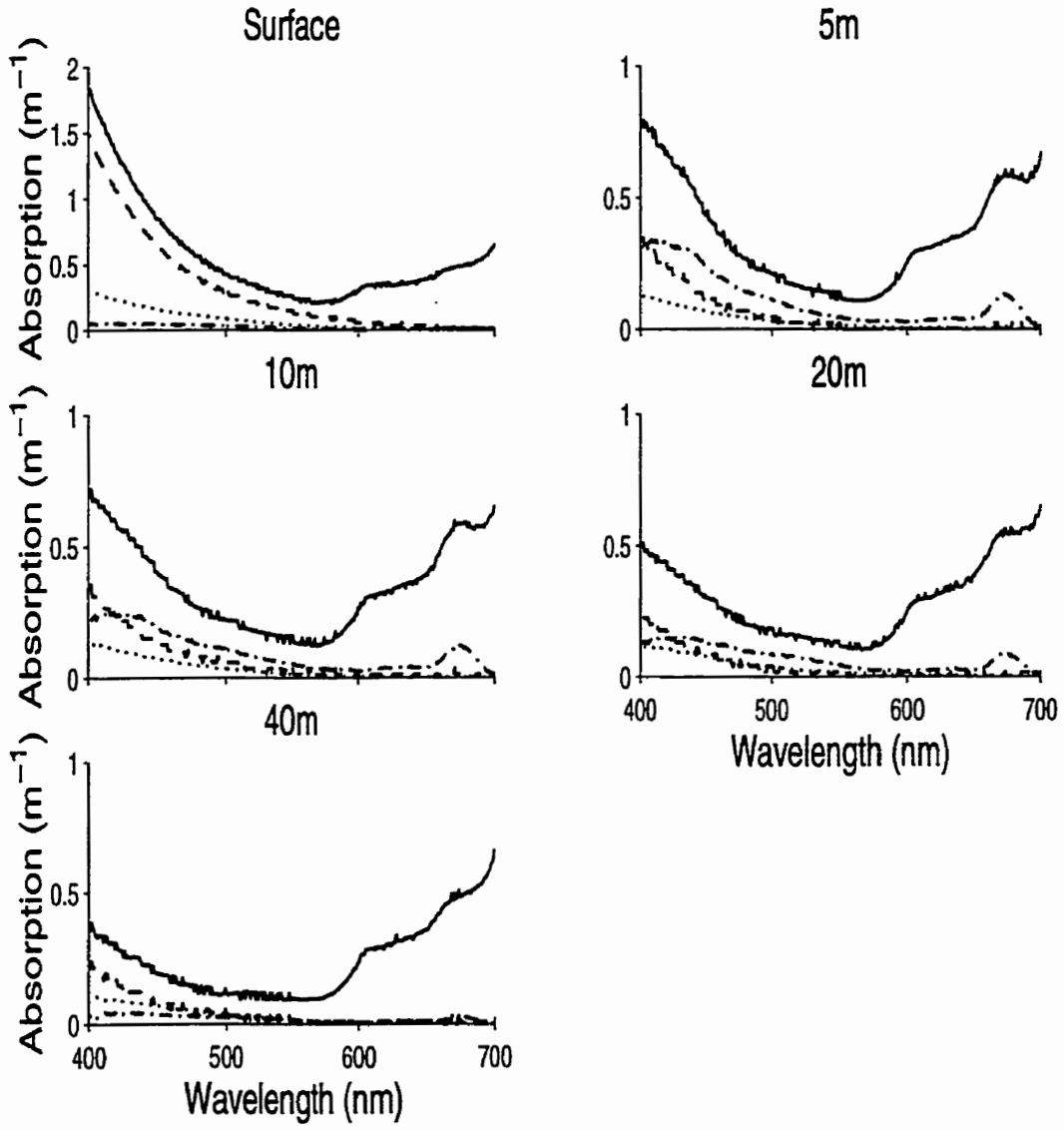

Figure C.4: Measured absorption (m^{-1}) for each depth of discrete water samples on April 16, 1998. Note that surface absorption is plotted with a different vertical axis scale. Lines are plotted for ——— a_T; - - - - a_{DOM}; - · - · a_{phyt}; · · · · a_{det}

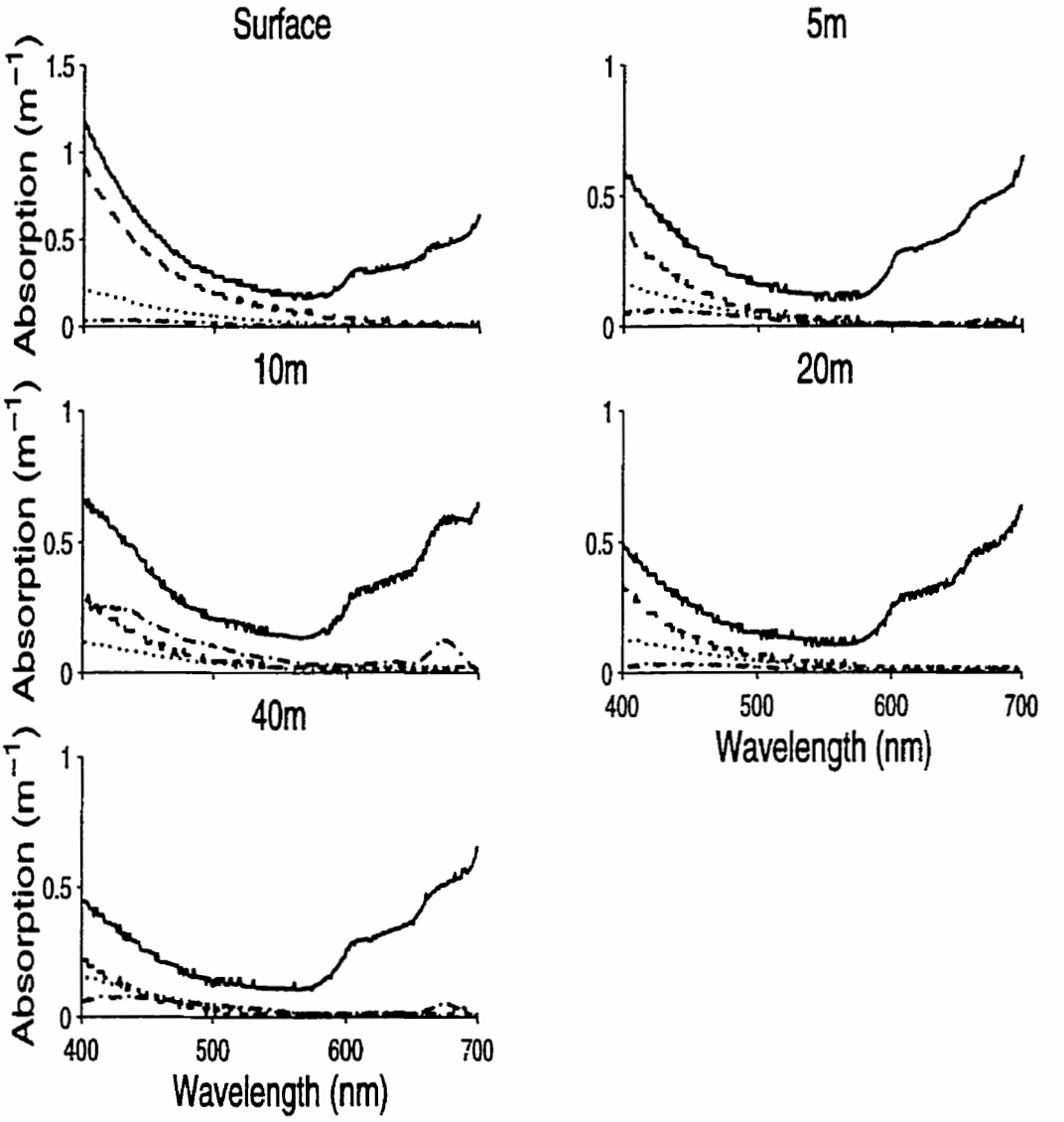

Figure C.5: Measured absorption (m^{-1}) for each depth of discrete water samples on April 23, 1998. Note that surface absorption is plotted with a different vertical axis scale. Lines are plotted for —— a_T; - - - - a_{DOM}; - · - · a_{phyt}; · · · · a_{det}

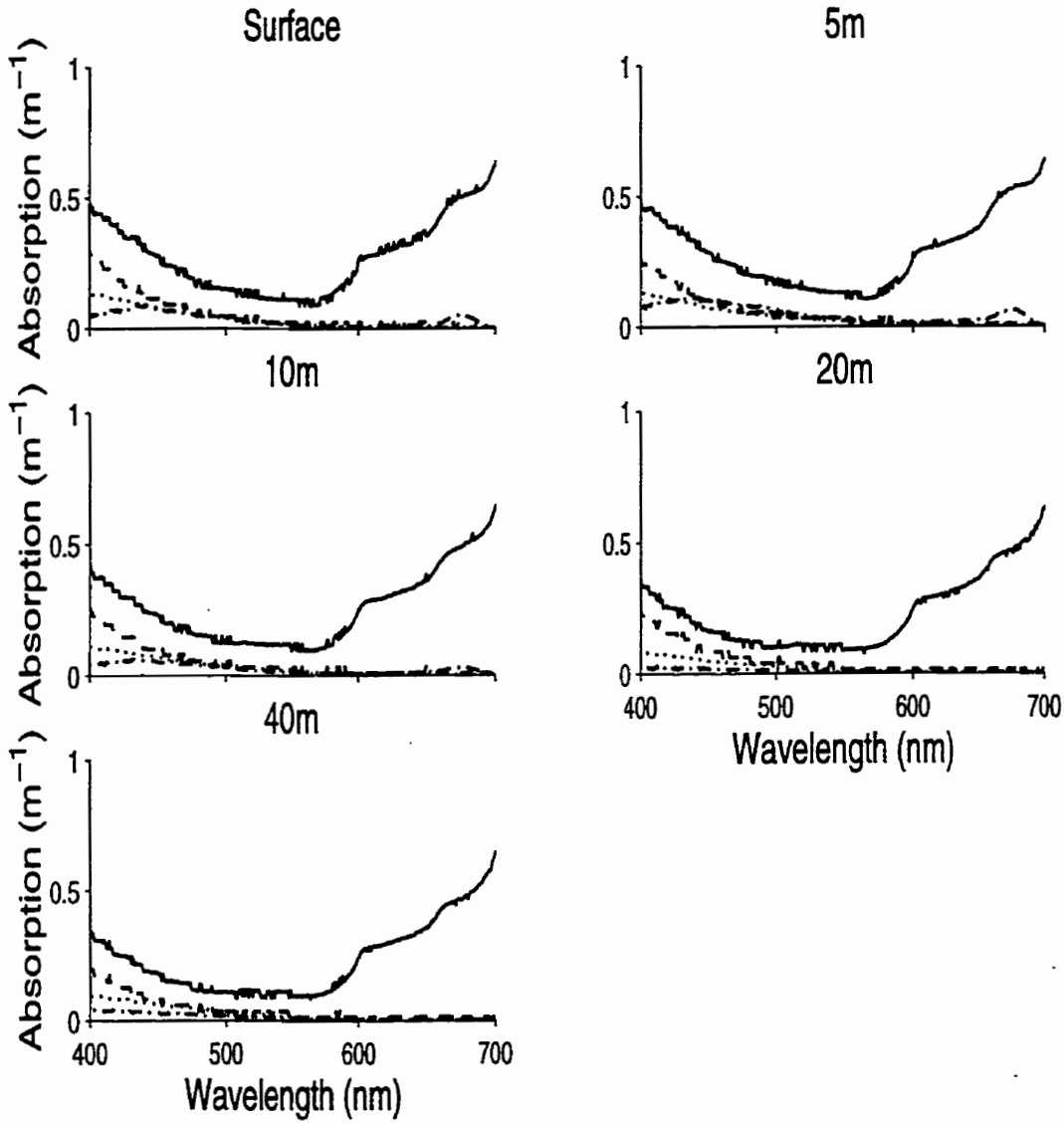

Figure C.6: Measured absorption (m^{-1}) for each depth of discrete water samples on April 30, 1998. Lines are plotted for —— a_T; - - - - a_{DOM}; - · - · a_{phyt}; · · · · a_{det}

Bibliography

Aas, E. 1981. The refractive index of phytoplankton. Institute Report Series 46, Universitetet I Oslo Institutt for Geofysikk.

Ahn, Y.-H., Morel, A., and Bricaud, A. 1992. Light backscattering efficiency and related properties of some phytoplankters. *Deep-Sea Research*, **39(11/12)**, 1835–1855.

Alldredge, A. and Gotschalk, C. 1989. Direct observations of the mass flocculation of diatom blooms: Characteristics, settling velocities and formation of diatom aggregates. *Deep-Sea Research*, **36(2)**, 159–171.

Bohren, C. and Huffman, D. 1983. *Absorption and scattering of light by small particles.* John Wiley & Sons.

Bricaud, A. and Morel, A. 1986. Light attenuation and scattering by phytoplanktonic cells: A theoretical modeling. *Applied Optics*, **25(4)**, 571–580.

Brown, O. and Gordon, H. 1973. Two component Mie scattering models of Sargasso Sea particles. *Applied Optics*, **12(10)**, 2461–2465.

Carder, K. and Costello, D. 1994. *Optical effects of large particles*, chapter 13, pages 243–257. Ocean Optics. Oxford University Press.

Ciotti, A. 1999. *Influence of phytoplankton communities on relationships between optical properties of coastal surface waters.* PhD dissertation, Dalhousie University, Department of Oceanography.

Conner, C. and Visser, A. D. 1992. A laboratory investigation of particle size effects on an optical backscatterance sensor. *Marine Geology*, **108**, 151–159.

Eisma, D., Schuhmacher, T., Boekel, H., Van Heerwaarden, J., Franken, H., Laan, M., Vaars, A., Eijgenraam, F., and Kalf, J. 1990. A camera and image-analysis system for *in situ* observation of flocs in natural waters. *Netherlands Journal of Sea Research*, **27(1)**, 43–56.

Friedman, G., Sanders, J., and Kopaska-Merkel, D. 1992. *Principles of sedimentary deposits.* Macmillan Publishing Company.

Gibbs, R. 1978. Light scattering from particles of different shapes. *Journal of Geophysical Research*, **83(C1)**, 501–502.

Green, R. 1979. *Sampling design and statistical methods for environmental biologists.* John Wiley & Sons.

Hartigan, J. 1975. *Clustering algorithms.* John Wiley & Sons.

HOBI Labs 1999. *Algorithm for estimating the σ attenuation coefficient from b_b.* HOBI Labs, Watsonville CA.

IPP. 1997. *Image-Pro Plus reference guide for Windows.* Media Cybernetics, Silver Springs, MD, version 3.0 for windows edition.

Johnson, R. and Wichern, D. 1998. *Applied multivariate statistical analysis.* Prentice Hall.

Jonasz, M. 1987. Nonspherical sediment particles: Comparison of size and volume distributions obtained with an optical and a resistive particle counter. *Marine Geology*, **78**, 137–142.

Kaufman, L. and Rousseeuw, P. 1990. *Finding groups in data. An introduction to cluster analysis.* John Wiley & Sons.

Kepkay, P., Niven, S., and Milligan, T. 1993. Low molecular weight and colloidal DOC production during a phytoplankton bloom. *Marine Ecology Progress Series*, **100**, 233–244.

Kiorbe, T., Lundsgaard, C., Olesen, M., and Hansen, J. 1994. Aggregation and sedimentation processes during a spring phytoplankton bloom: A field experiment to test coagulation theory. *Journal of Marine Research*, **52**, 297–323.

Kirk, J. 1994. *Light and photosynthesis in aquatic ecosystems.* Cambridge University Press.

Kishino, M., Takahashi, M., Okami, N., and Ichimura, S. 1985. Estimation of the spectral absorption coefficients of phytoplankton in the sea. *Bulletin of Marine Science*, **37(2)**, 634–642.

Kranck, K. and Milligan, T. 1988. Macroflocs from diatoms: *In situ* photography of particles in Bedford Basin, Nova Scotia. *Marine Ecology Progress Series*, **44**, 183–189.

Kranck, K. and Milligan, T. 1992. Characteristics of suspended particles at an 11-hour anchor station in San Francisco Bay, California. *Journal of Geophysical Research*, **97(C7)**, 11373–11382.

Kullenberg, G. 1974. *Observed and computed scattering functions*, chapter 2, pages 25–49. Optical Aspects of Oceanography. Academic Press.

Legendre, P. and Legendre, L. 1998. *Numerical Ecology. Second English Edition.* Elsevier.

Li, W., Dickie, P., and Spry, J. 1998. Plankton monitoring programme in the Bedford Basin, 1991-1997. Canadian Data Report 1036:vii 342pp., Fisheries and Aquatic Sciences.

Li, X. and Logan, B. 1995. Size distributions and fractal properties of particles during a simulated phytoplankton bloom in a mesocosm. *Deep-Sea Research II*, **42(1)**, 125–138.

Maffione, R. and Dana, D. 1997. Instruments and methods for measuring the backward-scattering coefficient of ocean waters. *Applied Optics*, **36(24)**, 6057–6067.

Matlab. 1999. *Statistics toolbox user's guide for use with Matlab.* Natick MA, version 2.0 edition.

Milligan, T. 1996. *In situ* particle (floc) size measurements with the benthos 373 plankton silhouette camera. *Journal of Sea Research*, **36(1/2)**, 93–100.

Milligan, T. and Kranck, K. 1991. *Electroresistance particle size analysers*, pages 109–116. Principles, methods, and application of particle size analysis. Cambridge University Press.

Mitchell, B. and Kiefer, D. 1983. Determination of absorption and fluorescence excitation spectra for phytoplankton. In *Marine Phytoplanton and Productivity. Proceedings of invited lecture symposium. 5th Conference.*, volume 5, pages 157–169. European Society of Comp. Phys. Biochem.

Mitchell, B. and Kiefer, D. 1988. Chlorophyll *a* specific absorption and fluorescence excitation spectra for light-limited phytoplankton. *Deep-Sea Research*, **35(5)**, 639–663.

Mobley, C. 1994. *Light and water. Radiative transfer in natural waters.* Academic Press Inc.

Morel, A. 1991. *Optics of marine particles and marine optics*, pages 141–188. Particle Analysis in Oceanography. Springer-Verlag.

Pope, R. and Fry, E. 1997. Absorption spectrum (380–700 nm) of pure water. II. Integrating cavity measurements. *Applied Optics*, **36(33)**, 8710–8723.

Riebesell, U. 1991a. Particle aggregation during a diatom bloom. I. Biological aspects. *Marine Ecology Progress Series*, **69**, 281–291.

Riebesell, U. 1991b. Particle aggregation during a diatom bloom. II. Physical aspects. *Marine Ecology Progress Series*, **69**, 273–280.

Roesler, C. 1998. Theoretical and experimental approaches to improve the accuracy of particulate absorption coefficients derived from the quantitative filter technique. *Limnology and Oceanography*, **43(7)**, 1649–1660.

Sandland, R. and Young, P. 1979. Probabilistic tests and stopping rules associated with hierarchical classification techniques. *Australian Journal of Ecology*, **4**, 399–406.

Smetacek, V. 1985. Role of sinking in diatom life-history cycles: ecological, evolutionary and geological significance. *Marine Biology*, **84**, 239–251.

Smith, R. and Baker, K. 1981. Optical properties of the clearest natural waters (200-800nm). *Applied Optics*, **20(2)**, 177–184.

Spath, H. 1980. *Cluster analysis algorithms for data reduction and classification of objects*. Ellis Horwood Limited.

Stevens, J. 1986. *Applied multivariate statistics for the social sciences*. L. Erlbaum Associates.

Stramski, D. and Kiefer, D. 1991. Light scattering by microorganisms in the open ocean. *Progress in Oceanography*, **28**, 343–383.

Stramski, D. and Reynolds, R. 1993. Diel variations in the optical properties of a marine diatom. *Limnology and Oceanography*, **38(7)**, 1347–1364.

Ulloa, O., Sathyendranath, S., and Platt, T. 1994. Effect of particle-size distribution on the backscattering ratio in seawater. *Applied Optics*, **33(30)**, 7070–7076.

Yentsch, C. 1962. Measurement of visible light absorption by particulate matter in the ocean. *Limnology and Oceanography*, **7**, 207–217.

Zhang, X., Lewis, M., and Johnson, B. 1998. Influence of bubbles on scattering of light in the ocean. *Applied Optics*, **37(27)**, 6525–6536.